Max-Planck-Institut für Polymerforschung
Max Planck Institute for Polymer Research

Guiding the assembly of nanoparticles with polymers

Dissertation

Zur Erlangung des Grades

´Doktor rerum naturalium (Dr. rer. nat.)

dem Fachbereich Chemie, Pharmazie und Geowissenschaften

der Johannes Gutenberg-Universität Mainz

Yinzhou Guo

Geboren in Xi’an (China)

Mainz 2021

JOHANNES GUTENBERG
UNIVERSITÄT MAINZ

JG|U

The thesis was carried out from September 2017 until Feberary 2021 at the Max-Planck-Institute for Polymer Research, Mainz.

Dekan:

Prodekan:

Gutachter 1:

Gutachter 2:

Date of oral examination:

Declaration

I hereby declare that I wrote the dissertation submitted without any unauthorized external assistance and used only sources acknowledged in this work. All textual passages which are appropriate verbatim or paraphrased from published and unpublished texts, as well as all information obtained from oral sources, are duly indicated and listed in accordance with bibliographical rules. In carrying out this research, I complied with the rules of standard scientific practice as formulated in the statutes of Johannes Gutenberg-University Mainz to insure standard scientific practice.

……………………………

(Yinzhou Guo)

Abstract

In the design of new materials, not only different chemical composition but also different structures lead to different properties. At the molecular level, different atoms can be assembled in a controlled manner to form molecules with varying structures by changing the composition of the atoms and the type of bonds present between them. This results in different molecules having various properties. At the colloid level, the assembly of colloidal building blocks could potentially have a similar variety. However, until now, we have a limited number of methods to control the self-assembly of the colloidal particles, especially to control the type of "bonds" controlling the orientation of the colloids in the assembled structure. Consequently, the ability to form different supra-colloidal structures with a rational design remains an open challenge.

In order to develop a methodology to control the formation of more complex supracolloidal structures, diverging from the common close-packed structures, there is a need to introduce directionality in the assembly process. One of the keys to successfully do so is to introduce directionality in the structure of the nanoparticle. Among the methods that can create this directionality is the use of patchy polymer nanoparticles or anisotropic metal particles.

The first target for the design of patchy nanoparticles with distinct shapes was binary particles of gold with patches of cerium oxide. Gold nanosphere, gold nanorod, and gold nanotriangle were used as the template for the growth of the cerium oxide domains. Then, the resulting nanoparticles were used to catalyze model reactions in suspensions. The gold nanoparticles covered with patches of cerium oxide outperformed the fully covered and the naked nanoparticles in terms of catalytic efficiency. Finally, the most efficient heteronanostructures were successfully embedded in nanofibrous membranes by colloidal electrospinning and used in water remediation experiments in a flow-through reactor (Section 4.1).

A second target for the introduction of directionality in the formation of supracolloidal structures is the formation of 1D colloidal chains made by the assembly of polymer functionalized nanoparticles in suspension (Sections 4.2 and 4.3). By controlling the coverage of the nanoparticles with the polymer chains (Section 4.2) and the quality of the solvent (Section 4.3) it is possible to form different supracolloidal structures went complementary nanoparticles are combined. The shape of the core and the interaction between the polymer patches play an essential role in the formation of the colloidal chains. The formation of directional assemblies can be observed both with directional building blocks (Section 4.2) or isotropic building blocks (section 4.3). The formation of directional chains or non-directional close-packed aggregates can be controlled by changing the condition, such as light and solvent quality. Furthermore, the same principles can also be used for the formation of 2D structures by confining the assembly at an interface. 2D colloidal monolayer film also can be prepared by patchy polymer-metal anisotropic nanoparticles via the Langmuir−Blodgett technique (Section 4.4).

This work clearly demonstrates how the formation of supracolloidal assemblies can be used to prepare functional materials. Furthermore, this work provides design rules to generate complex supracolloidal structures by controlling the interaction between the building blocks.

Zusammenfassung

Bei der Entwicklung neuer Materialien führen nicht nur unterschiedliche chemische Zusammensetzungen, sondern auch unterschiedliche Strukturen zu unterschiedlichen Eigenschaften. Auf molekularer Ebene können verschiedene Atome auf kontrollierte Weise zusammengesetzt werden, um Moleküle mit unterschiedlichen Strukturen zu bilden, indem die Zusammensetzung der Atome und die Art der zwischen diesen vorhandenen Bindungen geändert werden, und die verschiedenen resultierenden Moleküle haben verschiedene Eigenschaften. Auf Kolloidebene könnte die Anordnung möglicherweise eine ähnliche haben, aber bis jetzt haben wir eine begrenzte Anzahl von Methoden, um die Selbstorganisation der kolloidalen Partikel zu steuern, insbesondere um die Art der "Bindungen" zu steuern, die die Orientierung der Kolloide steuern in der zusammengebauten Struktur. Folglich bleibt die Fähigkeit, mit einem rationalen Design verschiedene suprakolloidale Strukturen zu bilden, eine offene Herausforderung.

Um eine Methodik zur Steuerung der Bildung komplexerer suprakolloidaler Strukturen zu entwickeln, die von den üblichen Close-Pack-Strukturen abweichen, muss die Richtwirkung in den Montageprozess eingeführt werden. Einer der Schlüssel dazu ist die Einführung von Direktionalität in die Struktur des Nanopartikels. Zu den Verfahren, die diese Richtwirkung erzeugen können, gehört die Verwendung von fleckigen Polymer-Nanopartikeln oder anisotropen Metallpartikeln.

Das erste Ziel für das Design von fleckigen Nanopartikeln mit unterschiedlichen Formen waren binäre Goldpartikel mit Flecken von Ceroxid. Goldnanosphäre, Goldnanostab und Goldnanowinkel wurden als Vorlage für das Wachstum der Ceroxiddomänen verwendet. Dann wurden die resultierenden Nanopartikel verwendet, um Modellreaktionen in Suspensionen zu

katalysieren. Die mit Ceroxidflecken bedeckten Goldnanopartikel übertrafen die vollständig bedeckten und die nackten Nanopartikel hinsichtlich der katalytischen Effizienz. Schließlich wurden die effizientesten Heteronanostrukturen durch kolloidales Elektrospinnen erfolgreich in Nanofasermembranen eingebettet und in Wassersanierungsexperimenten in einem Durchflussreaktor verwendet. (Kapitel 4.1).

Ein zweites Ziel für die Einführung von Direktionalität bei der Bildung suprakolloidaler Strukturen ist die Bildung von 1D-Kolloidketten, die durch Zusammenbau polymerfunktionalisierter Nanopartikel in Suspension hergestellt werden (Kapitel 4.2 und 4.3). Durch die Kontrolle der Bedeckung der Nanopartikel mit den Polymerketten (Kapitel 4.2) und der Qualität des Lösungsmittels (Kapitel 4.3) ist es möglich, verschiedene suprakolloidale Strukturen zu bilden, wobei komplementäre Nanopartikel kombiniert werden. Die Form des Kerns und die Wechselwirkung zwischen den Polymerpflastern spielen eine wesentliche Rolle bei der Bildung der kolloidalen Ketten. Die Bildung von gerichteten Ketten oder nicht gerichteten dicht gepackten Aggregaten kann durch Ändern der Bedingungen wie Licht- und Lösungsmittelqualität gesteuert werden. Darüber hinaus können dieselben Prinzipien auch für die Bildung von 2D-Strukturen verwendet werden, indem die Baugruppe an einer Grenzfläche begrenzt wird. Ein kolloidaler 2D-Monoschichtfilm kann auch durch fleckige anisotrope Polymer-Metall-Nanopartikel über die Langmuir-Blodgett-Technik hergestellt werden (Kapitel 4.4).

Diese Arbeit zeigt deutlich, wie die Bildung suprakolloidaler Anordnungen zur Herstellung von Funktionsmaterialien verwendet werden kann. Darüber hinaus liefert diese Arbeit Entwurfsregeln zur Erzeugung komplexer suprakolloidaler Strukturen durch Steuerung der Interaktion zwischen den Bausteinen.

Contents

1. Introduction

"There is nothing you can't build, only what you can't think of". This is a famous advertising slogan of Lego in China. Children use these captivating blocks to build their dream structures; everything is possible, from a vehicle that moves on the road to one that travels on the water. Some of those children grow up to be scientists, and they discovered a new set of building blocks; they use nanotechnology to bring their dream structures into a much smaller world—the colloidal world. Using nanocolloids as building blocks, the size of the structures built can go down to the nanometer range, but the possibilities are expanding. Today, scientists have access to a wide range of functional nanocolloids that display exciting properties. The assembly of these colloids with other nanocolloids or with polymers can yield functional materials. For example, such supracolloidal assemblies were used as sensor,[1] optical devices,[2] etc… Nanoparticles embedded in a fiber can efficiently kill bacteria and are widely used to design antimicrobial fabrics.[3] Electronic skin with nanoparticles sensitive to pressure, humidity, and temperature can be used for robots and prosthetic limbs.[4]

To control the properties of the supracolloidal assemblies, one strategy is to use different nanocolloids that have distinct intrinsic properties. In addition to the chemical composition, one factor providing a lot of flexibility is to tune the size and shape of the colloidal building blocks. Moreover, anisotropic nanoparticles can show different properties by comparison to isotropic nanoparticles, such as different optical absorption or different catalytic activity. Those different properties can enable countless new applications.[5] The variety of anisotropic nanocolloids made of noble metal and semiconductor with different shapes, such as stars, flowers, wires, triangles, and plates, have prompted the development of a host of applications including sensing, imaging, photothermal therapy, catalysis,[6-9] and data storage.[10]

Moreover, during the formation of supracolloidal structures, for example, through self-assembly, new collective properties can arise. In comparison to individual nanoparticles, the complex supracolloidal structures can display new properties due to the alignment or the interaction between the colloidal building blocks. For example, the directional assembly of the stretched carbon nanotubes (CNTs) covered with gold nanorods in a thermosensitive polymer matrix (polyvinyl alcohol) resulted in nanocomposites displaying broadened absorption bands as a result of end-to-end plasmon coupling between neighboring nanorods.[11] Many new complex structures of superparticles, each having unique properties, including icosahedral, decahedral, and single-crystalline fcc clusters, are produced by colloidal assembly in droplets.[12-14] Alternatively, plasmonic substrates with an excellent surface-enhanced Raman scattering (SERS) sensitivity can be produced by the assembly of gold nanorods, which can be used to design more sensitive sensors.[15, 16] Those supracolloidal structures all show properties that differ from those of the individual nanoparticle used to build the assembly.

Therefore, it is necessary to control not only the chemical composition of the nanocolloids used in the formation of these complex structures but also the directionality of the building blocks within those complex "dream structures" in order to achieve the desired properties and functions of the assembled material. Compared to the Legos of our childhood, we have not yet been able to bring the same level of complexity in the assembly at the nanoscale. However, we have now developed many types of nano-building blocks with different architectures and functions. However, we still need to develop strategies to assemble them in more complex assemblies to harness all of their potentials. A convenient way to produce such structures is to combine the nanocolloids with polymers. Gaining more control over the supracolloidal assembly would pave the way to a new generation of functional materials.

2. State of the art

Different strategies have been used to prepared complex supracolloidal assemblies. A critical challenge in the formation of intricate structures using colloidal building blocks is to introduce directionality and controlling the orientation of the building blocks within the supracolloidal assemblies and the orientation between the building blocks. Such directionality can be provided either by the design of the nanocolloids in the production of anisotropic nanoparticles, or in the method used to generate the assemblies.

2.1 Anisotropic nanoparticles

Anisotropic nanoparticles are powerful building blocks for the formation of assembled materials. They have morphological anisotropy and can also display chemical anisotropy. This anisotropy can be used to direct and control the formation of supracolloidal assemblies. Different synthetic approaches, and different chemical compositions of the nanoparticles are manners to control the structures and properties of the anisotropic nanoparticles.

2.1.1 Anisotropic polymer nanoparticles

There are many methods to generate isotropic nanoparticles on the nano- and micro- scale. However, the synthesis of anisotropic polymer nanoparticles is more intricate and requires more complex synthetic procedures such as controlled evaporation-driven assembly in emulsion,[17] micellar polymer self-assembly,[18] or by the application of external forces to deform isotropic nanoparticles.[19] Among those, solvent-evaporative emulsion and assembly of polymers are versatile and general methods to produce anisotropic polymer nanoparticles on a large scale with various starting materials.

Controlled evaporation-driven assembly in emulsions is a convenient method for the preparation of well-defined, shape-tunable polymer particles. In order to produce anisotropic polymer nanoparticles, either a block copolymer or a mixture of homopolymers is first dissolved in an organic solvent. Then, two immiscible liquid phases (polymer-containing organic solution and aqueous surfactant solution) are sheared with ultrasonicators or homogenizers. The nanodroplets are stabilized against coalescence and Ostwald ripening by the presence of surfactants.[20, 21] As the organic solvent evaporates from the emulsion droplets, the size of the polymer-containing droplets decreases until nucleation of ordered polymer domains is initiated near the interface between the droplet and the surrounding aqueous solution. When the solvent continues to evaporate, the order propagates into the particle center.[22] (**Figure 2.1**) Using this method, a rich variety of novel structured particles with controllable shapes, surface patterns, and internal nanostructures can be produced.[23, 24]

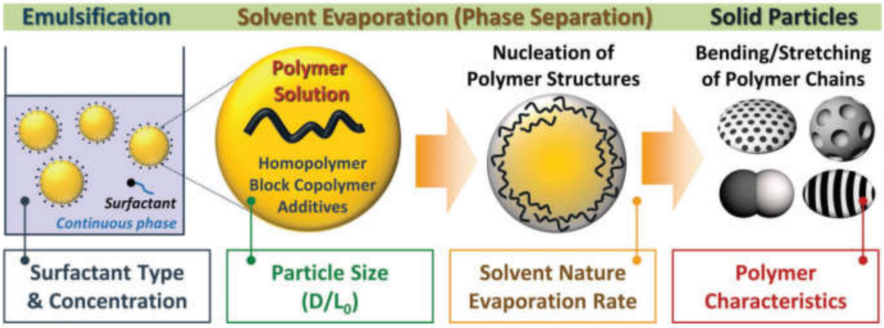

Figure 2.1 Schematic of physical processes that occur during solvent evaporation from a polymer-containing emulsion and factors governing the resulting particle shape. (adapted from ref. 24 with copyright 2018, John Wiley and Sons)

Another method for the production of anisotropic polymer nanoparticles is the self-assembly of (multi)block copolymers. Amphiphilic block copolymers are polymer building blocks that can form polymer nanoparticles by self-assembly. The self-assembled structures obtained depend on the primary structure of the amphiphilic polymer used as the building block: chain length (degree of polymerization: DP), composition (hydrophobic/hydrophilic balance), monomer sequence distribution (e.g., block, random, alternating), and pendant structures.[25-28] For example, Voets *et al.* used the self-assembly of block copolymer poly(acrylic acid)-block-poly(acryl amide) and poly(2-methylvinylpyridinium iodide)-block-poly(ethylene oxide) to form Janus-type micelles in water.(**Figure 2.2**)[29]

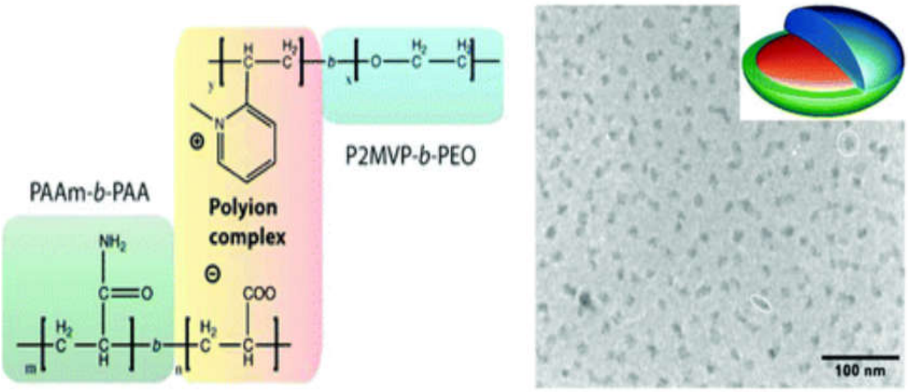

Figure 2.2 structure of the polymers and TEM images of the resulting Janus-type micelles. (adapted from ref. 29 with copyright 2006, John Wiley and Sons)

Another convenient way to produce anisotropic polymer NPs is to selectively change the solvent quality for one segment of the copolymer. [30, 31] While block copolymer usually self-assemble in isotropic spheres or in vesicles, anisotropic structures are also accessible. The most common one is the worm-like micelles, but even more complex structures can be obtained with a clever polymer design. For example, Walther *et al.* synthesized thermoresponsive bis-hydrophilic block terpolymers (PEO-*b*-PnBuA-*b*-PNiPAAm), by changing the temperature, different copolymers with blocks of different length resulted in the self-assembly in different structures. (mixed, multi compartment, or Janus) (**Figure 2.2**).[32] Similarly, Skrabania *et al.* used a"triphilic" copolymers made of oligo(ethylene oxide)monomethyl ether acrylate, butyl or 2-ethylhexyl acrylate, and 1H,1H,2H,2H-perfluorodecyl acrylate to form various structures like patched double micelles and larger soccer ball structures in selective solvents.[33] The variety of the structures accessible through the formation of block copolymer micelles depends on the volume occupied by each segment and the type of interactions between the segments.

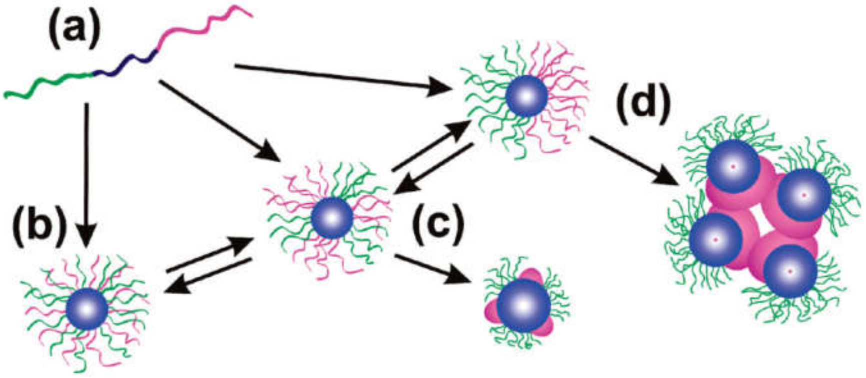

Figure 2.3 Schematic drawing of the self-assembly of block terpolymers PEO-*b*-PnBuA-*b*-PNiPAAm. A block terpolymer (A) with two outer hydrophilic blocks can self-assemble into mixed micelles (B), partly demixed or multicompartment micelles (C) or completely demixed biphasic Janus micelles (D). The amphiphilicity, upon triggering the hydrophilic-to-hydrophobic transition, may lead to the formation of superstructures (adapted from ref. 32 with copyright 2010, American Chemical Society).

The formation of anisotropic polymer nanoparticles can also be achieved using homogenous isotropic polymer nanoparticles as a starting material. The application of external forces to isotropic nanoparticles leads to the deformation of the initially spherical particles and can be used to prepare a variety of anisotropic polymer nanoparticles.[34, 35] For example, Champion *et al.* used spherical polystyrene (PS) particles as a starting material for preparing particles of complex shapes. They embedded the NPs in an elastic matrix, then heated the NPs above the glass transition temperature (T_g). At this point, a stretching deformation was applied in one or two dimensions to change the shape of the PS nanoparticle. After cooling, the anisotropic PS NPs were removed from the matrix (**Figure 2.4**).[35]

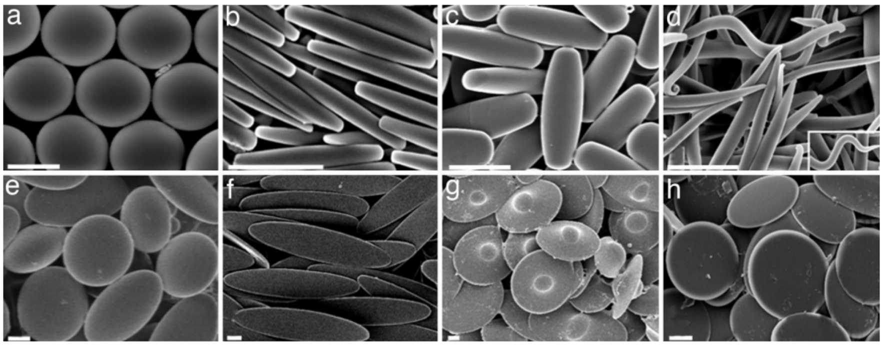

Figure 2.4 Micrographs of anisotropic PS NPs made using matrix-assisted deformation. (A) Spheres. (B) Rectangular disks. (C) Rods. (D) Worms. (E) Oblate ellipses. (F) Elliptical disks. (G) UFOs. (H) Circular disks (adapted from ref. 35 with copyright 2007, PNAS).

2.1.2 Anisotropic metal nanoparticles

Metal particles with nanometer-scale dimensions are of great interest due to their properties, mostly because controlling their shape at the nanoscale can provide access to materials with unique optical, electronic, and catalytic properties. Metals such as gold,[36-38] silver,[39, 40] platinum,[41, 42] and palladium[43, 44] have been used to produce nanoparticles with complex anisotropic shapes. Gold is one of the benchmarks in the preparation of anisotropic metal nanoparticles due to its rapid and controlled crystallization in well-defined shapes.

The seedless growth method is a facile one-pot approach that is commonly used for synthesizing anisotropic gold nanoparticles. This method has a fast reaction speed and yields a variety of final nanoparticles.[45] Also, because the seedless growth method is a one-step synthesis, its operation is more straightforward in comparison to alternative processes.[46, 47] For example, Straney *et al.* obtained gold nanorods and gold nanotriangles with high yield using the seedless growth method,[48] and Umar *et al*. used the seedless growth method to synthesize size-tunable, monodisperse cuboctahedral gold nanoparticles.(**Figure 2.5**).[49]

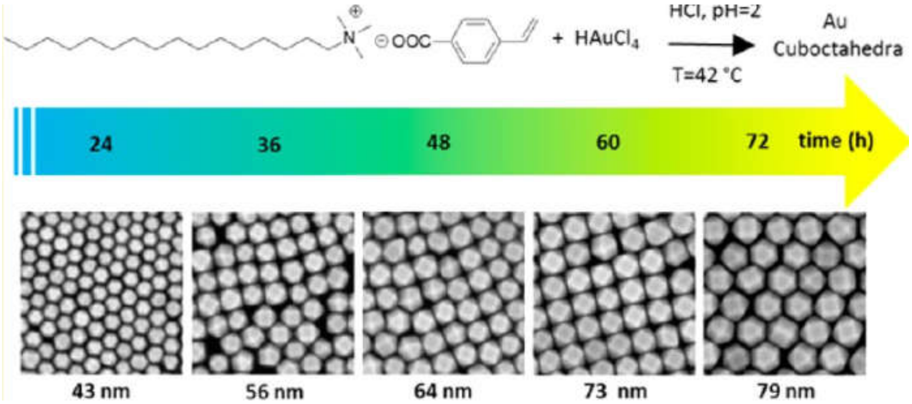

Figure 2.5 Schematic and SEM images of the seedless synthesis of monodisperse cuboctahedral gold nanoparticles with tunable sizes (adapted from ref. 49 with copyright 2005, American Chemical Society).

Even though the seedless growth method is easy and fast, the variety in shape accessible through seedless processes is limited. However, a way to go around that is to use seed growth methods where chemical agents are used to selectively increase the growth of specific crystalline lattices from well-defined seeds. The seed growth method is a popular technique for the synthesis of anisotropic AuNPs. The seed-growth process can be viewed as the step-by-step growth of the NPs, and allows for an easy control of the size and shape of AuNPs (**Figure 2.6**).[50, 51]

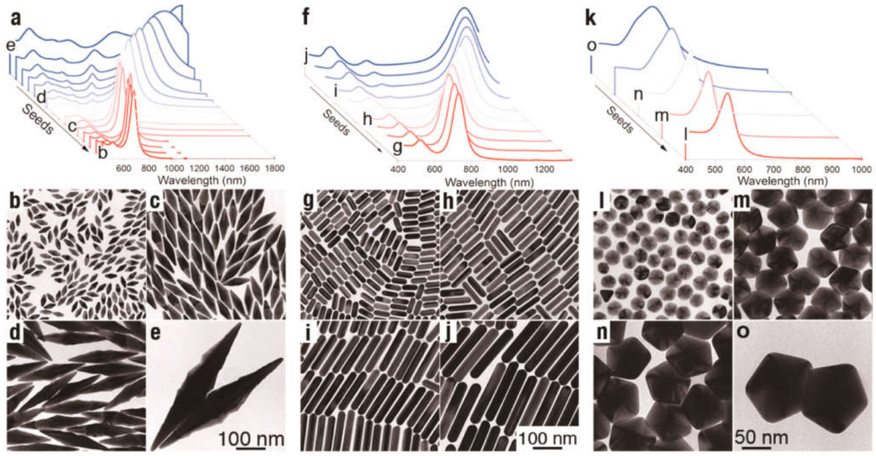

Figure 2.6 Universal character of thermally treated seeds. Effect of seed concentration on the growth of bipyramids (A-E), nanorods (F-J), and decahedra (K-O). (A,F,K) UV-vis-NIR spectra of colloids prepared with different seed concentrations and representative TEM images of nanoparticles prepared in a single growth step from different amounts of seeds (adapted from ref. 51 with copyright 2017, American Chemical Society).

The first step in a seed-growth synthesis is the synthesis of small gold nanoparticle seeds. They can be formed by the reduction of gold salt by sodium borohydride in the presence of a weakly binding ligand such as cetyltrimethylammonium bromide (CTAB).[52-54] Then the second step is the addition of the seeds into the growth solution, which contain additional gold salts, weak reducing agents (e.g., ascorbic acid), and shape-directing agents (e.g., silver nitrate).[55] These reagents interact synergistically to direct the growth of the seed in order to form the anisotropic gold nanoparticles with different shapes. Gold nanorod is a typical example of anisotropic gold nanoparticles[56] produced using a seed-mediated growth approach (**Figure 2.7**). By controlling the shape of the seed (e.g., octahedral, cubic) and the growth conditions, an array of anisotropic NPs is accessible.

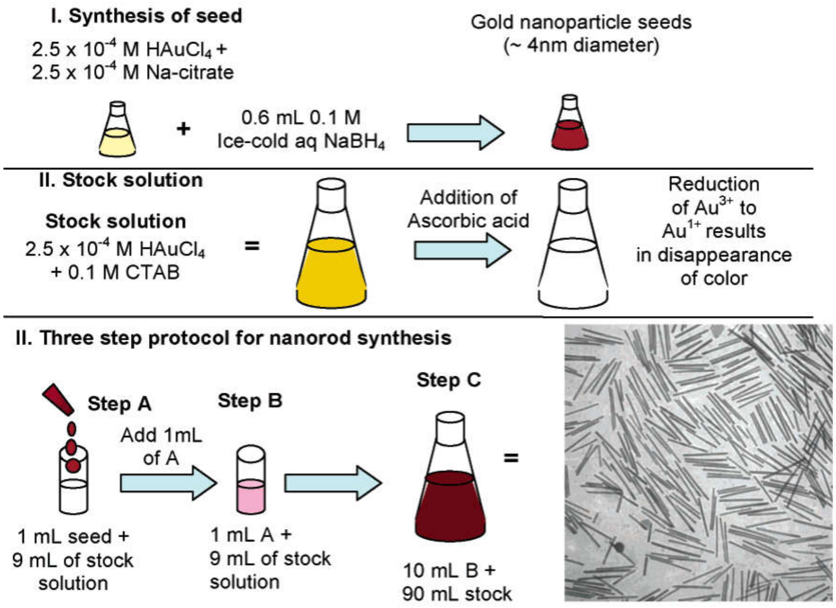

Figure 2.7 Seed-mediated growth approach to making gold and silver nanorods of controlled aspect ratio. The specific conditions are shown here, for 20 mL volume of seed solution, lead to high-aspect-ratio gold nanorods. (bottom right) Transmission electron micrograph of gold nanorods (adapted from ref. 55 with copyright 2005, American Chemical Society).

Traditionally, the reduction of the gold salts in solution is performed by the addition of a reducing agent to the solution. Alternative methods such as pulse radiolysis, can be used for the reduction of the gold salts. For example, Abidi *et al*. produced AuNPs using a ^{60}Co panoramic gamma source to reduced $HAuCl_4$ in the presence of tetraoctylammonium bromide (TOAB) in an aqueous CTAB solution containing a low concentration of silver ions, and they obtained a series of AuNRs with various aspect ratios by varying the silver ion concentration (**Figure 2.8**).[57]

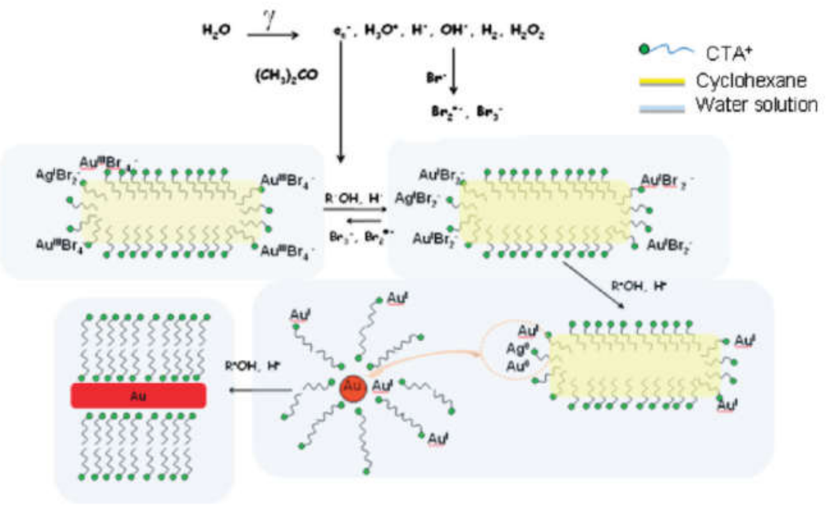

Figure 2.8 Scheme of the reduction and growth mechanism leading to the formation of gold NRs by radiolysis (adapted from ref. 57 with copyright 2010, American Chemical Society).

Another class of methods for the formation of metal NPs is the top-down method, such as lithography.[58] Colloidal lithography has been used to produce large arrays of gold nanoparticles and nanotriangles. The first step consists in using polymer spheres self-assembly to form a hexagonal monolayer. Then in a second step, gold is deposited on the substrate, which is covered by the "colloidal mask" created by the packing of the polymer spheres. After removing the colloidal mask, large gold nanoparticle arrays can be obtained.[59-61] For example, Lohmüller *et al.* used arrays of gold nanotriangles produced by colloidal lithography to track the trajectory of a single protein molecule (**Figure 2.9**).[59] By controlling the conditions used during colloidal lithography, they could control the space between each pair of gold triangles in the final array and consequently tune the properties of the arrays.

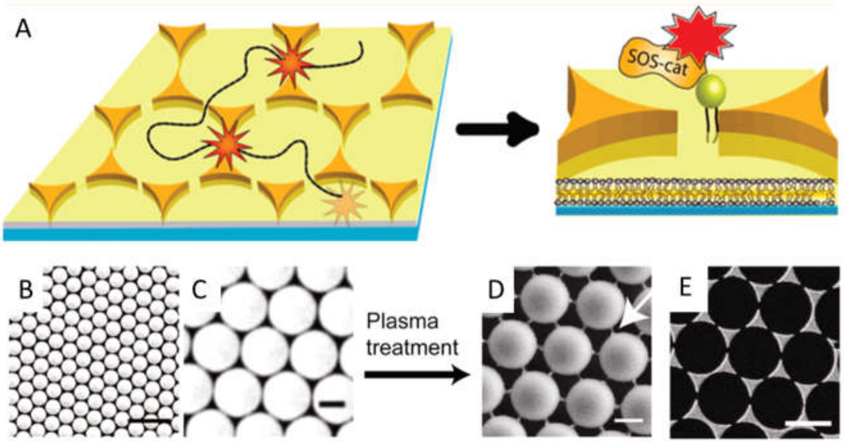

Figure 2.9 (A) Scheme of the gold nanotriangle array with well-defined space used to track the trajectory of a single protein molecule. (B, C) Polystyrene spheres forming a hexagonal monolayer by self-assembly on the solid substrate (scale bar A, 5 µm; scale bar B, 1 µm). (D) Air plasma treatment leads to the formation of connections between individual particles (scale bar: 1 µm). (E) The polymer thread serves as a shadow mask for gold evaporation. After particle lift-off, an array of separated gold nanotriangles remains on the substrate (scale bar: 1 µm) (adapted from ref. 59 with copyright 2012, American Chemical Society).

2.1.3 Anisotropic binary metal nanoparticles

Anisotropic nanoparticles can be built with domains of different compositions using metal nanoparticles as a template. Those binary nanoparticles can be divided into three main types: metal-metal binary nanoparticles, metal-semiconductor binary nanoparticles, and metal-polymer binary nanoparticles. Typically, the binary metal particle can out-perform pure metal nanoparticles in terms of processability, but also by displaying tunable mechanical and new optical properties because of the composition and structure of the resulting hetero-nanoparticles. Because of that, binary metal nanoparticles have been finding applications in various fields, including coatings, optical materials, and biomedical applications.

The overgrowth method is a very common way to produce the metal-metal binary nanoparticles. For example, different shapes of gold nanoparticles can be used as the seed to overgrow another metal on the surface. Scott *et al*. added gold nanotriangles into a K_2PdCl_4 solution with ascorbic acid as the reducing agent and CTAC as the stabilizing agent. After the reaction, core-shell Au-Pd binary nanotriangles were obtained (**Figure 2.10**).[62] One limitation here is the possibility of galvanic replacement of atoms of the initial particles with those used to grow the second domains.[63, 64] Furthermore, different metals have different lattices. The lattice mismatch between two different metals plays a critically important role in the overgrowth of the second metal. A high lattice mismatch will prevent conformal overgrowth. Additionally, the overgrowth of a second metal domain can also be influenced by the surface free energy, and the lowest the interfacial free energy between two different metals is, the easiest will the overgrowth process be.[65, 66]

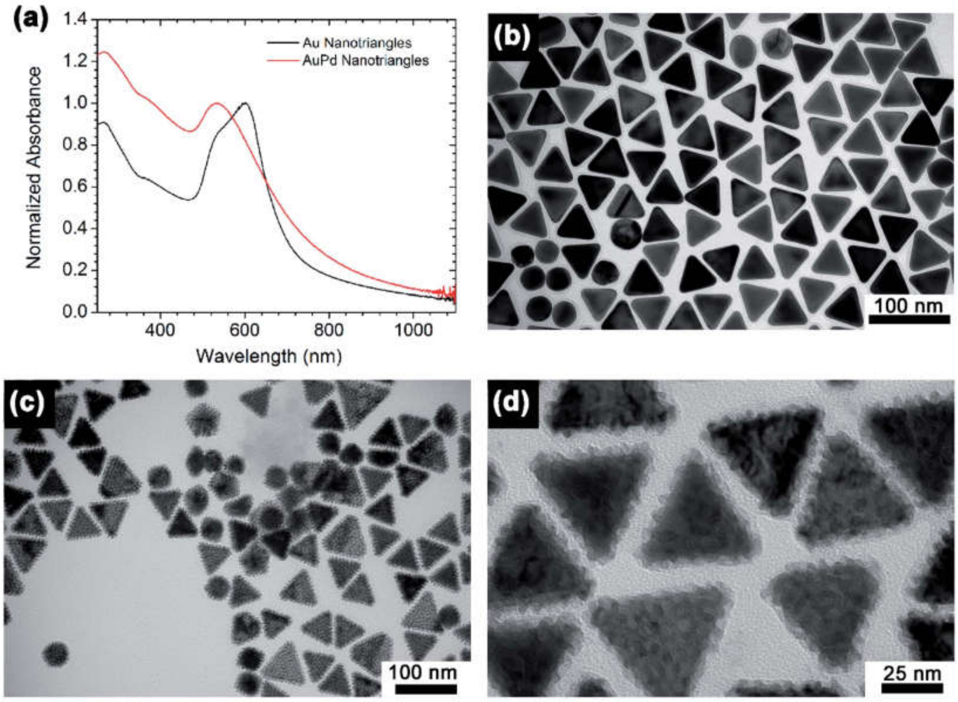

Figure 2.10 (A) Normalized UV-vis spectra of Au and AuPd bimetallic nanotriangles; the spectra are normalized to the maximum of the plasmon band. TEM images of (B) as-synthesized Au nanotriangles, (C) AuPd bimetallic nanotriangles and (D) magnified image of AuPd nanotriangles (adapted from ref. 62 with copyright 2017, RSC Publishing).

The overgrowth method is also used for the synthesis of metal-semiconductor binary nanoparticles. Using anisotropic metal nanoparticles as a seed to do the overgrowth of semiconductors, core-shell structures, or partial coverage of the original metal NPs with domains of semiconductor can be produced. The anisotropy of the final structure depends on the type of seed NPs that are used and the type of semiconductor that is grown on that seed. For example, Huang *et al*. used gold nanorods as the seed to do the overgrowth with Cu_2O in order to obtain Au–Cu_2O core-shell nanorod.[67] Lou *et al*. used gold nanotriangles (Au-TNP) as the seed to do the overgrowth of silver in sulfur solutions. Because sulfur slows down the oxidization reaction rate, Ag_2S showed preferential overgrowth to obtain anisotropic Ag_2S-edged Au-TNPs (**Figure 2.11**). [68]

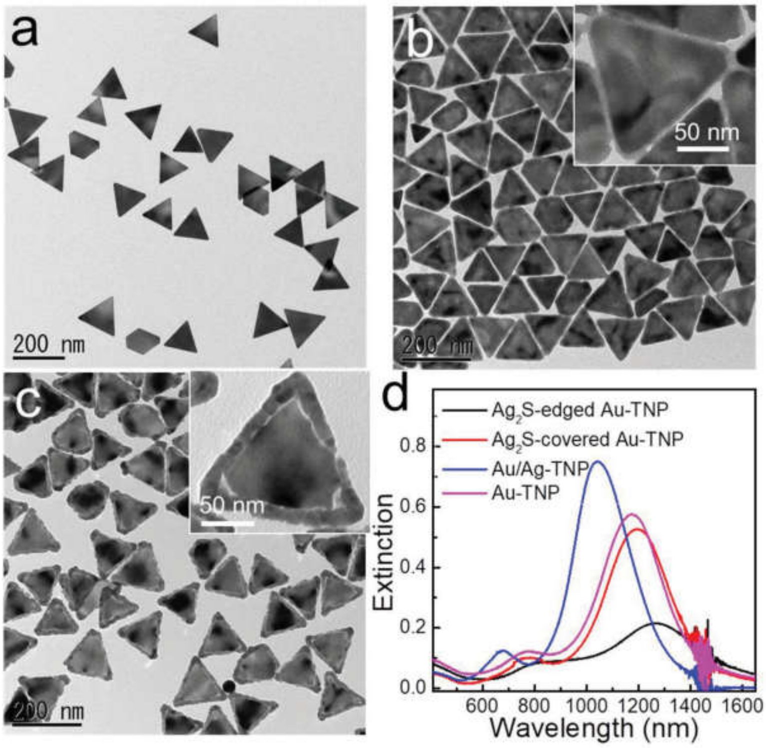

Figure 2.11 (A–C) TEM images of Au/Ag-TNPs (core/shell), Ag_2S-covered, and Ag_2S-edged Au-TNPs, respectively. D) Visible-NIR extinction spectra of Au/Ag-TNPs (core/shell), Au-TNPs, Ag_2S-covered Au-TNPs, and Ag_2S-edged Au-TNPs (adapted from ref. 66 with copyright 2018, John Wiley and Sons).

Finally, metal-polymer binary nanoparticles can be prepared by the functionalization of the surface of metal nanoparticles, such as gold nanoparticles, with polymer chains. The polymer chains can directly be grafted on the NPs surface using preformed polymers or can be grown from initiators immobilized on the NPs surface.[69] In both cases, the functionalization of the surface, either with polymer chains or initiators, can be realized with end-terminated molecules bearing the appropriate functional group to bind to the surface of the NPs. For example, in the case of metal NPs, thiol groups can easily be attached to the surface. Consequently, thiol-terminated polymers have become a popular class of ligands to functionalized gold nanoparticles.[70] For example, Galati *et al.* used thiol-terminated PS to functionalized gold nanoparticles, and by changing the solvent, the surface patterning of PS brushes on the gold nanoparticles was realized (**Figure 2.12**). Furthermore, the PS patches on the gold nanoparticle were dependent on the size and shape of the gold nanoparticles.[69, 71]

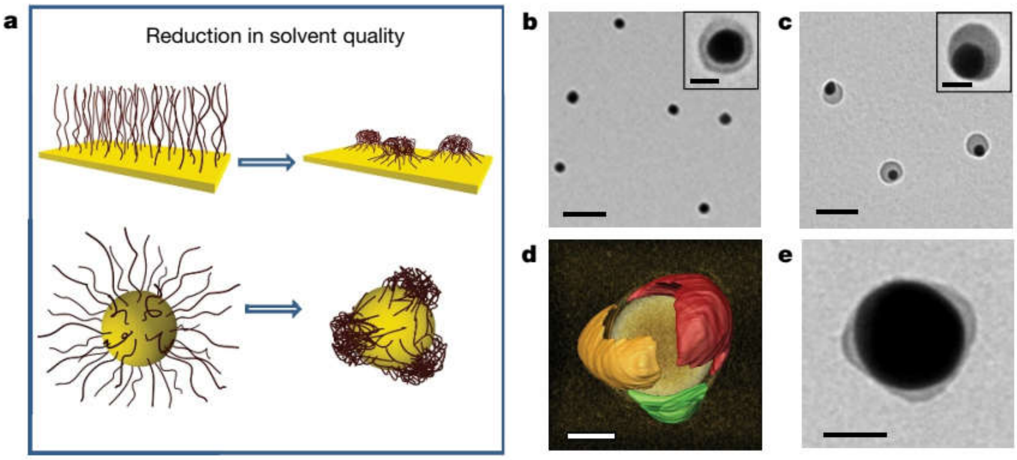

Figure 2.12 Polymer segregation on the nanoparticle surface. (A) Schematics of solvent-mediated formation of pinned polymer micelles (surface patches) on a planar macroscopic surface (top) and on the nanoparticle surface (bottom). (B,C) TEM images of gold nanospheres capped with polystyrene-50K nanosphere solution in DMF (B) and from the DMF/water mixture at $C\text{w} = 4$ vol% (C). (D) Electron tomography reconstruction image of the 60-nm-diameter nanosphere with three polystyrene-50K patches, each shown for clarity with a different arbitrary color. (E) TEM image of the gold nanosphere carrying photocrosslinked thiol-terminated polystyrene-*co*-polyisoprene patches (adapted from ref. 69 with copyright 2016, Nature Publishing Group).

2.2 Assembly of colloidal nanoparticles

Supracolloidal assemblies are highly ordered objects made of nanoparticles, produced by the assembly of those nanocolloidal building blocks, which can occur spontaneously or be templated. Organizing nanoparticles into supracolloidal assemblies can give rise to collective properties or provide new methods for the formulation of functional materials and allows novel possibilities to design functional devices. Assembling nanoparticles into 1D, 2D and 3D supracolloidal assemblies is an excellent way to use nanoparticles as the building blocks to construct hierarchical materials with a precise structure. The interactions and the directions between the building blocks determine the formation and configuration of the supracolloidal assemblies. Furthermore, this configuration of the building blocks affects the final properties of supracolloidal assemblies.

2.2.1 Self-assembly of colloidal nanoparticles

Self-assembly is the process that spontaneous arrangement of building blocks into well-defined ordered complex architectures. An essential parameter in the self-assembly of nanoparticles is the interaction potential between the building blocks defined by their composition, shape, and surface chemistry.

The 1D structures are the most basic type of ordered structure for the supracolloidal assemblies. Various nanoparticles can form 1D supracolloidal assemblies; those with specific geometries, such as nanorods, have advantages in forming 1D supracolloidal assemblies owing to their anisotropic structures.[72] However, it is more challenging to form well-defined 1D supracolloidal assemblies through self-assembly when isotropic building blocks are used. This is due to a lack of directional interactions arising from the isotropic nature of spherical nanoparticles. Nonetheless, linear 1D assembly can be formed, providing a fine balance between steric interactions and electrostatic repulsion. For example, Zhang *et al.* reported a general method that used molecular clusters to fabricate a 1D supracolloidal assemblies. In their work, isotropic spherical nanoparticles can aggregate into wide linear polymer-like single-nanoparticle chains of up to 1000 close-packed nanoparticle components (**Figure 2.13**).[73]

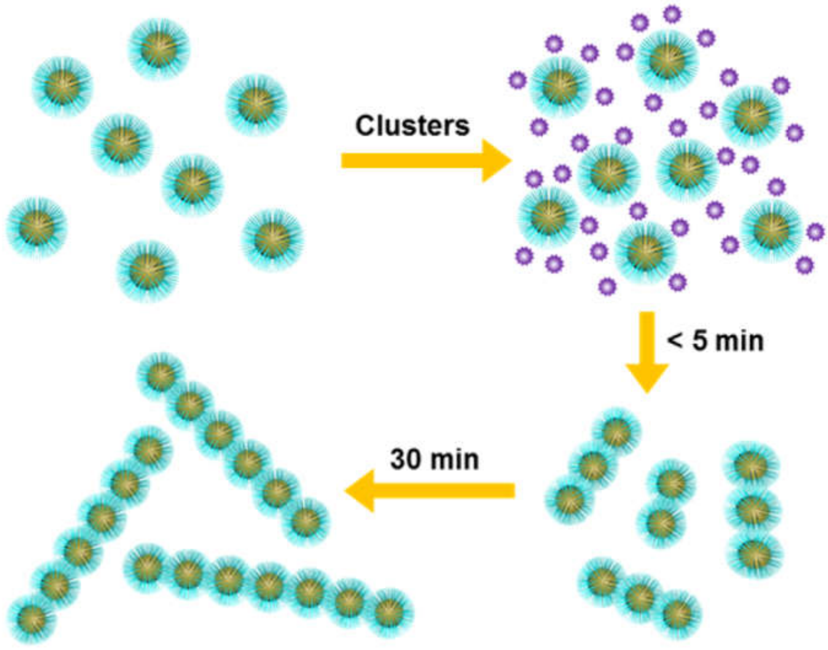

Figure 2.13 Schematic illustration of the self-assembly process of 1D NC superlattice chains in solution in the presence of molecular clusters.(adapted from ref. 71 with copyright 2012, American Chemical Society).

In addition to 1D assemblies, 2D supracolloidal assemblies with close-packed or non-close packed structures can also be generated by self-assembly. Typically, 2D structures are fabricated at the air-liquid interface assembly, or by evaporation-deposition and/or electrophoretic-deposition methods.[74-76] Those methods can be used independently, or in combination, even to form large scale 2D supracolloidal assemblies, using Langmuir–Blodgett deposition[77], template assembly[78], spin coating[79], etc.

Performing the self-assembly of nanoparticles at the interface between two phases is a prevalent method to produce 2D supracolloidal assemblies. Amphiphilic nanoparticles segregate at the interface between two liquids or at the liquid-air interface, and by controlling the concentration of NPs, it is possible to tune the structure of the resulting NP array. For example, Lu *et al.* used acrylamide functionalized gold nanoparticles to do the self-assembly into a monolayer film at the liquid-liquid interface. A chemically cross-linked film with a close-packed array of NPs was formed with high macroscopic uniformity and excellent free-standing property through the photopolymerization of the acrylamides. The resulting film was able to undergo controlled shrinkage under irradiation with UV-light enabling the tunning of the SERS activity of the film (**Figure 2.14**).[80]

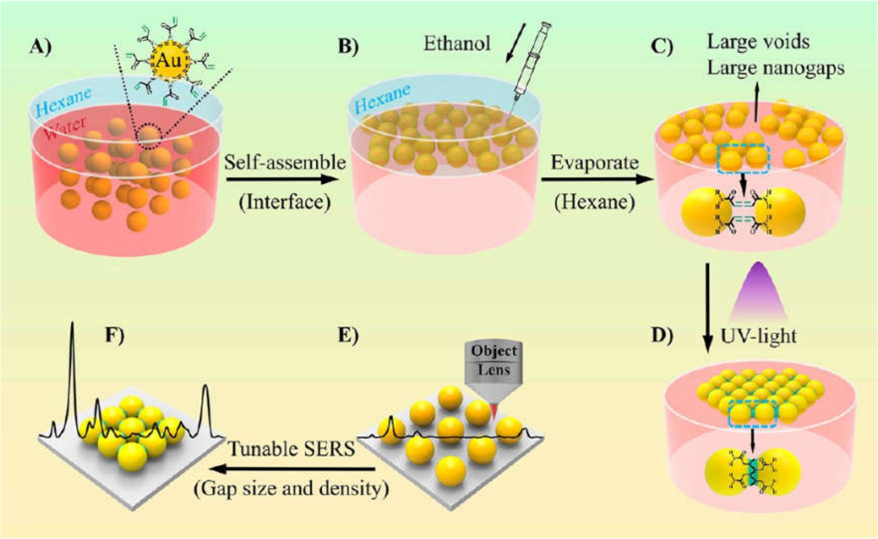

Figure 2.14 Schematic illustration of shrinkable Au NP monolayer films induced by interfacial cross-linking at the air-water interface. (A) The hexane was carefully introduced in the aqueous solution of acrylamide-modified Au NPs for the formation of an immiscible interface. (B) The interface trapped Au NPs by the addition of ethanol. (C) Evaporation of hexane resulted in SAMs with large voids and large nanogaps between NPs. (D) Light-controlled shrinkage and cross-linking of SAMs. (E, F) The SAMs were transferred onto silicon wafers for tunable SERS via changing the size and density of nanogaps (adapted from ref. 78 with copyright 2018, American Chemical Society).

Finally, 3D supracolloidal assemblies have received widespread attention due to their interesting optical properties. The fabrication of 3D supracolloidal assemblies commonly occurs at air-liquid and liquid-liquid interfaces or directly on substrates.[81] Their fabrication formation can be induced by solvent evaporation,[82] gravitational sedimentation[83] and by changing the conditions such as pH value,[84] or light.[85] In general, the assemblies are normally polyhedral blocks and are dominated by either a face-centered cubic (*fcc*) or a body-centered cubic (*bcc*) structure in most cases, because those close-packed structures are the colloidal arrangements that display the minimal conformational energy.[86, 87] The self-assembly of colloidal nanoparticles directly in suspension can also form 3D supracolloidal assemblies. For example, the self-assembly of polymer or silica nanoparticles in well-ordered 3D colloidal crystals has been widely used to generate colorimetric sensors.[88, 89]

2.2.2 Directed assembly of colloidal nanoparticles

During self-assembly, the relative orientation of the nanoparticles changes spontaneously to form the nanoparticles assemblies. An alternative method for the large-scale assembly of nanoparticles is to use a template to control the distribution of the nanoparticles in space. Moreover, using such directed assembly processes, it is possible to control more easily the formation of directional assemblies of nanoparticles. Directed assembly is a process where the formation of supracolloidal assemblies is aided or modulated using a template, directing agents, or external fields.[90] It may give rise to novel ordered nonequilibrium structures, free from entropy maximization constraints. In addition, the directional control of the particle assembly allows to break the mirror-symmetry of particle arrangements often observed during self-assembly to produce materials with far-reaching applications in optics, magnetics and diagnostics.[91-94] The template can be physical, forcing the nanoparticles to organize in predetermine grooves,[95] or chemical such as liquid crystals,[96] or block copolymers.[97] The template does not always provide physical constrain: shear, electric field and magnetic field have also been used to orient and control the positioning of nanoparticles.

Amongst the techniques used to force the directed assembly leading to the hierarchical ordering of nanoparticles, electrospinning is a simple and effective method. With electrospinning, it is possible to assemble nanoparticles into versatile supracolloidal assemblies, and those assemble structures can cover a large surface-area, and their production is easily scalable. Nanoparticles can be aligned in polymer fibers during the electrospinning process.[98, 99] The preformed nanoparticles are directly added into the polymer solution and stirred until the suspension become homogenous. Then, the nanoparticles/polymer supracolloidal assemblies can be easily prepared by electrospinning, which consists in applying high-voltage power supplied to a stream of the polymer/nanoparticles suspension to draw fibers from the drying solution. The resulting fibers and mats can be used in water purification, wearable electronics, and medical applications.[100-102] For example, He *et al*. used silver NPs and PVA solution to form a free-standing and flexible surface-enhanced Raman scattering (SERS) substrate *via* electrospinning. They control the number of NPs in the fibers by changing the concentration of AgNPs in suspension. After electrospinning, the NP arrays were confined and aligned within the PVA fibers. The resulting free-standing electrospun mat could be used as a SERS substrate with high sensitivity and reproducibility (**Figure 2.16**).[103]

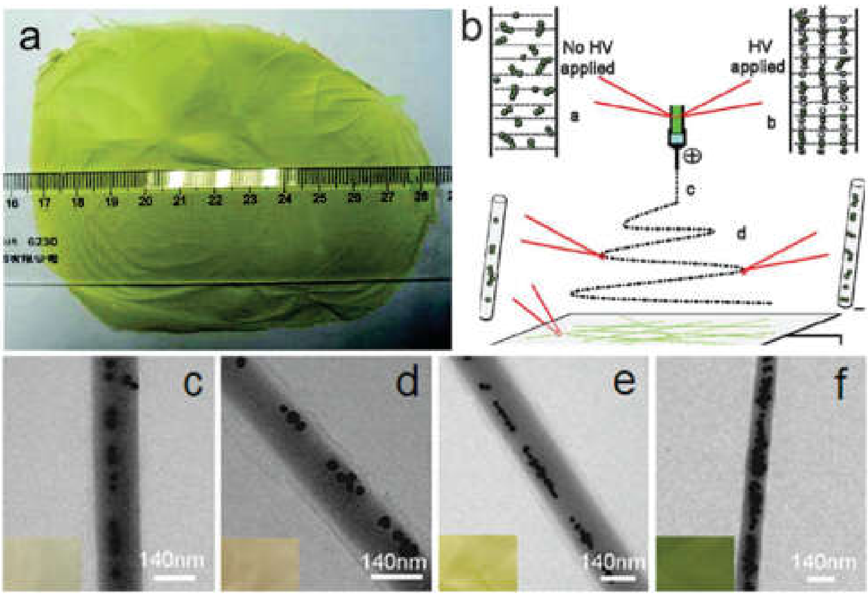

Figure 2.16 (A) Photograph of AgNPs/PVA fibrous mat produced by electrospinning of a solution containing a molar ratio of PVA/Ag of 530 : 3. (B) Schematic illustration of the formation of Ag NP aggregates with chain-like structures within PVA fibers. (C-F) TEM images of AgNPs/PVA fibers with different PVA/Ag molar ratios of 530 : 1, 530 : 2, 530 : 3 and 530 : 4 (adapted from ref. 97 with copyright 2009, American Chemical Society).

Applying external fields, such as electric fields or magnetic fields, is an easy way to induce the assembly of colloidal nanoparticles into one- or two- dimensional supracolloidal assemblies. The external fields can induce interactions between the colloidal nanoparticles. The direction of the external fields can be applied during the assembly process and 1D linear assembly or layered two-dimensional assemblies with directionality can be produced. For example, Collins *et al*. reported reversible phase transitions in 2D colloidal crystals in a negative dielectrophoresis (DEP) cell through the combination of electric field strength and geometric confinement within this electric field. The transformation of the resulting structure was provoked by increasing the dipolar interactions between adjacent particles either by increasing the electric field strength or increasing the lateral compressive forces at the open sides of the traps (**Figure 2.17**).[104]

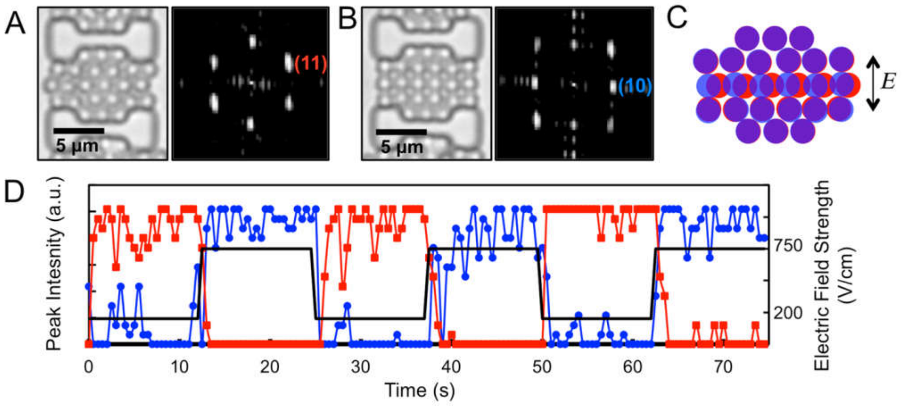

Figure 2.17 (A, B) Optical micrographs and corresponding finite Fourier transforms of colloidal crystals confined within a trap at E = 200 and 750 V/ cm, respectively. (C) Overlay of particle positions in cavities at E = 200 V/cm (red) and 750 V/cm (blue). (D) Intensities of the (11) reflection of hexagonally packed crystals (red) and the (10) reflection of square-packed crystals (blue) in the FFT images of a colloidal crystal confined in a trap (left y-axis) as the applied electric field strength is switched between 200 and 750 V/cm in 12.5 s intervals (right y-axis) (adapted from ref. 98 with copyright 2015, American Chemical Society).

The directed assembly of colloidal nanoparticles in emulsion droplets by solvent evaporation is a standard method to produce 3D supracolloidal assemblies. Wang *et al.* show that "magic number" clusters exist in a confined soft matter system with negligible interactions. Colloidal particles in an emulsion droplet spontaneously organized into a series of clusters with precisely defined shell structures. Free energy calculations demonstrate that colloidal clusters with magic numbers possess higher thermodynamic stability than those off-magic number (**Figure 2.18**).[12]

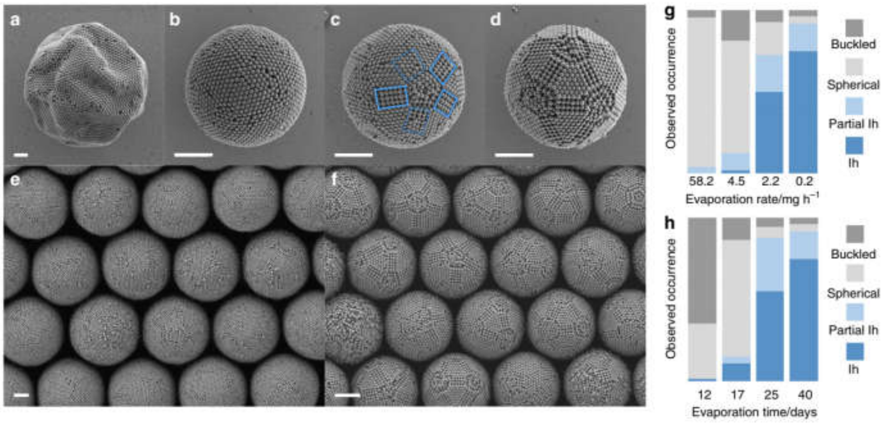

Figure 2.18 Colloidal clusters from confined self-assembly in water-in-oil emulsion droplets. Four distinct cluster morphologies with increasing degree of order are observed:(A) buckled clusters partially collapse upon evaporation into non-spherical shape;(B) spherical clusters exhibit only local order;(C) partial icosahedral clusters show one or more five-fold symmetry axes and incomplete faceting (dotted blue boxes);(D) icosahedral clusters have well-defined facets, edges, and vertices and complete icosahedral symmetry.(E,F) Low-magnification scanning electron microscopy (SEM) images highlight the uniformity in size and structure of the prepared clusters. Spherical and icosahedral clusters dominate in the limit of fast (E) and slow (F) evaporation, respectively. (G,H) Statistical evaluation of the observed morphologies as a function of the evaporation rate (G) and as an evolution over time for the slowest evaporation rate (H) showing the progression from spherical to icosahedral (*Ih*) (adapted from ref. 12 with copyright 2018, Nature Publishing Group).

The structure of the template also has an important influence on the final structure of materials. For example, Dziomkina *et al.* used topologically patterned electrode substrates as a template to control the packing of NPs. They used electrophoresis of charged polymer colloids on those patterned electrode surfaces to direct the assembly and form colloidal monolayers or grow colloidal crystals with different lattice structures. The pattern of the electrode substrates was the determining factor in controlling the structure of the colloidal crystals grown on the electrode (**Figure 2.19**).^{105}

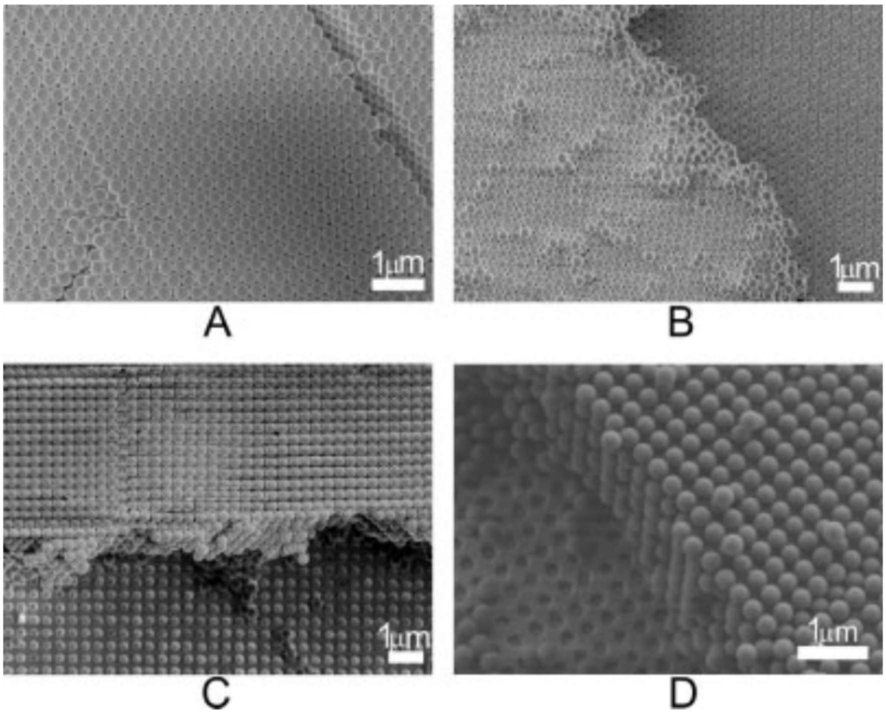

Figure 2.19 (A, B) Colloidal crystals with fcc structures and (111) planes parallel to a hexagonally patterned electrode. (C) Colloidal crystal with *fcc* structure and (100) plane parallel to the square-patterned electrode substrate with pattern periodicity similar to the colloidal size (top view). (D) Colloidal crystal with *bcc* structure and (100) plane parallel to the square-patterned electrode with pattern periodicity corresponding to the bcc lattice for colloids of the appropriate size (adapted from ref. 99 with copyright 2005, John Wiley and Sons).

2.2.3 Directional self-assembly of colloidal nanoparticles

Rather than using templates or templating forces, the self-assembly itself can potentially occur in a directional manner. Creating directionality, or anisotropy, during the self-assembly of isotropic nanoparticles is possible,[106, 107] but challenging since it heavily relies on the delicate balance of attractive and repulsive forces. To control directionality during the self-assembly process, one of the most common methods is to start with anisotropic building blocks.

The ideal building block for directional self-assembly is one that is physically or chemically heterogeneous. Different directing agents have been used to functionalize the colloidal nanoparticles, such as polymers, DNA, and different kinds of small molecules. The surfaces of the resulting nanoparticles have different domains or patches bearing those directing agents. When the molecules used to functionalize the surface can only interact in a specific manner with other patches, or only with a specific subset of patches through a variety of patch-patch interactions, this leads to the self-assembly of the patchy nanoparticles in a controlled direction.[108] An extensive assortment of interactions have been used to build such supracolloidal structures such as covalent molecular interaction, metal coordination[109], host–guest complexation[110], hydrogen bonding[111], and DNA hybridization (**Figure 2.20**).[112]

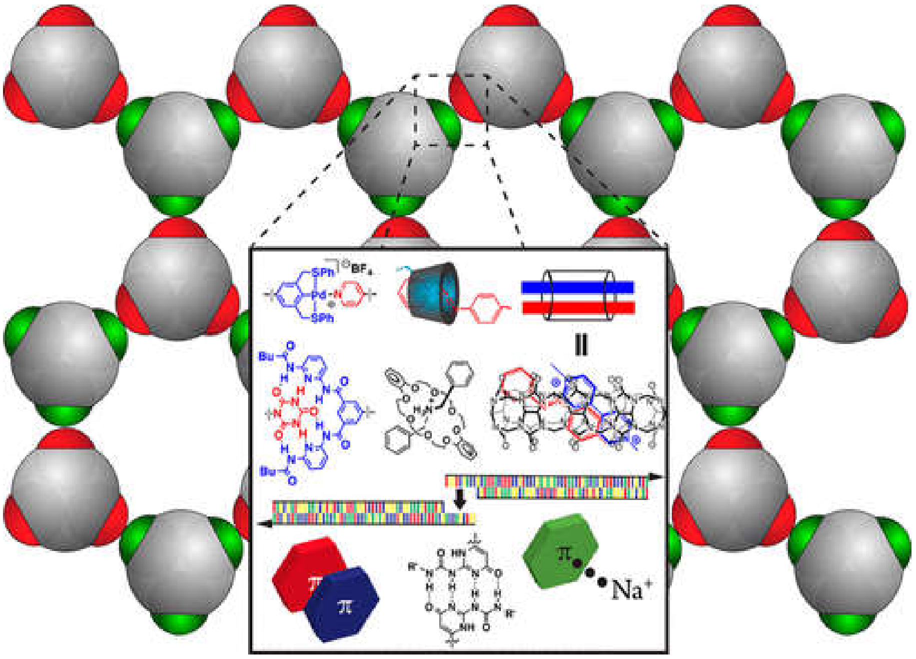

Figure 2.20 Schematic illustration of different kinds of directional noncovalent molecular interactions drive colloidal particles into supracolloidal assemblies by directional self-assembly. Such as metal coordination, host–guest complexation, hydrogen bonding, and DNA hybridization (adapted from ref. 104 with copyright 2017, American Chemical Society).

Such patchy nanoparticles can be prepared in a straightforward manner using anisotropic metal nanoparticles. The different crystal facets present in anisotropic metal nanoparticles have intrinsically different reactivities, and it is possible to use that property to specifically functionalize one type of crystal facet. For example, in the case of gold nanorods, the end of the nanorods exhibit higher index facets and those facets are more reactive toward thiolated molecules. It is thus possible to specifically functionalize the ends of the nanorods without reacting with the sides.

Linear one-dimensional assemblies of colloidal nanoparticles have promising applications in the sensing of chemical and biological species and in the fabrication of waveguides and antennas.[113] Using colloidal nanoparticles functionalized with polymer or DNA chains to control the directionality of assembly is an efficient method to produce the linear 1D supracolloidal assemblies. For example, Liu *et al.* used thiol-terminated PS functionalized at the end of rod-shaped nanoparticles. The addition of water, a non-solvent for the PS, to the suspension of PS-functionalized NRs in dimethylformamide, a good solvent for the PS, triggered the assembly of chains of NRs. After the addition of water, in order to minimize the surface energy of the system in the resulting poor solvent, the patches of PS ligands formed physically bonded patches, and hence, created bonds between the NR ends. This resulted in the end-to-end directional self-assembly and yielded linear 1D supracolloidal assemblies. By using different nanorods as building blocks, the composition of the final 1D supracolloidal assemblies can be tuned (**Figure 2.21**).[114]

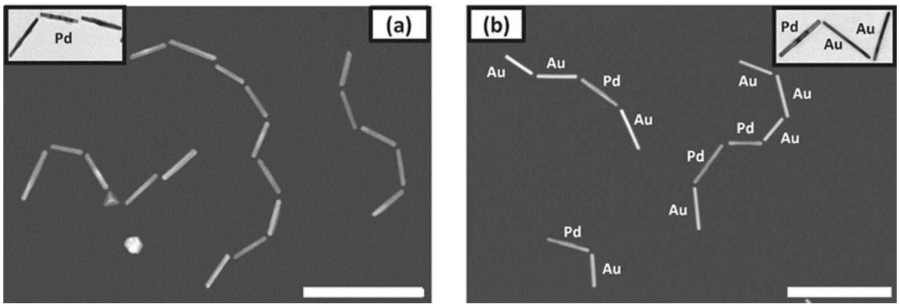

Figure 2.21 Copolymerization of palladium and gold NRs. (A,B) STEM images of (A) homopolymers of palladium NRs, and (B) copolymers of palladium and gold NRs. Insets: high-magnification transmission electron microscopy (TEM) image of fragments of (A) a Pd NR chain and (B) a Pd-Au chain. Scale bars: 500 nm (adapted from ref. 106 with copyright 2014, John Wiley and Sons).

Similarly, directional self-assembly has been used to produce 2D layers. For example, Rong *et al.* selectively functionalized either the transverse or the longitudinal facets of Au NRs with poly(ethylene glycol) (PEG) molecules and used the PEG to guide the directional self-assembly leading to the formation of different directional colloidal arrays. The side-PEGylated Au NRs formed closely packed horizontal arrays, whereas the end-PEGylated Au NRs formed vertically standing arrays on the substrate. The resulting Au NR arrays with different orientations showed anisotropic surface-enhanced Raman scattering (SERS) performance. (**Figure 2.22**)[16]

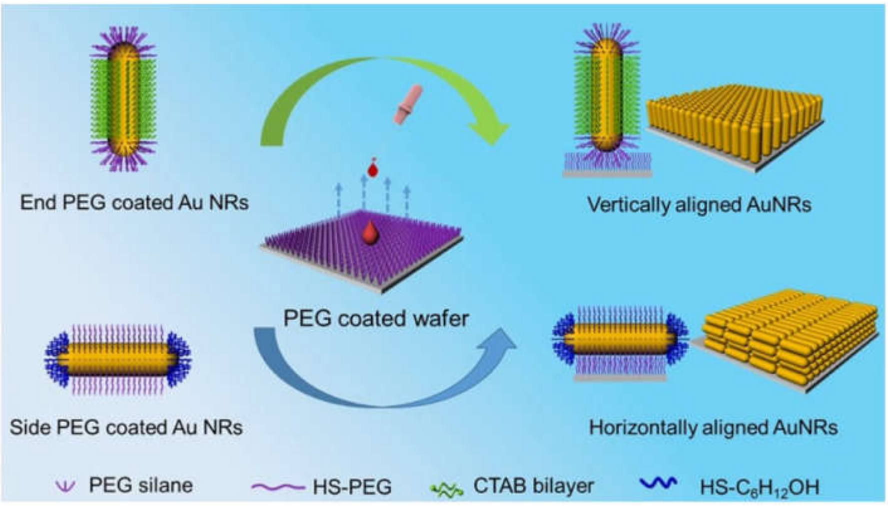

Figure 2.22 Schematic illustration of the fabrication of precisely controlled self-assembled Au NR structures on the substrate (adapted from ref. 16 with copyright 2017, American Chemical Society).

Directional self-assembly in 3D has been used to produce complex colloidal crystals.[115] One of the main limitations in designing colloidal crystals with specific optical properties is that most self-assembled colloidal crystals are face-centered cubic (*fcc*) close-packed structures, since *fcc* structure is the thermodynamically stable conformation with the minimal free energy.[116] Designing non-close-packed colloidal crystals and more complex lattice architectures can increase the width of a photonic stop band because of the reduced volume fraction occupied by the colloids.[117, 118]

The formation of such non-close-packed structures is challenging. It has been achieved by functionalizing patches on nanocolloids with complementary DNA chains to guide the assembly process. Due to the high degree of selectivity of a single DNA strand for a specific matching DNA strand, it is possible to control the direction of the assembly by promoting the assembly between complementary patches. For example, He *et al.* used DNA to functionalized colloidal patchy nanoparticles, using partially compressed tetrahedral clusters with 4 sticky DNA patches. The self-assembly of those particles led to the formation of a colloidal cubic diamond due to the specific matching patch–patch adhesion. The final colloidal diamond has promising optical properties, including a wide and complete photonic bandgap (**Figure 2.23**).[119]

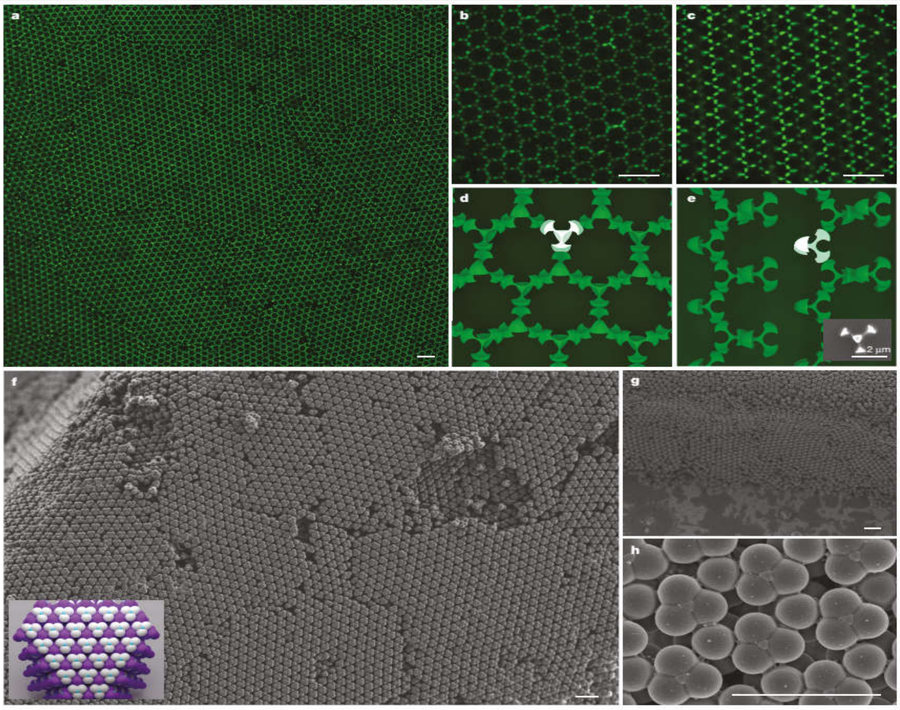

Figure 2.23 Crystallization of cubic diamond colloidal crystals. (A) Confocal microscope image showing the hexagonal symmetry of the 111 plane characteristic of diamond crystals. The signal originates from the fluorescently labeled TPM cores of the tetrahedral cluster patchy particles. (B,C) Magnified confocal images showing the 111 (B) and 110 (C) planes of the cubic diamond crystal. (D,E) Computer-generated images of the TPM patterns expected for the 111 (D) and 110 (E) planes for cubic diamond crystals. A single TPM core within one compressed cluster is highlighted in white. Inset, SEM image of the TPM core, in which polystyrene is dissolved and washed away by THF. (F) SEM images of the 111 plane of colloidal diamond crystals. The crystals are about 40 μm across, with grain boundaries and point defects. Inset, a computer-generated image showing the 111 plane of a colloidal diamond crystal for $d$cc/(2a) = 0.74, consistent with the SEM image. (G) Side view of a crystal edge. The thickness of the crystal is about 10–20 particles. (H) Magnified SEM image of the 111 plane showing the interlocking of particles, as designed. For particles shown in (A,C,F and G) $d$cc/(2a) = 0.73 and b/a = 1.20; in (B) $d$cc/ (2a) = 0.69 and b/a = 1.18; in (H) $d$cc/(2a) = 0.75 and b/a = 1.19. In (A-D, F-H) scale bars are 5 μm (adapted from ref. 111 with copyright 2020, Nature Publishing Group).

2.3 Applications of supracolloidal assemblies

The uniques properties of supracolloidal assemblies enable a wide variety of potential applications, such as sensing, catalysis, solar cells, and biomedical applications. Different building blocks and different structures of supracolloidal assemblies can be obtained by various approaches in different size ranges (nanoscopic, microscopic, and macroscopic) and provide specific functions to the resulting material.

2.3.1 Sensing

Colloidal photonic crystals are composed of periodical modulation of dielectric materials and exhibit photonic band gap.[120] Colloidal photonic crystals can exhibit bright and vivid colors when the “crystal” lattice is in the range of the visible light. This is because the light with certain specific wavelengths or frequencies cannot propagate through colloidal photonic crystals due to the photonic band gap.[121-123] The photonic band gap of the colloidal crystal depends on the size and structure of the colloidal crystal. The position of the band gap depends on both the distance between the colloids and the refractive index of the material between the colloids. Consequently, changing either would result in the shift of the band gap and can be used to design sensors. Colorimetric sensors build with such colloidal 3D structure can respond to various stimuli and lead to fast response speed, high sensitivity and excellent selectivity.[124-126]

For example, Burgess *et al.* used a highly ordered 3D photonic crystal as a regionally functionalized porous carrier to generate complex wettability patterns. The SiO_2 inverse opal films (IOFs) were chemically patterned via multiple iterations of alkylchlorosilane exposure and selective oxygen plasma exposure. The IOF domains with different chemical functionalization displayed different wetting. As specific solvents were able to enter specific domains of the IOF, local modulation of the refractive index within the IOF were observed and led to the selective shift of the band gap in the visible range (**Figure 2.24**). Such IOFs were used as sensors to analyze the hydrophilicity of solvents.[127]

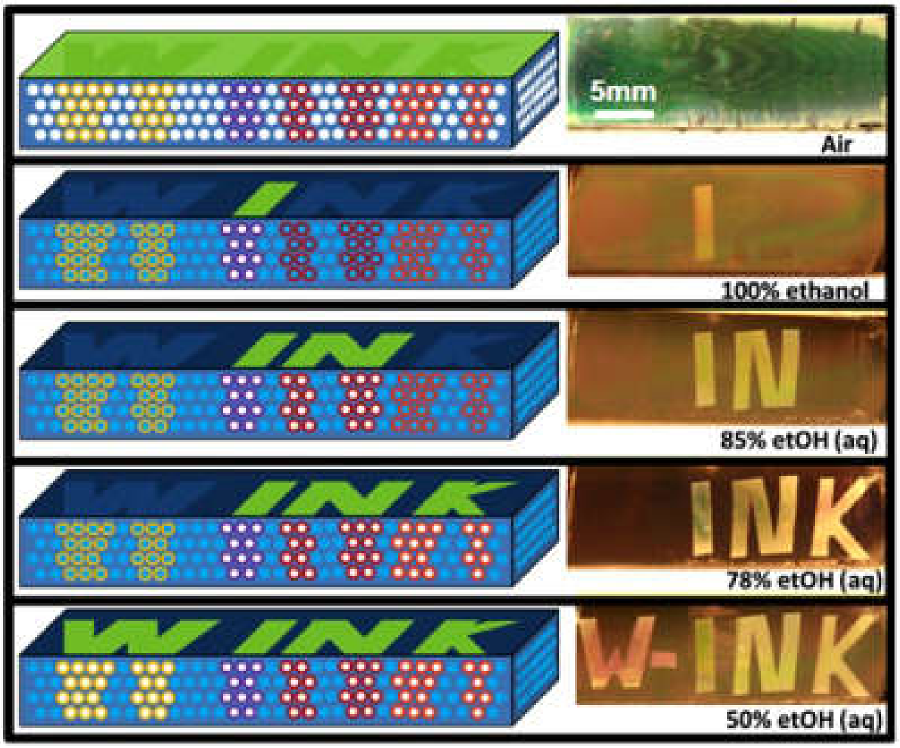

Figure 2.24 Schematic of the chemical encoding procedure and optical images of an IOF in which the word "W-INK" is encoded via the surface chemistry in an IOF: "W-" 13FS, "I" DEC, "N" 3FS, "K" TMS, background ROH. In different water/ethanol mixtures, different words appear (adapted from ref. 120 with copyright 2011 American Chemical Society).

2.3.2 Catalysis

Several metal nanoparticles display very high catalytic efficiency, partially due to their large surface area to volume ratio. While catalytic nanoparticles are intrinsically interesting, their assembly into more complex hybrid supracolloidal assemblies can potentially be superior, mostly in terms of recycling and product purification. Different assembly techniques can potentially be used to embed the catalytic nanoparticles in a convenient and practical supracolloidal assembled material. For example, Hu *et al.*

embedded hematite nanoparticles via colloidal-electrospinning within a supracolloidal nanofibrous polymer membranes. Within the supracolloidal membrane, the mesh made of polymer fibers provided a porous scaffold with high water permeability and the nanoparticles trapped within those fibers acted as a catalyst and efficiently converted H_2O_2 into O_2. Those supracolloidal membranes significantly reduced the harmful effect of high H_2O_2 concentrations during the wound healing process (**Figure 2.25**).[128]

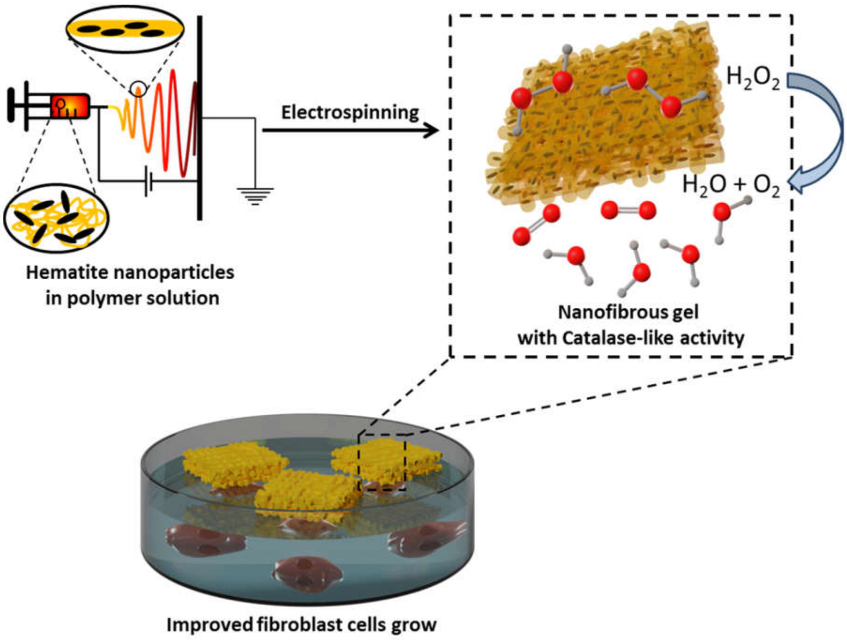

Figure 2.25 Schematic illustration of the fabrication procedure of hematite nanofibrous mats via electrospinning and their use as catalase mimics to convert hydrogen peroxide into water and oxygen to yield an improved fibroblast growth (adapted from ref. 121 with copyright 2017 American Chemical Society).

2.3.3 Biomedical applications

Nanoparticles and their assemblies are being used for biomedical applications such as drug delivery and tissue engineering.[129] The nanoparticles can be directly used as drug carriers to deliver and target the release of drugs. However, supracolloidal assemblies can show improved release properties.[130, 131] Furthermore, the formation of supracolloidal assemblies allow to combine components bringing different functions to the final assembly.[132] For example, Yang *et al.* used superparamagnetic iron oxide nanoparticles and polystyrene-*b*-poly(ethylene oxide) to form supracolloidal magneto-vesicles (MVs). The MVs efficiently encapsulated drugs in their hollow cavity, and the release was controlled by the thickness of the MVs, which was controlled by changing the ratio of polymer and nanoparticles. After intravenous injection, the MVs exhibited drastically enhanced signal in MRI, improved tumor delivery efficiency, and displayed an enhanced antitumor efficacy in comparison to pure polymer micelles or iron nanoparticles (**Figure 2.26**).[133]

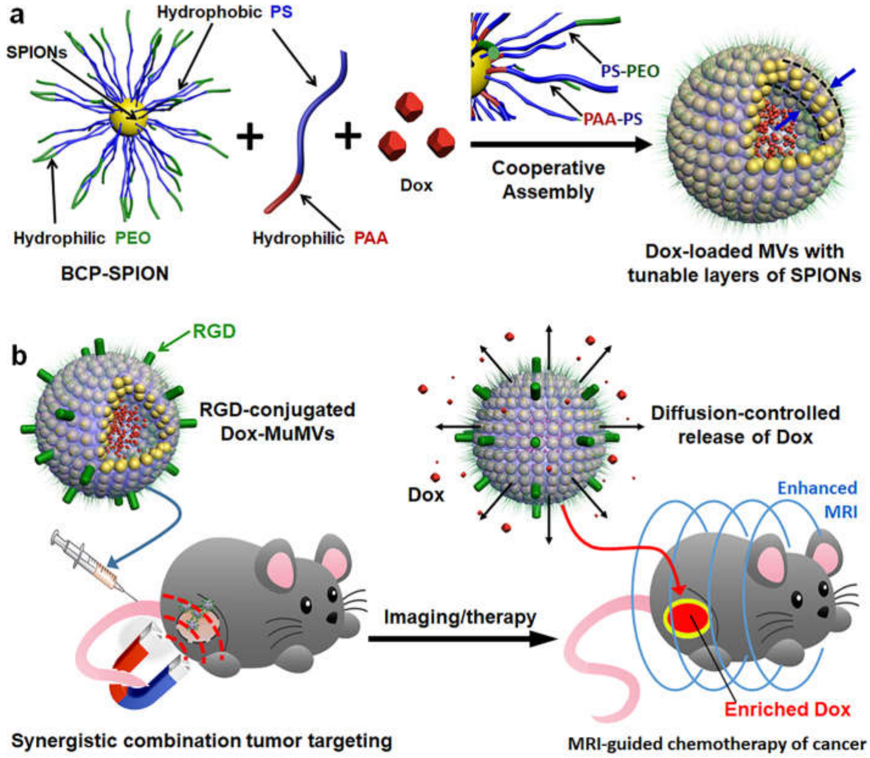

Figure 2.26 (A) Fabrication of MVs with tunable wall thickness via the cooperative assembly of BCP-grafted SPIONs and free PS-*b*-PAA and (B) utilization of MVs for imaging-guided magnetic delivery of Dox into tumor-bearing mice (adapted from ref. 126 with copyright 2018 American Chemical Society).

2.3.4 Energy storage and conversion

Supracolloidal assemblies have been used in the design of materials used for energy storage or conversion. They have been used in the production of solar cells, fuel cells, lithium batteries, and supercapacitors.[134-136] For example, Song *et al.* developed a wavelength-selective supracolloidal crystal concentrator that could selectively converge useful light and filter out unnecessary light for dye-sensitized solar cells (DSSC) based on its photonic band gap properties. The application of the supracolloidal crystal concentrator could effectively improve the output power of the DSSC by more than 5 times and retain the stable high performance of the DSSC (**Figure 2.27**).[137]

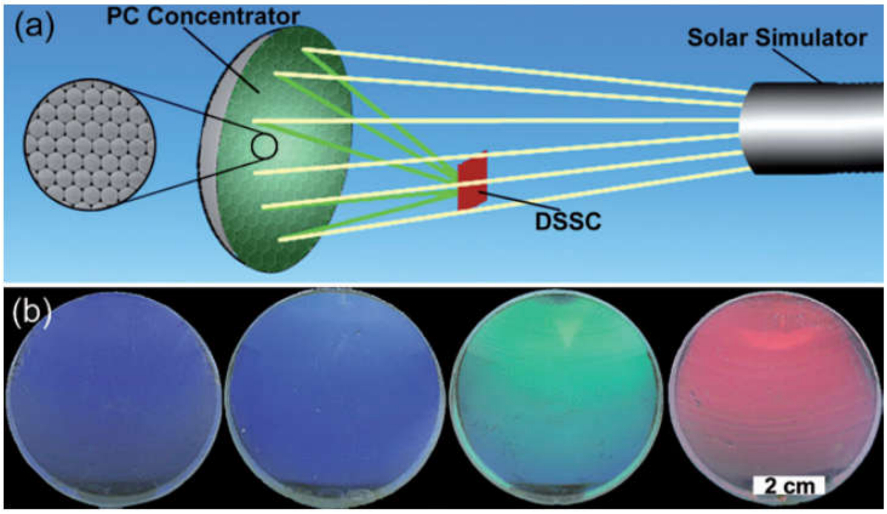

Figure 2.27 (A) Schematic illustration of the photovoltaic system with a PC concentrator. The insert is a typical SEM image of the PC concentrator. (B) Typical photographs of the PC concentrators with different colors, the stopbands of the PC concentrators from left to right are 448, 475, 530 and 647 nm, respectively. The scale bar is 2 cm (adapted from ref. 130 with copyright 2008 RSC Publishing).

3. Experimental section

3.1 Materials

Hydrogen tetrachloroaurate (III) ($HAuCl_4$) (a 40 % solution in dilute hydrochloric acid), sodium hydroxide (NaOH), phenol red, sodium borohydride ($NaBH_4$), ascorbic acid, silver nitrate, potassium iodide (KI), potassium platinum(II) chloride, styrene (St), divinylbenzene (DVB), hexadecane, 2-bromo-2-methylpropanoic acid 3-(triethoxysilyl)propyl ester, methyl methacrylate (MMA), tert-butyl methacrylate (tBMA), acrylic acid (AA), tetraethyl orthosilicate (TEOS), 2-dimethylaminoethyl methacrylate (DMAEMA), 2,2'-azobis(2-methylbutyronitrile) (V-59), 4-cyano-4-(phenylcarbonothioylthio)pentanoic acid (CPAD), 4-phenylazophenol, β-cyclodextrin, 5,5'-dithiobis-(2-nitrobenzoic acid) (DTNB), trifluoroacetic acid (TFA), ethylenediamine (EDA), cetyltrimethylammonium bromide (CTAB), and cetyltrimethylammonium chloride (CTAC) were purchased from Sigma-Aldrich; hydrogen peroxide solution (30%) and cerium acetate were purchased from Roth; poly(vinyl alcohol) (PVA) (Mw = 125,000 $g \cdot mol^{-1}$, 88% hydrolyzed) was purchased from Polysciences Inc.; and glutaraldehyde (GA, 50% aqueous solution) was purchased from Merck. Dimethylformamide (DMF), dichloromethane (DCM), anisole, diethyl ether, n-hexane, ethanol, tetrahydrofuran (THF), copper (II) bromide, ascorbic acid, ammonia, and N,N,N′,N″,N″-pentamethyldiethylenetriamine (PMDETA) were purchased from Acros Organic. V-59 was purified by recrystallization. St, DVB, DMAEMA, tBMA, AA and MMA were purified with a neutral alumina column. Other commercially available chemicals were used as received. The polymerizable ATRP initiator (2-((2-(3-Methyl-2-oxobut-3-en1yl)xy)ethyl)disulfanyl)ethyl 2-bromo-2-methylpropanoate) was synthesized according to the method previously reported.[138] For the synthesis of metal nanoparticles, all the glassware was cleaned using aqua regia (V_{HCl}: V_{HNO3}= 3:1 ratio) followed by rinsing with copious amounts of ultrapure water. All experiments performed in an aqueous environment were conducted using Milli-Q water (pH = 6.90, 18.2 MΩ).

3.2 Synthesis

Synthesis of Au nanospheres (Au NSs)

Au NSs were synthesized using a modified seed-mediated method reported elsewhere.[71] The seed solution was prepared by adding 0.6 mL of a freshly prepared ice-cold solution of $NaBH_4$ (10 mM) to 9.833 mL aqueous CTAB (0.1 M) and then mixed with 0.167 mL of $HAuCl_4$ (15 mM) in a 100 mL Erlenmeyer flask. After vigorous stirring for 2 min, the pale yellow mixture was left undisturbed for 40 min at 25 °C and then diluted to 100 mL with the addition of Milli-Q water. The growth solution was prepared by mixing 4 mL of CTAB solution (0.24 M), 0.133 mL of $HAuCl_4$ (15 mM) and 3 mL of ascorbic acid solution (0.1 M). The growth solution was subsequently diluted to 50 mL with Milli-Q water. Then 0.6 mL of the seed solution was added to the growth medium. The mixture solution was kept in a water bath at 30 °C for 24 h. After the reaction, the excess of CTAB and unreacted species were removed by two cycles of centrifugation (20000 g, 20 min at 25 °C) followed by redispersion in CTAB solution (0.1 mM).

Synthesis of Au nanorods (Au NRs)

Au NRs were synthesized using a seed-mediated growth method.[139] The seed solution was prepared by adding 0.6 mL of freshly prepared ice-cold $NaBH_4$ solution (10 mM) to a mixture containing 0.12 mL of $HAuCl_4$ (15 mM) and 2.5 mL of CTAB solution (0.2 M). The seed solution was kept at 25 °C for 40 min before use. The growth solution was prepared by mixing 5 mL of CTAB solution (0.2 M) with 0.5 mL of $HAuCl_4$ solution (15 mM), 0.4 mL of $AgNO_3$ solution (4 mM), and 4 mL Milli-Q water. The dark yellow growth solution turned colorless after the addition of 0.124 mL of ascorbic acid solution (0.0788 M). Then 0.1 mL of the seed solution was added to the growth solution, and the mixture was reacted in a water bath at 30 °C for 24 h without stirring. After the reaction, the excess of CTAB and unreacted salts were removed by two cycles of centrifugation (18000 g, 20 min at 25 °C) followed by redispersion in CTAB solution (0.1 mM).

Synthesis of Au nanotriangles (Au NTs)

Au NTs were synthesized using a seedless procedure.[45] First, a mixture was prepared by combining 8 mL Milli-Q water, 1.6 mL of CTAC solution (0.1 M), 75 µL of KI solution (0.01 M), 80µL of $HAuCl_4$·solution (25.4 mM) and 20.3 µL of NaOH solution (0.1 M) in a 50 mL Erlenmeyer flask. Once the mixture became homogeneous, 80 µL of ascorbic acid (0.064 M) was added to the reaction. Then, the solution became colorless after 30 s of moderate shaking, and 10 µL of NaOH (0.1 M) was then added quickly under ultrasonication for 5 s. The color of the solution changed from colorless to blue within ca. 20 min. After the reaction, the excess of CTAC and unreacted salts were removed by three cycles of centrifugation (10000 g, 20 min at 25 °C) followed by redispersion in Milli-Q water for the first two cycles and redispersion in CTAB solution (0.1 mM) after the third centrifugation cycle.

Depletion-induced separation of the nanotriangles.

As for Au NTs purification, the suspension of as prepared AuNTs was purified by the depletion-induced separation approach using CTAC at room temperature.[140] First, the concentration of CTAC was increased to 0.2 M. Then, the suspension was kept at room temperature for 12 h without stirring. Then, the supernatant was removed, and the precipitate formed at the bottom of the vial was redispersed in 5 mL 0.1 M CTAC solution. After 12 h, two cycles of centrifugation at 10000 g, 20 min at 25 °C were used to remove the excess CTAC from the suspension. Finally, the AuNTs were redispersed in 0.1 mM CTAB solution.

Synthesis of Au@CeO$_2$ nanosphere

Typically, 1 mL of the as-prepared AuNS suspension was centrifuged (20,000 g, 30 min) and redispersed with 0.5 mL of CTAB solution (0.1 mM). Then, different amounts of K_2PtCl_4 solution (0.1 mM) were added to the AuNS suspension under gentle shaking. To get fully covered AuNS (AuNS@F-CeO$_2$), 50 µL of platinum salt solution was added, and for the partially covered AuNS (AuNS@J-CeO$_2$), 20 µL of the platinum salt solution was added. The resultant suspension was kept at room temperature for 30 min to allow for the adsorption of $PtCl_4^{2-}$ on the AuNS. Then, a freshly prepared Ce(AC)$_3$ solution (10 mM) was added, either 200 µL for the synthesis of AuNS@F-CeO$_2$ or 100 µl for the AuNS@J-CeO$_2$. Then, water was added (250 µL for AuNS@F-CeO$_2$ or 380 µL for AuNS@J-CeO$_2$) to the suspension under gentle shaking. Finally, the resultant suspension was placed in an oven set at 100 °C for 1 h to produce the AuNS@CeO$_2$ binary nanoparticle. The unreacted salts were removed by two centrifugation cycles (15,000 g, 20 min, 27 °C), followed by redispersion in water.

Synthesis of Au@CeO$_2$ nanorod

Typically, 1 mL of the as-prepared AuNR suspension was centrifuged (12,000 g, 20 min) and redispersed with 0.5 mL of CTAB solution (0.1 mM). Then, different amounts of K_2PtCl_4 solution (0.1 mM) were added to the AuNR suspension under gentle shaking. To get fully covered AuNR (AuNR@F-CeO$_2$), 50 µL of platinum salt solution was added, and for the tips covered AuNR (AuNR@T-CeO_2), 10 μL of the platinum salt solution was added. The resultant suspension was kept at room temperature for 30 min. Then, a freshly prepared $Ce(AC)_3$ solution (10 mM) was added, either 200 μL for the synthesis of AuNR@F-CeO_2 or 30 μl for the AuNR@T-CeO_2. Then, water was added (250 μL for AuNR@F-CeO_2 or 410 μL for AuNR@T-CeO_2) to the suspension under gentle shaking. Finally, the resultant suspension was placed in an oven set at 100 °C for 1 h to produce the AuNR@CeO_2 binary nanoparticle. The unreacted salts were removed by two centrifugation cycles (10,000 g, 20 min, 27 °C), followed by redispersion in water.

Synthesis of Au@CeO_2 nanotriangle

Typically, 1 mL of the as-prepared AuNT suspension was centrifuged (1,000 g, 20 min) and redispersed with 0.5 mL of CTAB solution (0.1 mM). Then, different amounts of K_2PtCl_4 solution (0.1 mM) were added to the AuNT suspension under gentle shaking. To get fully covered AuNT (AuNT@F-CeO_2), 100 μL of platinum salt solution was added, and for the edge covered AuNT (AuNT@E-CeO_2), 30 μL of the platinum salt solution was added. The resultant suspension was kept at room temperature for 30 min. Then, a freshly prepared $Ce(AC)_3$ solution (10 mM) was added, either 250 μL for the synthesis of AuNT@F-CeO_2 or 50 μL for the AuNT@E-CeO_2. Then, water was added (150 μL for AuNT@F-CeO_2 or 420 μL for AuNR@E-CeO_2) to the suspension under gentle shaking. Finally, the resultant suspension was placed in an oven set at 100 °C for 1 h to produce the AuNT@CeO_2 binary nanoparticles. The unreacted salts were removed by two centrifugation cycles (800 g, 20 min, 27 °C), followed by redispersion in water.

Synthesis of polystyrene core nanoparticles (PS NPs)

The PS NPs functionalized with an ATRP initiator were prepared using a starve-fed method reported elsewhere.[141] First, a miniemulsion was prepared using 24 mL of 0.3 wt% aqueous solution of SDS used as the dispersed phase and a mixture of 25.3 mmol of styrene, 2.8 mmol of DVB, 0.14 mmol of V-59 and 1.1 mmol of hexadecane used as the dispersed phase. The two phases were mixed together and stirred for 10 min and then emulsified by ultrasonication. The suspension was sonicated in an ice bath for 2 minutes at 70% amplitude in 10-seconds pulses followed by 2-seconds pauses. The emulsified mixture was immersed in an oil bath at 80 °C to initiate free radical polymerization. After 4 h, 2 mL of 7.6 wt% SDS aqueous solution was added to increase the SDS concentration to 0.5 wt%. Then, an organic phase mixture of 5.5 mmol of St, 0.06 mmol of DVB, and 0.03 mmol of V-59 with 1 mmol of ATRP initiator was injected into the reaction vessel at a rate of 1.5 mL/hour. The reaction continued overnight at 80 °C under stirring. The resulting PS NPs were purified by three times precipitation using methanol followed by redispersion in THF and three times precipitation in hexane followed by redispersion in THF and then dried.

Synthesis of PS-poly(methyl methacrylate-*co*-2-(dimethylamino) ethyl methacrylate) and PS-poly(methyl methacrylate-*co*-methacrylic acid) core-canopy NPs (PS-PMMA-*co*-PDMAEMA and PS-PMMA-*co*-PDMAA)

Poly(methyl methacrylate-*co*-2-(dimethylamino)ethyl methacrylate) (PMMA-*co*-PDMAEMA) or poly(methyl methacrylate-*co*-methacrylic acid) (PMMA-*co*-PtBMA) chains were grown at the surface of the PS NPs from the initiating sites using atom-transfer radical-polymerization (ATRP). First, $CuBr_2$ (5 mg, 0.022 mmol) and PMDETA (48 µL, 0.22 mmol) were dissolved in 2.5 mL DMF to prepare a stock solution of Cu(II)/PMDETA. An ascorbic acid solution was prepared by dissolving ascorbic acid (40.5 mg, 0.23 mmol) in 2.5 mL DMF. A suspension of PS NPs was prepared by resuspending 0.1 g of PS NPs (0.026 mmol of initiator) in 2 mL anisole. The suspension was placed in a Schlenk tube and then MMA was added (0.364 mmol, 0.771 mL for short chains; 1.82 mmol, 0.594 mL for long chains), with tBMA (0.156 mmol, 0.051 mL for short chains; 0.78 mmol, 0.253 mL for long chains) or DMAEMA (0.156 mmol, 0.053 mL for short chains; 0.78 mmol, 0.267 mL for long chains). The mixture was degassed through three freeze-pump-thaw cycles. Subsequently, 87.6 μL of the Cu(II)/PMDETA solution and 42.6 μL of the ascorbic acid solution were added to the mixture. The reaction mixture was stirred at 70 °C in an oil bath overnight. The polymerization was stopped by quickly cooling down the reaction mixture to room temperature. The resulting functionalized PS NPs were washed by centrifugation with hexane three times then redispersed in THF.

Synthesis of silica core nanoparticles (Si NPs)

Using a modified Stöber synthesis, ATRP initiator functionalized Si NPs were prepared.[142] A mixture prepared with 7.5 mL ammonium hydroxide (28% in water) and 100 mL ethanol in a 250 mL round-bottom flask was stirred at 300 rpm to get homogenized. Then, the mixture was heated to 40 °C, and 7.5 g of TEOS was added into the solution at a rate of 9 mL/min using a syringe pump. Then, the reaction was kept at 40 °C for 6 h under permanent stirring. Then, 2.4 mmol of TEOS and 0.27 mmol of 2-Bromo-2-methylpropanoic acid 3-(triethoxysilyl)propyl ester were added to the suspension drop-wise. The reaction was kept at 40 °C overnight. Then, the temperature of the mixture was increased to 80°C for 1 h to promote covalent bonding of the organosilane to the surface of the silica nanoparticles.[143] The resulting Si NPs were purified by three centrifugation cycles in methanol at 15000 g for 20 min.

Synthesis of Si-poly(methyl methacrylate-*co*-2-(dimethylamino) ethyl methacrylate) and Si-poly(methyl methacrylate-*co*-methacrylic acid) core-canopy NPs (Si-PMMA-*co*-PDMAEMA and Si-PMMA-*co*-PDMAA)

The polymer-functionalized Si NPs were prepared following the same recipe as the polymer-functionalized PS NPs. The only difference is that 0.186 g of Si NPs (0.026 mmol of initiator) in 5 mL anisole were used to maintain the concentration of initiator in the system constant. The resulting Si NPs were washed by three centrifugation cycles using methanol at 15000 g for 20 min, and then redispersed in THF.

Synthesis of PS-(PMMA-*co*-PMAA) and Si-(PMMA-*co*-PMAA) polymer functionalized nanoparticles

The as synthesized PS-(PMMA-*co*-PtBMA) or Si-(PMMA-*co*-PtBMA) nanoparticles (0.1 g) were dissolved in 10 mL DCM, followed by the addition of 5 mL of TFA. The resulting suspension was stirred for 24 h at room temperature and purified by precipitation in hexane (3X) followed by redispersion in THF.

Synthesis of CTA-poly(methyl methacrylate-*co*-2-(dimethylamino) ethyl methacrylate) and CTA-poly(methyl methacrylate-*co*- methacrylic acid) copolymers

CTA-poly(methyl methacrylate-*co*-2-(dimethylamino) ethyl methacrylate) (CTA-PMMA-*co*-PMAA) and CTA-poly(methyl methacrylate-*co*-methacrylic acid) (CTA-PMMA-*co*-PMAA) were synthesized by RAFT polymerization. CPAD (14.4 mg, 0.052 mmol), AIBN (1.62 mg, 0.01 mmol), MMA (0.728 mmol, 1.542 mL for short chains; 3.64 mmol, 1.188 mL for long chains), tBMA (0.312 mmol, 0.102 mL for short chains; 1.56 mmol, 0.506 mL for long chains) or DMAEMA (0.312 mmol, 0.106 mL for short chains; 1.56 mmol, 0.534 mL for long chains) were mixed with 5 mL THF in a 25 mL Schlenk tube. After degassing through three freeze-pump-thaw cycles, the mixture was placed in a pre-heated oil bath at 75 °C for 24 h under stirring. After polymerization, the solution was cooled down to room temperature and the polymer was precipitated in hexane (3X).

Synthesis of thiol-terminated poly(methyl methacrylate-*co*-2-(dimethylamino) ethyl methacrylate) and poly(methyl methacrylate-*co*-methacrylic acid) copolymers

To transform the end group of the polymer chains to a thiol group, 0.4 g of CTA-PMMA-co-PDMAMEA or CTA-PMMA-co-PMAA was dissolved in DCM, followed by the addition of n-butylamine (3 mL) and stirred at room temperature for 12 h. The polymer was purified by precipitation in hexane (3 h) and dried at room temperature for 24 h.

Synthesis of thiol-terminated poly(2-(dimethylamino)ethyl methacrylate)

CTA-poly(2-(dimethylamino)ethyl methacrylate) (CTA-PDMAEMA) was synthesized by RAFT polymerization. CPAD (14.4 mg, 0.052 mmol), AIBN (1.62 mg, 0.01 mmol), DMAEMA (1.77 mL, 0.312 mmol) were mixed with 5 mL THF in a 25 mL Schlenk tube. After degassing with three freeze-pump-thaw cycles, the mixture was placed in a pre-heated oil bath at 70 °C for 24 h under stirring. After polymerization, the solution was cooled down to room temperature, and the polymer was precipitated in diethyl ether (3X). Then, 0.2 g of CTA-PDMAEMA was dissolved in DCM, followed by the addition of n-butylamine (3 mL). The mixture was stirred at room temperature for 12 h. The polymer was purified by precipitation in diethyl ether (3X) and dried at room temperature for 24 h.

Synthesis of azobenzene monomer (4-methacryloyloxyazobenzene)

First, 4-hydroxyazobenzene (1 g, 5.05 mmol) was dissolved in 12 mL of THF and triethylamine (0.51 g, 5.05 mmol) was added to the solution. The solution was purged with nitrogen and stirred for 30 min at 0 °C. Methacryloyl chloride (1.5 mL, 15 mmol) was injected gradually into the solution at 0 °C in an ice bath. The formation of the triethylammonium salt in the form of a precipitate was observed immediately after the addition of methacryloyl chloride. The reaction mixture was then stirred for 24 h at 25 °C. After the reaction, the resulting precipitate was filtered off. The solution was diluted four times by adding a mixture of $CHCl_3$ and water (3:1). The organic layer was washed three times by extraction with distilled water. Finally, the yellow organic layer was dried with anhydrous Na_2SO_4, and the residual solvent was removed in vacuo. The resulting yellow solid was crystallized twice from n-hexane and dried under high vacuum. ^{1}H NMR (300 MHz, $CDCl_3$) δ (ppm): 7.98–7.89 (m, 4H), 7.54–7.45 (m, 3H), 7.30–7.21 (m, 2H), 6.38 (m, 1H), 5.79 (m, 1H), 2.08 (dd, 3H).

Synthesis of β- cyclodextrin monomer (glycidyl methacrylate-ethylenediamine-beta- cyclodextrin) (GMA-EDA-β-CD)

Mono-6-O-(p-toluenesulfonyl)-beta-cyclodextrin (mono-6-OTs-*β*-CD) was synthesized by first dissolving β-CD (2.5 g) in 6.5 mL of DMSO, followed by the dropwise addition of 3.75 g of p-toluenesulfonyl chloride dissolved in 6 mL of DMSO. The solution was stirred for 24 h at 45 °C. Then, 30 mL of acetone was added dropwise. The CD-derivative immediately crystallized, and a white precipitate was observed. This white precipitate was filtered, rinsed with precooled acetone. This procedure was repeated three times. ^{1}H NMR (300 MHz, DMSO-d_6): d (ppm) 7.75 (d, 2H), 7.43 (d, 2H), 5.58–5.83 (m, 7H), 4.84 (m, 7H), 4.77 (m, 7H), 4.34 (s, 1H), 4.32 (s, 1H), 4.193 (m, 6H) 3.21–3.69 (m, 40H), 2.502 (S, 3H).

Then, 2.0 g of mono-6-OTs-*β*-CD was reacted with an excess of ethylenediamine (EDA) (6 mL) at 75 °C for 4 h. After the reaction, the mixture was cool down to room temperature, and then, 10 mL of cold acetone was added, leading to the precipitation of the product. The precipitate was redissolved in 10 mL of a water-methanol mixture and poured into 10 mL of acetone (3X) for the complete removal of unreacted EDA. The sample was dried at 50 °C for 24 h in a vacuum oven. ^{1}H NMR (300 MHz, D_2O): $\delta = 4.90$ (m, 7H), 3.83–3.68 (m, 28H), 3.51–3.25 (m, 14H), 2.89 (d, 2H).

Finally, a 1 to 1 molar ratio of glycidyl methacrylate (GMA) (0.2g) and EDA-*β*-CD (2 g) was dissolved in 30 mL DMF, followed by the addition of a small amount of 1,4-dihydroxybenzene. The mixture was left to react for 6 h at 60 °C. After the reaction, the mixture was allowed to cool down to room temperature. Then, 100 mL of acetone was added. The resulting white precipitate was filtrated and washed using ca. 500 mL of acetone, and finally dried at room temperature for 24 h under vacuum.

Synthesis of thiol-terminated poly(4-methacryloyloxyazobenzene-*co*-2-(dimethylamino) ethyl methacrylate) and poly(glycidyl methacrylate-ethylenediamine-beta-cyclodextrin-*co*-2-dimethylamino) ethyl methacrylate) copolymer

CTA-PAzo-*co*-PDMAEMA and CTA-PCD-*co*-PDMAEMA were synthesized by RAFT polymerization. CPAD (14.4 mg, 0.052 mmol), AIBN (1.62 mg, 0.01 mmol), DMAEMA (1.77 mL, 0.312 mmol), 4-methacryloyloxyazobenzene (0.027 g, 0.1 mmol) or GMA-EDA-β-CD (0.12 g, 0.1 mmol) were mixed with 5 mL THF in a 25 mL Schlenk tube. After degassing with three freeze-pump-thaw cycles, the mixture was placed in a pre-heated oil bath at 70 °C for 24h under stirring. After the polymerization, the solution was cooled down to room temperature and the polymer was precipitated in diethyl ether (3X). Then 0.2 g of CTA-PAzo-*co*-PDMAEMA or CTA-PCD-*co*-PDMAEMA was dissolved in DMF, followed by the addition of n-butylamine (3 mL). The solution was stirred at room temperature for 12 h protected. The polymer was purified by precipitation in diethyl ether (3X) and dried at room temperature for 24 h.

Functionalization of gold nanoparticles with thiolated polymers

The concentration of the AuNPs was adjusted so the extinction of the plasmon peak of the suspension was 1 AU·cm^{-1}. Then 5 mL of AuNP suspension was concentrated by centrifugation and redispersed in 5 mL of a 0.1 mg/mL solution of thiolated polymer in THF while keeping the suspension in an ultrasound bath. The suspension was kept at room temperature overnight, and then centrifugation (5X) was used to remove the excess free polymer. The functionalized nanoparticles were kept in water with 0.1 mM CTAB.

Photocatalytic reactions

Catalytic reaction of 4-nitrophenol (4-NP): First, 25 µL of the 4-NP aqueous solution (either 10, 15, or 25 mM) were combined to 3 mL of a freshly prepared aqueous solution of $NaBH_4$ (8 mg·mL^{-1}). At this stage, the 4-NP was converted to nitrophenolate anion. Then, the appropriate volume (10, 30, 50 µL) of Au@CeO_2 suspension with 0.2 mg/mL of gold was added. The mixture was transferred into a quartz cuvette and irradiated with white light. UV–vis absorption spectrometry was used to monitor the conversion after predetermine reaction time.

Catalytic reaction of phenol red: First, an aqueous solution containing NH_4Br (20 mg·mL^{-1}), H_2O_2 (200 mg·mL^{-1}), and phenol red (0.25 mg·mL^{-1}) were prepared. Then, the appropriate volume of (150, 250, 350 μL) of Au@CeO_2 suspension with 0.2 mg/mL of gold was added to a 2.5 mL of this phenol red solution. The mixture was transferred into a quartz cuvette and irradiated with white light. UV–vis absorption spectrometry was used to monitor the conversion after predetermine reaction time.

Catalytic reaction of rhodamine B: An aqueous solution of rhodamine B (0.0015 mg·mL^{-1}) was prepared. Then 50; 100; 150 μL of the Au@CeO_2 suspension with 0.2 mg/mL of gold was added to a 2.5 mL of this rhodamine B solution. The mixture was transferred into a quartz cuvette and irradiated with white light. UV–vis absorption spectrometry was used to monitor the conversion after predetermine reaction time.

Electrospinning and PVA/AuNR@CeO_2 composite nanofibers

Suspensions of AuNR with different coverage of CeO_2 were prepared with a constant concentration of gold (60 mg/mL). Then, those concentrated AuNR suspensions (1 mL) were combined with a PVA solution (2 mL, 15 wt %) to yield a final suspension containing 10 wt % of PVA and 20 mg/mL of Au. The PVA/AuNRs suspensions were ultrasonicated for 10 min, and then stirred overnight at 200 rpm to obtain homogeneous suspensions. For electrospinning, a 1 mL syringe was filled with the PVA/AuNR mixture, and the electrospinning was conducted at room temperature with a relative humidity of 20–25%. The fibers were collected onto an aluminum foil carrier placed at a distance of 20 cm from the nozzle (diameter, 0.8 mm). The flow rate was 0.3 mL·h^{-1}, and the applied voltages was +18 kV. Fibers without any AuNRs were prepared under the same conditions. Samples for transmission electron microscopy (TEM) analysis were prepared by placing a TEM grid (copper, 300 mesh) on the aluminum foil to collect the fibers for 15 s. The fibers were crosslinked by placing the fiber mats in a reaction chamber with a vial containing 1 mL of a 50 wt % GA solution and 20 μL of a 37 wt % HCl solution. The pressure in the reaction chamber was reduced to 1 mbar, and the reaction was carried out at room temperature for 24 h. The reaction chamber was vented, and the mats recovered. Finally, any unreacted GA or HCl remaining in the mats were removed by drying the samples for 24 h at room temperature in the fume hood.

Self-assembly of gold nanorods

Typically, the self-assembly of the AuNRs was carried out by mixing, in a 4 mL glass vial, 0.5 mL of NRs suspension with an extinction of the LSPR of 1 $AU \cdot cm^{-1}$ of the two AuNRs suspensions functionalized with the complementary polymer ligands.

Self-assembly of PS and Si nanoparticles

The NPs were redispersed in THF with a concentration of 1 mg/mL. Then the suspensions were diluted to 0.1 mg/mL by the addition of the appropriate solvent mixture. Then, 0.5 mL of the two suspensions of complementary NPs were mixed in a 4 mL glass vial.

3.3 Characterization

Powder X-ray diffraction (XRD)

Solid-state analysis of the naked Au NPs and Au@CeO_2 NPs were conducted on a STOE Stadi P (Germany) diffractometer using Ag $K\alpha_1$ radiation. The sample was prepared on a perfluoropolyether film with Fomblin Y. The data were analyzed with the EVA software package from Bruker. All diffraction peaks were assigned to the cubic phase of CeO_2 (JCPDS #34-394) and the other one to the cubic phase of Au (JCPDS #89-3697).

UV-Vis absorption spectroscopy

Absorbance of solutions was collected for a spectral range of 300 ~ 1000 nm using Agilent Cary 60 UV/vis spectrometer.

Dynamic light scattering (DLS)

DLS measurements were carried out on an Zetasizer Nano S-90 system (Malvern), equipped with a He–Ne 633 nm laser as the light source and the analysis angle was 90º.

Nuclear magnetic resonance (NMR)

^1H NMR, T1 and T2 spectra were recorded with a Bruker AV-300 MHz NMR spectrometer. All the synthetic products could be dissolved in either $CDCl_3$, THF-d_8, D_2O, DMSO or cyclohexane-d_{12}.

Thermogravimetric Analysis (TGA)

The measurements were conducted using a Mettler-Toledo TGA/SDTA-851 thermobalance (50–700 °C, heating rate of 5 $°C \cdot min^{-1}$, nitrogen atmosphere; the initial sample weight was about 10 mg).

SEM and TEM imaging

The morphology of assemblies was imaged using SU8000 scanning electron microscope (Hitachi, Japan) and a JEM1400 transmission electron microscope (JEOL, Japan). TEM samples were prepared from casting a 5 μL of NPs suspension on a 300 mesh copper grid covered with carbon film, and dried quickly by removing the solvent at room temperature.

4. Results and discussion

This thesis aims to develop processes for the formation of supracolloidal assemblies with well-controlled hierarchical structures and use the supracolloidal assemblies as functional materials. Different approaches have been used in this thesis to build hierarchical supracolloidal structures: the colloidal electrospinning of tailored anisotropic Au-CeO_2 nanoparticles (**Section 4.1**), the self-assembly of anisotropic polymer-functionalized Au nanorods (**Section 4.2**), the directional self-assembly of isotropic polymer-functionalized PS, Si and Au nanoparticles (**Section 4.3**) and the interfacial self-assembly of polymer-functionalized Au nanotriangle (**Section 4.4**).

In **Section 4.1**, a library of anisotropic Au-CeO_2 nanoparticles with distinct shapes has been synthesized using gold nanosphere, gold nanorod, and gold nanotriangle templates for the selective over-growth of the cerium oxide domains. Finally, the most efficient heteronanostructures were successfully embedded in membranes by colloidal electrospinning. The resulting electrospun functional membranes were a convenient and scalable manner to use the nanoparticles in model water remediation experiments in a flow-through reactor.

In **Section 4.2**, Au nanorods were functionalized at their tips with polymers bearing either β-cyclodextrin or azobenzene moieties. The self-assembly of Au nanorods in plasmonic 1D arrays was easily controlled by the host-guest complexes formed by the polymer ligands. The resulting plasmonic supracolloidal assemblies can be broken and recombined by irradiation. Furthermore, the average number of Au nanorods in the self-assembled structures can also be controlled by the addition of free azobenzene to the system, demonstrating the ability of such supracolloidal assemblies to act as sensors.

In **Section 4.3**, PS, Si and Au nanoparticles were with complementary polymer ligands. Upon mixing the nanoparticles functionalized with the two complementary polymer ligands, the nanoparticles can undergo self-assembly. The self-assembly of those building blocks can be controlled by changing the solvent quality. Tuning the quality of the solvent was used to control the architecture of the resulting supracolloidal assemblies.

In **Section 4.4**, the site-selective functionalization of Au nanotriangles with polymer ligands was used to generate amphiphilic nanoparticles able to undergo self-assembly at the liquid-air interface. The monolayer formed adopted a close-packed structure, but the results obtained can be used to propose methods to potentially generate a wider variety of supracolloidal architectures.

4.1 Nanofibrous photocatalytic membranes based on tailored anisotropic Au-CeO_2 nanoparticles[1]

Supracolloidal assemblies can be readily formed by mixing nanoparticles with polymers, leading to the formation of hybrid materials displaying the properties of the nanoparticles but possessing the processing opportunities of the polymers. For example, the combination of plasmonic nanoparticles with semiconductor photocatalysts creates highly efficient photocatalytical nanoparticles. However, problematic recovery, and long-term colloidal stability of those nanoparticles in suspension limit their wide use in catalysis. In order to palliate to such limitation, the nanoparticles were embedded in polymer fibers to design photocatalytic membranes by colloidal electrospinning and used in water remediation experiments in a flow-through reactor.

4.1.1 Introduction

The use of light to drive and catalyze chemical reactions is a sustainable alternative to conventional heat-driven catalysis.[144-146] among the vast array of photocatalysts being developed, plasmonic-driven and plasmonic-enhanced photocatalysts are receiving growing interest because the hot charge carriers produced by the local surface plasmon resonance are typically more energetic than the electrons generated by traditional semiconductor and organic photocatalysts.[147] One of the main advantages of plasmonic photocatalysts nanoparticles (NP) is their unmatched ability to combine light absorption, electric field, energetic carriers, and thermal effect in one material.

However, the direct practical application of plasmonic photocatalysts NPs in suspensions remains restricted, being hampered by a lack of long-term colloidal stability and recyclability. To circumvent those limitations, the immobilization of the NPs in a solid matrix, like electrospun fibers, is appealing. To prepare photocatalytic electrospun membranes, we first optimize the plasmonic building blocks and then use colloidal electrospinning to embed them in nanofibers mats that could be used as a filtration membrane in a flow-through reactor.

An extensive range of plasmonic metal NPs (including Au, and Ag) have been used as photocatalysts,[148, 149] mostly because they can generate hot carriers during the optical excitation of their localized surface plasmon resonances.[150-152] The hot charge carriers can migrate to the surface of the NP where they can activate the chemical transformations of reactants located in close proximity to the surface. The efficiency of the ensuing chemical reactions is influenced by the interaction between the reactants and the NPs, and also by the efficiency of the transfer of the hot charge carriers.[151-154] Consequently, the size and shape of the NPs influence the catalytic activity. For example, small AuNPs have higher surface-to-volume ratios, which allows for the more efficient transfer of the hot carriers to the surface of the particle, and they, consequently, exhibit higher photocatalytic activity than larger AuNPs. Furthermore, the shapes of the particle influence the absorption of light, and thus the formation of hot charge carriers. Therefore, understanding the effect of the NPs size and shape on the catalytic activity would provide guidelines for designing photocatalytic materials.

The combination of plasmonic nanoparticles with semiconductors can largely improve their photocatalytic efficiency.[155] The functionalization of plasmonic NPs with semiconductor domains creates a new generation of highly efficient catalysts for visible-light-driven photocatalysis, and the resulting metal-semiconductor hybrid NPs are displaying potential for applications in a gamut of fields such as dye-sensitive solar cells (DSSCs), photocatalysis, photoelectric devices, or hydrogen production.[156-159] Different metal NPs (including Au, Pt, and Ag) have been combined with various semiconductors, such as TiO_2, ZnO, and CdS.[157, 160-162] The properties of metal-semiconductor NPs are highly dependent on the size, shape, and spatial distribution of each component.

Amongst the semiconductors used for catalysis, cerium oxide display a high oxygen storage capacity, a large number of oxygen vacancy defects between the oxidation states of cerium(III) and cerium(IV), and good thermal stability behavior,[163] which enhance reaction rates and make CeO_2 a prime candidate for the design of metal-semiconductor hybrid NPs.[164] The combination of CeO_2 with AuNPs is particularly appealing because CeO_2 has an appropriate Schottky barrier. The energy of the Schottky barrier of CeO_2 is similar to the energy of the hot-electrons generated by the plasmonic AuNPs, facilitating their injection in the CeO_2 domains,[107, 165-167] making the CeO_2-AuNPs hybrid nanomaterials ideal for plasmonic-enhanced photocatalysis.

Even though metal-semiconductor heteronanoparticles are very efficient photocatalysts, their direct applications remain difficult due to their challenging long-term colloidal stability, demanding separation from the reaction medium and overall problematic recovery and recycling. Embedding the NPs in a solid matrix is a convenient way to facilitate their straightforward applications. For example, porous solids, clays, and microbeads have been used amongst other substrates to immobilize the photocatalytic nanoparticles.[168-170] An alternative approach is the immobilization of the NPs in or on nanofibers prepared by colloidal electrospinning.[171, 172] Electrospinning is a scalable and versatile technique to obtain nanofibrous materials with variable porous structures and controllable fiber diameters.[173] Electrospinning of polymers and polymer hybrids has already been implemented in roll-to-roll processes and other industrial processes to form self-standing fibers and mats and coatings.[174, 175] During colloidal electrospinning, preformed nanoparticles can be combined to polymer solutions or melts to produce hybrid nanofibers.[176-178] Furthermore, immobilization of NPs within electrospun fibrous mats lead to the formation of catalytic membranes, which are more convenient for handling, processing, and avoiding contamination of the catalytic systems.[179] Recently, hybrid electrospun mats containing a variety of nanoparticles have found application in an array of fields such as wound dressing material and antifouling coatings.[128, 180]

Herein, we designed self-standing photocatalytic fibrous polymer mats containing AuNPs functionalized with CeO_2 domains. We used the over-growth of CeO_2 on specifically shaped AuNPs templates to prepare a library of tunable binary AuNP@CeO_2 catalysts. By turning the structure of the AuNP templates and the distribution of CeO_2 domains, we could control the photocatalytic activity of the resulting binary NPs. The AuNP@CeO_2 binary nanoparticles can promote both benchmark reduction and oxidation reaction of model waste products used in water remediation. This present approach combines the advantage of a metal nanoparticle and semiconductor patches, providing a platform for the design of novel hybrid metal-semiconductor anisotropic particles, which can be used as building blocks for the development of functional mesoscopic structures. To demonstrate this potential, we embedded the most efficient binary NPs in poly(vinyl acohol) (PVA) fibers and used the resulting nanofibrous mats to perform photocatalytic reactions in flow (**Figure 4.1.1**).

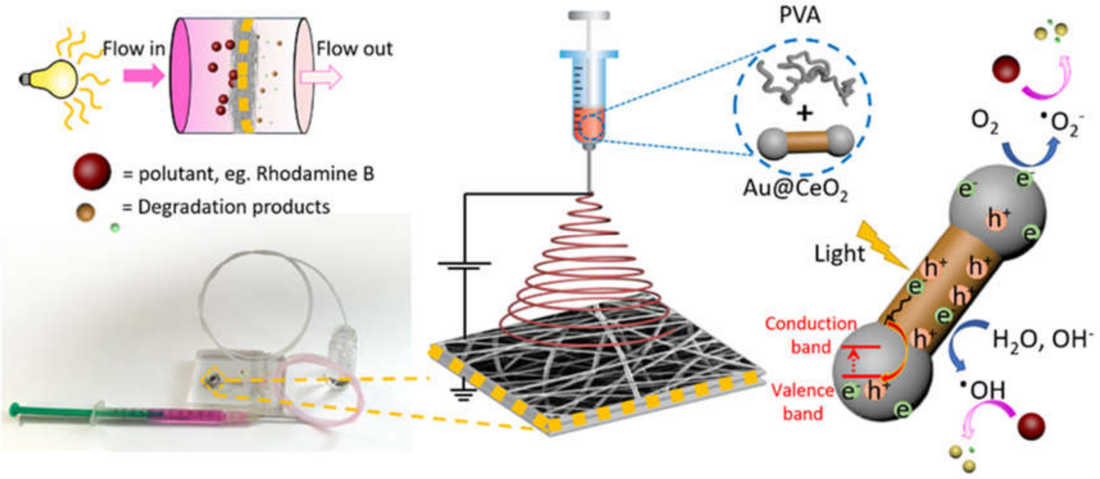

Figure 4.1.1 Preparation of photocatalytic membranes containing gold-cerium oxide nanoparticles and their use for the in-flow catalytic reaction.

4.1.2. Results and discussion

Gold nanoparticles (AuNPs), either gold nanospheres (AuNS), gold nanorods (AuNR), or gold nanotriangles (AuNT) were selectively functionalized with a complete or partial layer of cerium oxide (CeO_2) through an over-growth process to yield binary AuNP@CeO_2 (**Figure 4.1.2**).

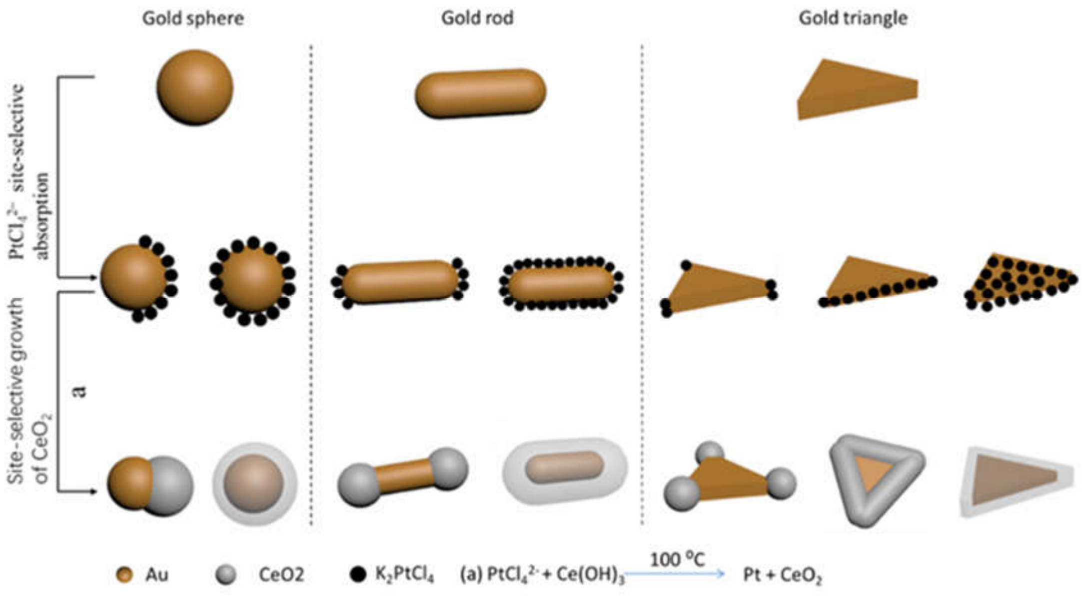

Figure 4.1.2. Library of the different Au@CeO_2 binary nanoparticles synthesized.

The site-overgrowth of CeO_2 on the anisotropic AuNPs occurs through the use of $PtCl_4^{2-}$ ions as the guiding units. The $PtCl_4^{2-}$ ions bind more strongly to high index facets.[167] and are the locus of the site-specific oxidation of the ceria precursor. When the system is fed with a limiting amount of K_2PtCl_4 those high index facets will be covered almost exclusively with the platinum ions. The ceria precursor, like cerium acetate ($Ce(AC)_3$), can be rapidly hydrolyzed into $Ce(OH)_3$ when the temperature is higher than 60 °C and subsequently be oxidized by the preadsorbed $PtCl_4^{2-}$ through an autoredox reaction to produce the CeO_2 nucleus where the $PtCl_4^{2-}$ ion are present. Further growth of those CeO_2 nucleus yields localized patches of CeO_2 when an excess of ceria precursor is heated above the temperature of 100 °C. Such an approach was used to generate patchy anisotropic binary AuNP@CeO_2 (**Figure 4.1.3**).

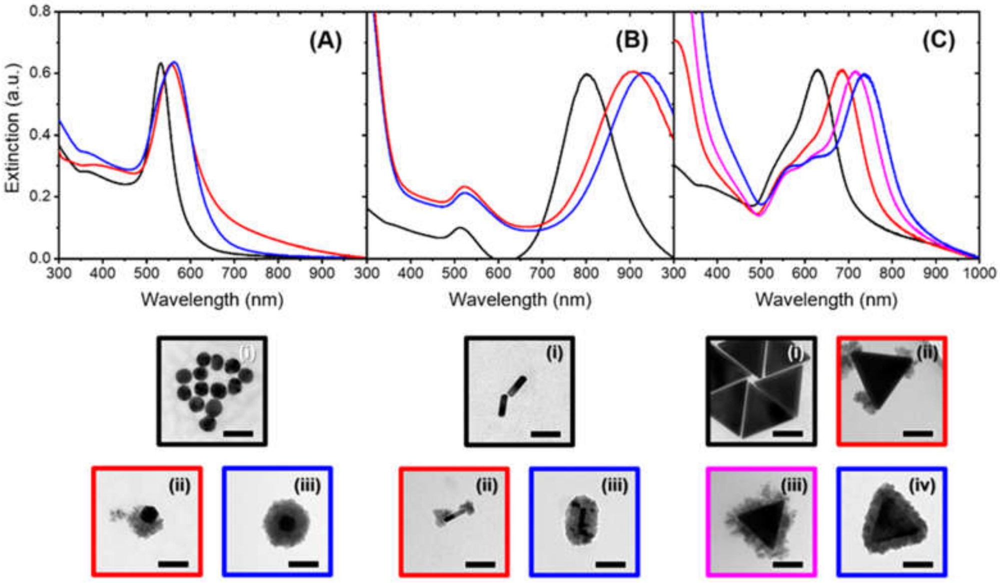

Figure 4.1.3 TEM images and UV–vis extinction spectra of AuNP-CeO_2 binary patchy nanoparticles. (A-C). TEM images of AuNS@CeO_2 nanoparticles, (E) UV–vis spectra of AuNS (black), AuNS@J-CeO_2 (red), AuNS@F-CeO2 (blue); (E-G). TEM images of AuNR@CeO_2 nanoparticle, (H) UV–vis spectra of AuNR (black), AuNR@F-CeO_2 (red), AuNR@T-CeO_2 (blue); (I-L). TEM images of AuNT@CeO_2 nanoparticle, (M) UV–vis spectra of AuNT (black), AuNT@T-CeO_2 (red), AuNT@E-CeO_2 (blue) and AuNT@F-CeO_2 nanoparticle (pink). The scale bars are 50 nm.

The amount of $PtCl_4^{2-}$ used played an essential role in the site-selective growth of CeO_2, given that the over-growth of CeO_2 only happens at the gold surface area where $PtCl_4^{2-}$ ions were adsorbed. Using AuNRs as the starting material, either fully covered NRs (AuNR@F-CeO_2) were produced when an excess of K_2PtCl_4 was used, or tip-coved NRs (AuNR@T-CeO_2) were produced in the presence of a limiting amount of K_2PtCl_4. Similarly, fully covered AuNTs (AuNR@F-CeO_2), edge-covered AuNTs (AuNT@E-CeO_2), or tip-cover AuNTs (AuNR@T-CeO_2) can be produced by limiting the amount of K_2PtCl_4 in the presence of AuNTs. When AuNSs were used as the substrate, a limiting concentration of K_2PtCl_4 during the reaction yielded Janus NPs (AuNS@J-CeO_2) while an excess of K_2PtCl_4 yielded fully-covered nanostructures (AuNS@F-CeO_2).

The modification of the AuNPs with CeO_2 over-growth led to a red-shift in the intrinsic localized surface plasmon resonance (LSPR) extinction. The addition of CeO_2 onto the naked AuNP resulted in a stronger red-shift of the LSPR maxima, which was more pronounced for the fully covered AuNPs@CeO_2 than the partially covered AuNPs@CeO_2. This shift was due to an increase in the local refractive index of the immediate surrounding of the AuNPs, and the increase of the local refractive index was more significant as the amount of CeO_2 on the AuNP increased. Since the refractive index of the environment around the AuNPs increased as more of the surface area was covered by the CeO_2.[181]

The X-ray diffraction (XRD) pattern of the binary nanostructures CeO_2@AuNS (**Figure 4.1.4A**) showed two sets of diffraction peaks, one stemming from the AuNSs and one ascribed to the CeO_2 over-growth. Similar results were also obtained for the CeO_2@modified AuNR and AuNT (**Figure 4.1.4 B and C**). One set of diffraction peaks was assigned to the cubic phase of CeO_2 (JCPDS #34-394) and the other one to the cubic phase of Au (JCPDS #89-3697).

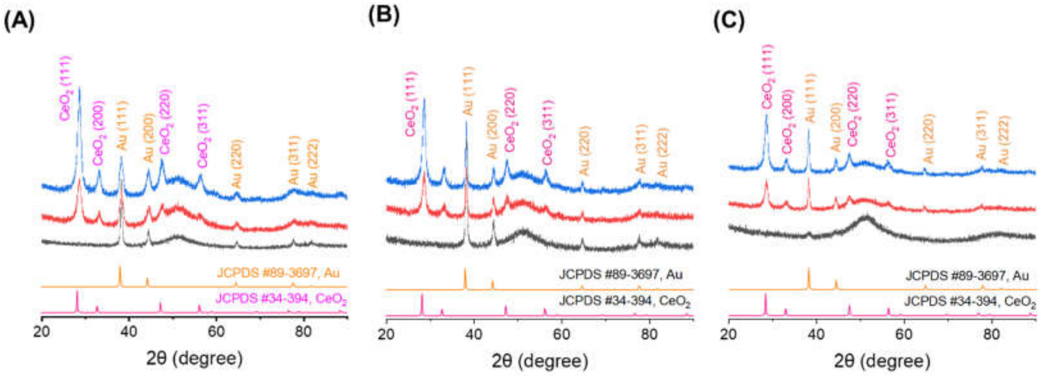

Figure 4.1.4. XRD patterns of naked AuNP (black), AuNP@J-CeO_2 (red), AuNP@F-CeO_2 (blue) nanoparticles, and the reference diffraction patterns for Au (JCPDS #89-3697) (orange) and CeO_2 (JCPDS #34-394) (pink). For the binary nanoparticles obtained with (A) AuNS, (B) AuNR and (C) AuNT templates.

The excitation of the LSPR of AuNPs generates "hot electrons" that possess high kinetic energy after being accelerated by the strong electric field of the plasmon. Those hot electrons can be harnessed to catalyze an array of organic reactions involving species either in close vicinity or adsorbed to the gold surface.[182, 183] The catalytic activity of the AuNP@CeO_2 binary nanostructures was investigated using three different benchmark reactions: the reduction reaction of 4-nitrophenol to 4-aminophenol in the presence of sodium borohydride; the oxidation reaction of phenol red to bromophenol blue in the presence of hydrogen peroxide and halogen ions and the photodegradation of rhodamine B.[184-186] Those reactions are model reactions used in the development of photocatalytic water remediation strategies.[187, 188]

Rhodamine B can be degraded under light irradiation in the presence of photocatalysts like AuNPs or AuNP@CeO_2. During the rhodamine B degradation, the absorption peak at ca. 554 nm decreased and the color of the solution changed from red to colorless (**Figure 4.1.5**). This reaction was used as a benchmark to compare the library of AuNP@CeO_2 binary nanostructures prepared (**Figure 4.1.5**), by monitoring the concentration of rhodamine B in solution by UV-Vis spectrometry.

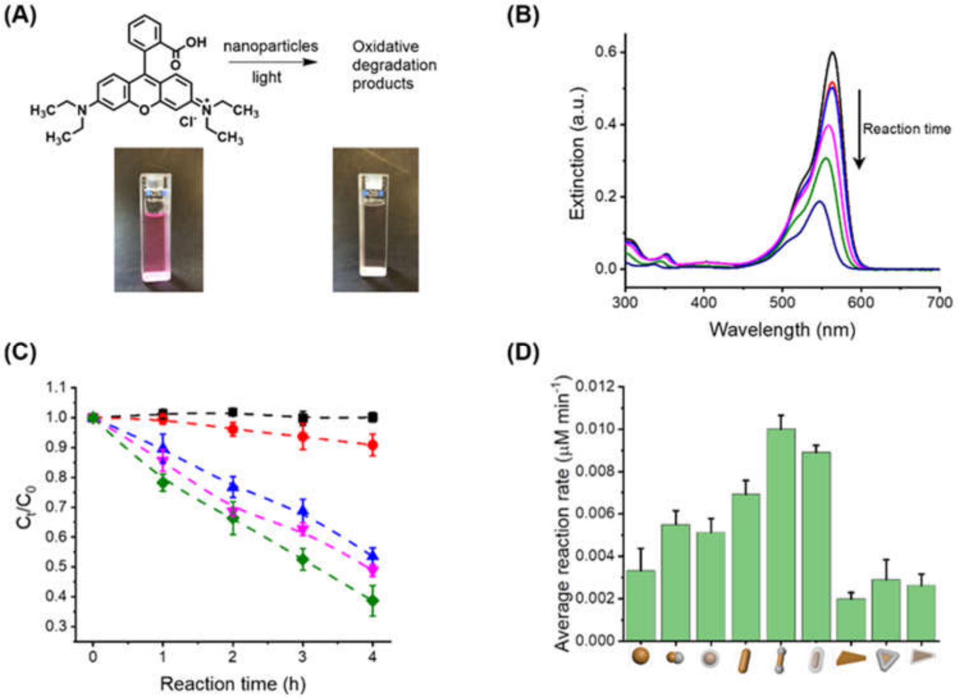

Figure 4.1.5. Catalytic activity of the nanoparticles in suspension during the photooxidation of rhodamine B. (A) Degradation of rhodamine B. (B) UV–vis spectra of the catalytic degradation of rhodamine B. (C) Variation of the concentration of rhodamine B during the reaction in the presence of AuNRs or AuNR@CeO_2 under different conditions; under light irradiation, without nanoparticles (black), with nanoparticles (AuNRs), without irradiation (red), with AuNRs, under irradiation (blue), with AuNRs@T-CeO_2, under irradiation (green), and with AuNRs@F-CeO_2, under irradiation (pink). (D) Reaction rate of the photodegradation of rhodamine B in the presence of the different AuNP@CeO_2 prepared.

Similarly, the oxidation of phenol red to bromophenol blue in the presence of Br^- and H_2O_2 can be catalyzed with light after the addition of the right NPs. During this reaction, the color of the solution turned from light yellow (phenol red) to blue (bromophenol blue), and consequently, the absorption peak at ca. 400 nm belonging to phenol red decreased, while the peak belonging to bromophenol blue at ca. 590 nm increased. The reaction kinetics could be monitored from time-dependent UV-Vis spectrometry (**Figure 4.1.6**). Likewise, the reduction of 4-nitrophenol (4-NP) to 4-aminophenol (4-AP) in the presence of $NaBH_4$ was accompanied by a decrease in intensity of the peak at ca. 400 nm in the UV-Vis spectra of 4-NP while the 4-AP peak at ca. 300 nm increased and can be used to quantify the extent of the reaction (**Figure 4.1.7**).

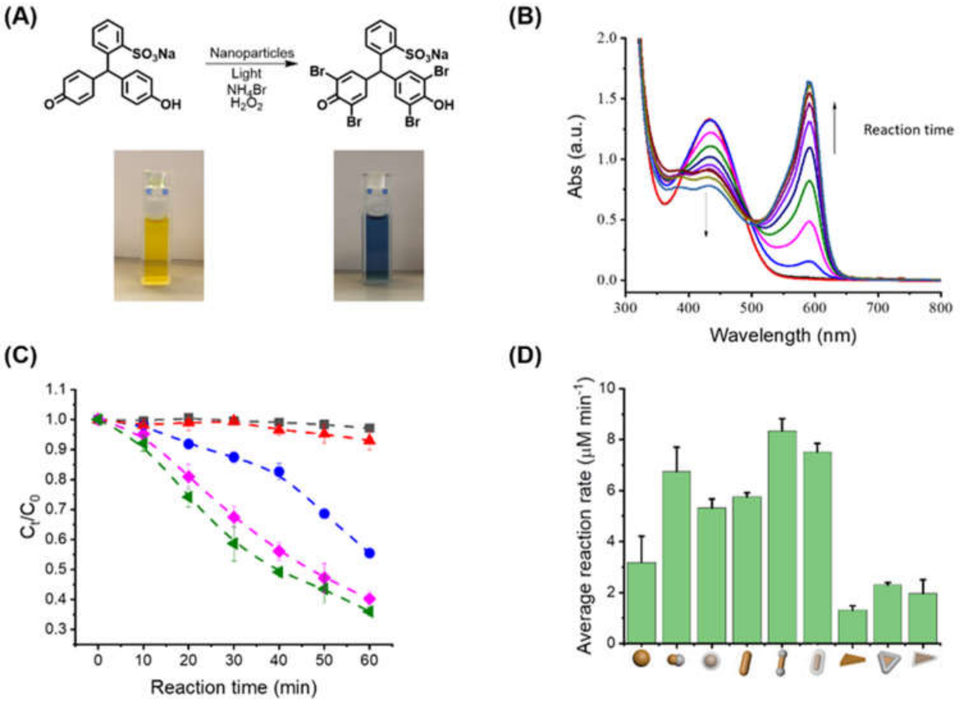

Figure 4.1.6. Catalytic activity of the nanoparticles in suspension during the photooxidation of phenol red. (A) Conversion of phenol red to bromophenol blue. (B) UV–vis spectra of the catalytic conversion of phenol red to bromophenol blue. (C) Variation of the concentration of phenol red during the reaction in the presence of AuNRs or AuNR@CeO_2 under different conditions; under light irradiation, without nanoparticles (black), with nanoparticles (AuNRs), without irradiation (red), with AuNRs, under irradiation (blue), with AuNRs@T-CeO_2, under irradiation (green), and with AuNRs@F-CeO_2, under irradiation (pink). (D) Reaction rate of the photodegradation of nitrophenol in the presence of the different AuNP@CeO_2 prepared.

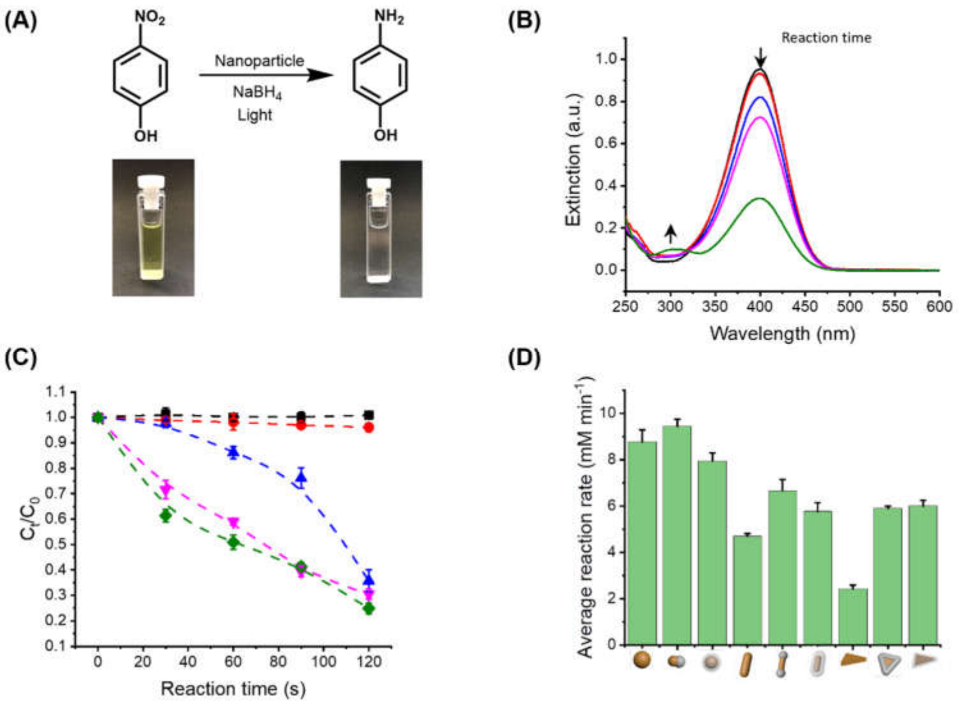

Figure 4.1.7. Catalytic activity of the nanoparticles in suspension during the photoreduction of 4-nitrophenol. (A) Conversion of 4-nitrophenol to 4-aminophenol. (B) UV–vis spectra of the catalytic degradation of 4-nitrophenol. (C) Variation of the concentration of nitrophenol during the reaction in the presence of AuNRs or AuNR@CeO_2 under different conditions; under light irradiation, without nanoparticles (black), with nanoparticles (AuNRs), without irradiation (red), with AuNRs, under irradiation (blue), with AuNRs@T-CeO_2, under irradiation (green), and with AuNRs@F-CeO_2, under irradiation (pink). (D) Reaction rate of the photodegradation of nitrophenol in the presence of the different AuNP@CeO_2 prepared.

To compare the reaction rate observed in the presence of the different binary nanoparticles, all the reactions were performed at a constant concentration of Au at 0.2 mg/mL. The coverage of the AuNPs with CeO_2 influenced the rate of the photocatalytic reactions (**Figure 4.1.8**). In the presence of the NPs but in the absence of light, the reagents (either rhodamine B, phenol red or 4-NP) were not consumed; similar results were also observed for reagents solution irradiated in the absence of NPs. However, when the AuNP@CeO_2 binary nanostructures were present in suspensions and irradiated with white light, the reagents were consumed as measured by UV-Vis spectrometry (**Figure 4.1.5, and 4.1.8**).

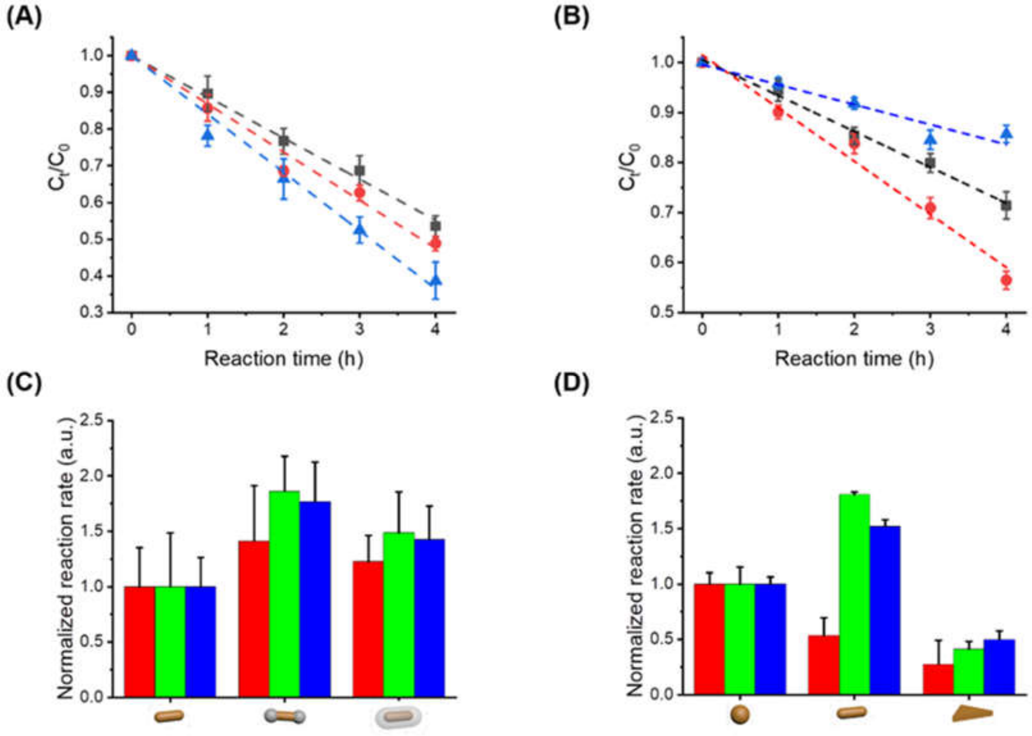

Figure 4.1.8. (A) Variation of the concentration of rhodamine B during photodegradation catalyzed with AuNR (black), AuNR@F-CeO$_2$ (red) and AuNR@T-CeO$_2$ (blue). (B) Variation of the concentration of rhodamine B during photodegradation catalyzed with naked AuNS (black), AuNR (red) and AuNT (blue). (C) Normalized reaction rate for the catalytical reaction of nitrophenol (red), phenol red (green) and rhodamine B (blue) in presence of AuNR@CeO$_2$ with different CeO$_2$ coverage. (D) Normalized reaction rate for the catalytical reaction of nitrohenol reaction (red), phenol red (green) and rhodamine B (blue) in presence of naked gold nanoparticles of different shape.

The photocatalytic activity of the AuNP@CeO$_2$ resulted from the plasmon-excitation-induced hot-electrons, and for the three reactions studied and the three types of binary architectures used (naked, fully covered, or partially covered), the photocatalytic activity of the AuNPs increased with the addition of CeO$_2$. However, the addition of a complete layer of CeO_2 either did not improve the performance of the photocatalyst in comparison to the partially covered AuNPs, either the same catalytic activity or a decrease in catalytic activity was observed for the fully covered AuNPs. The catalytic activity of partially covered AuNP@CeO_2 was higher than that of fully covered AuNP@CeO_2, which was higher than the naked AuNPs. The results suggest that the access of the reacting molecules to the gold substrate is essential and that the full coverage of the AuNPs with a layer of porous CeO_2 impeded the diffusion of the reactive species to reaction sites.

Under light irradiation, the AuNPs used as the template for the binary AuNP@CeO_2 produced a pair of hot-electron and hot-hole and those hot-charge carriers can move to the gold surface where they reacted with any molecules present there. In the case of AuNP@CeO_2 binary photocatalysts, the Au part was responsible for light absorption generating hot-charge carriers. Due to the complementary energy level of the hot-electrons of Au and the Schottky barrier of CeO_2, the hot-electrons were able to flow from Au to the conduction band (CB) of CeO_2 (**Figure 4.1.1**), separating the electron-hole pair increasing the catalytic activity of the heteronanostructures.[166] The electrons transferred to the CeO_2 domains were available to perform photoreaction, and the CeO_2 domains behaved as an electron-transfer medium.

The different AuNP templates used also affected the catalytic activity observed (**Figure 4.1.8B**). The photooxidation of rhodamine B and phenol red was faster in the presence of AuNRs than in the presence of AuNSs, which was faster than in the presence of AuNTs. However, the photoreduction of 4-NP was the fastest in the presence of the AuNSs. The photocatalytic activity observed resulted from different factors, mainly the absorption of light resulting in the formation of hot-electrons and the interaction between the reagents and the surface of the NPs. To qualitatively addressed the formation of hot-electrons by the light absorption, a constant concentration of AuNPs (2 mL of a suspension of 0.2 mg·mL^{-1} of gold) was immobilized on 0.5 cm^2 of a poly(ethylene terephthalate) film coved with indium tin oxide. The resulting electrodes were used in a 3-electrode system to measure the photocurrent generated by their exposure to the white light used in the catalytic experiments (**Figure 4.1.9**). The result shows that the current density generated by the AuNRs was larger than the current density produced by the AuNSs and AuNTs (**Figure 4.1.9A**). However, the presence of the CeO_2 domains only had a marginal effect of the photocurrent measured during the irradiation of the 3-electrode system (**Figure 4.1.9B**). Furthermore, the photooxidation reaction rate of rhodamine B was directly related to the photocurrent generated (**Figure 4.1.9B**).

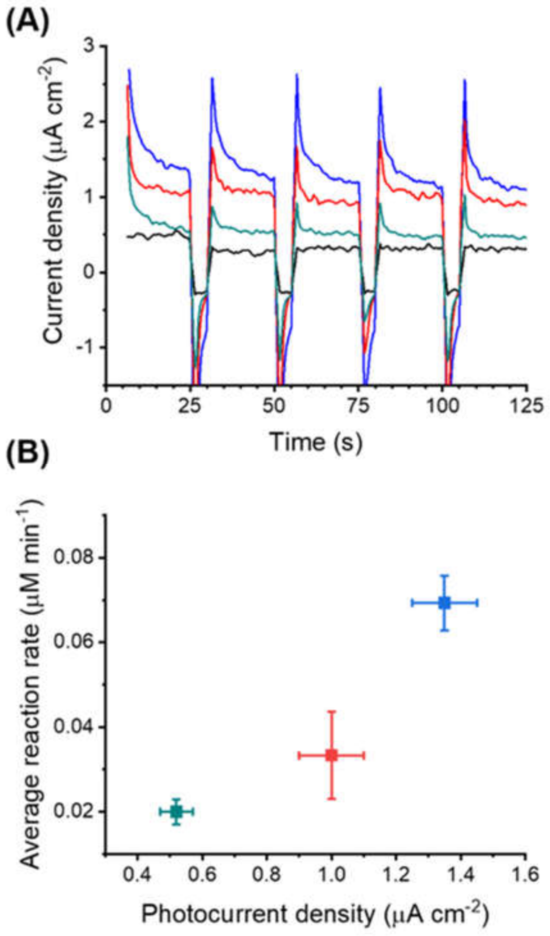

Figure 4.1.9. (A) Photocurrent measured with AuNSs (red), AuNRs (blue) and AuNTs (green). (B) Photooxidation reaction rate of rhodamine B for nanoparticle producing different photocurrent.

However, the behavior observed for the conversion of 4-NP to 4-AP could not only be attributed to the efficiency of hot-electron formation. The mechanism of the reactions, the reactivity of the different crystalline facets of gold and the AuNPs composition also need to be taken into account. In the case of AuNSs, the particles present mostly (111) and (100) facet,[189] while the AuNTs are mostly composed of (111) planes,[190] whereas in the AuNRs the long cylindrical wall is built with (110) planes and the spherical caps with (111) and (100) facets.[189] The first step in the photooxidation reaction of phenol red and rhodamine B is the production superoxide, like $O_2^{\bullet -}$, from dissolved oxygen, and the formation of superoxide occurs preferentially at (110) facet.[191] In the case of the reduction of 4-NP, the first step of the reaction is the concomitant binding of the 4-NP and of the borohydride ion to the surface of the gold,[192] which is favored on (100).[193, 194] Consequently, the AuNS, exposing a larger fraction of (100) facets, catalyzed the reduction of 4-NP more efficiently than the AuNTs and AuNRs.

All the AuNP@CeO_2 photocatalyst prepared were highly efficient to catalyze the model reactions. However, their isolation from the reaction system was challenging. To prepare more convenient photocatalytic functional materials, the AuNR@CeO_2 building blocks were immobilized in membranes made of poly(vinyl alcohol) (PVA) nanofibers (**Figure 4.1.10**). The catalytic membranes were prepared based on the study of AuNP@CeO_2 for the catalytic activity. AuNR and AuNR@CeO_2 were used as the model catalysts to prepare the catalytic membranes. The fibers were prepared by the colloidal electrospinning of a mixture of AuNR@CeO_2 in suspension in a concentrated aqueous solution of PVA. All the hybrid nanofibrous membranes were prepared with the same loading of gold atoms (0.2 mg of Au/mg of PVA). The nanofibers were crosslinked to prevent the dissolution of the membrane after immersion in water and efficiently entrap the NPs in the fibers (**Figure 4.1.11**).

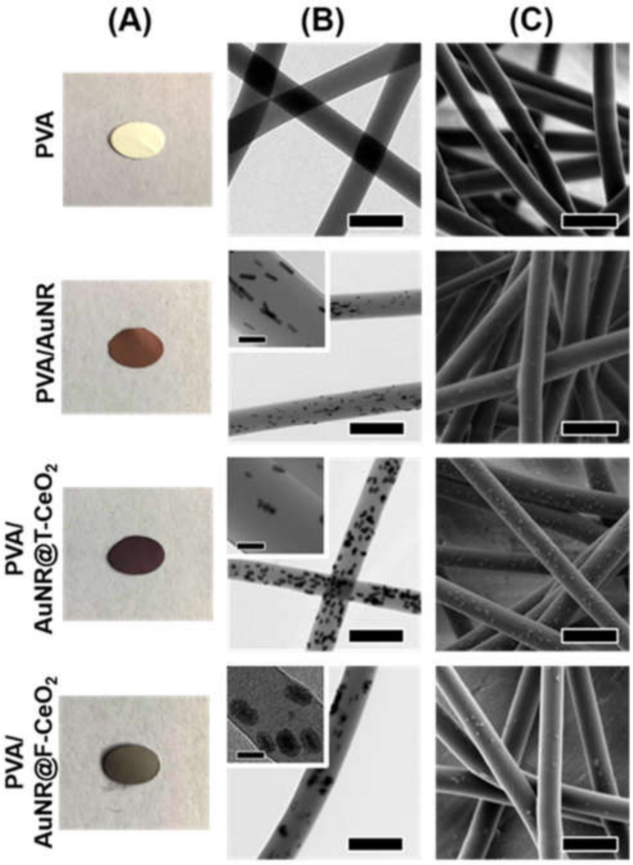

Figure 4.1.10. Electrospun hybrid membranes (A) images of the membrane coupons, (B) TEM images of the fibers (scale bars 250 nm, and 50 nm in the insets) and (C) SEM images of the fibers (scale bars 250 nm) made with PVA or mixtures of PVA/AuNR, PVA/T-AuNR@CeO$_2$ and PVA/F-AuNR@CeO$_2$.

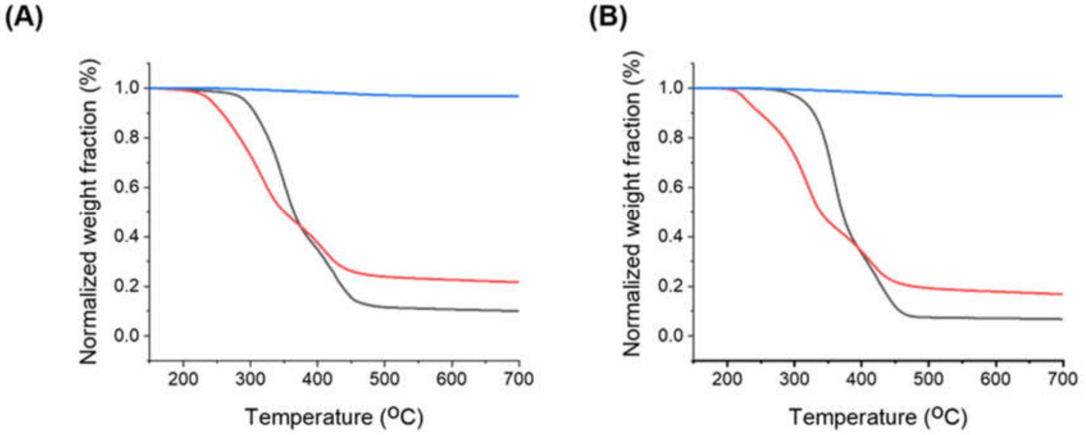

Figure 4.1.11. Thermogravimetric analysis of pure PVA membrane (black), PVA/AuNR membrane (red) and pure AuNR (blue) before (A) and after (B) immersion in water for 2 weeks.

The AuNR@CeO_2 NPs were distributed throughout the PVA fibers (**Figure 4.1.10**). The NPs with more extensive coverage of CeO_2 displayed some mild aggregation in the fibers, which was absent in the parent suspension used for electrospinning. Additionally, the NRs were oriented along the fiber axis direction. The alignment of NRs in PVA nanofibers can be attributed to the strong shear forces generated on the NR/PVA suspension during the electrospinning process. The suspension was sheared by the flow driven by the difference of potential applied, and then, the NRs were oriented along the direction of elongated polymer flow.[98, 195]

The choice of a crosslinked PVA network as a matrix for the embedding of AuNR@CeO_2 was made to allow access to the catalytic sites of the AuNPs for the molecules dissolved in water. Pure PVA fibers swelled after immersion in water, and water-soluble reactants can penetrate the PVA fibers and react with the embedded NRs. Given the permanent immobilization of the AuNP@CeO_2 and the access to the photocatalytic sites, PVA/AuNR or AuNR@CeO_2 nanofibrous membranes are promising hybrid materials for long-term use in aqueous environments.

The activity of the photocatalytic membranes was studied for their efficiency in the photodegradation of rhodamine B. Poly(dimethyl siloxane) (PDMS) devices were prepared by layering the photocatalytic membranes in a fluidic device (**Figure 4.1.12**).

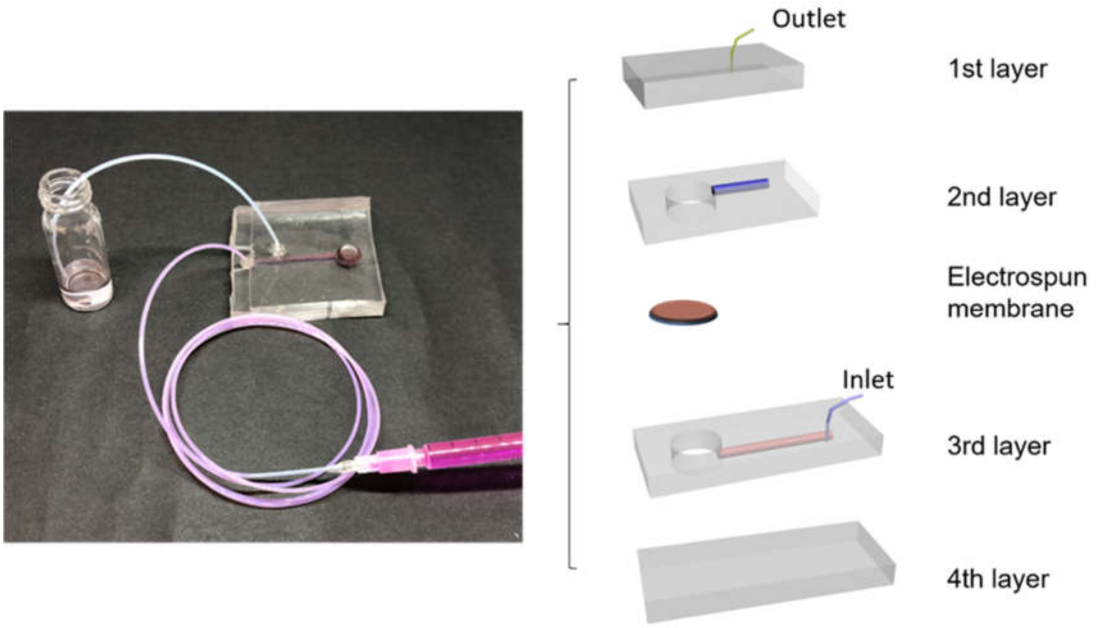

Figure 4.1.12. Architecture of the flow-through device.

The resulting PDMS devices were used to study the conversion of the rhodamine B at different flow rates (**Figure 4.1.13**). The degradation of rhodamine B can be switched on and off by shining white light on the devices (**Figure 4.1.13A**). In comparison to free AuNR@CeO$_2$ (**Figure 4.1.5**), the AuNR@CeO$_2$ embedded in the PVA membrane showed the same trend of efficiency. At a given flow rate, the membranes embedding AuNR@T-CeO$_2$ displayed a higher photodegradation than the membranes containing AuNR@F-CeO$_2$, which were more efficient than the membranes containing the naked AuNRs. Using a flow-through device, the rhodamine conversion was no longer controlled by the reaction time but rather by the flux of rhodamine B solution through the membrane. When the flux was too fast, the residence time of the molecules in the photocatalytic area was not long enough to allow for a complete conversion of the rhodamine B. However, the activity of the membranes can also be influenced by the loading of NPs in the fibers. As the concentration of nanoparticles in the fiber increased, the rhodamine conversion observed at a given flow rate increased

(**Figure 4.1.13D**). Furthermore, the reaction can be performed over a long period of time with a limited influence of the conversion observed at a given flow rate (**Figure 4.1.13B**).

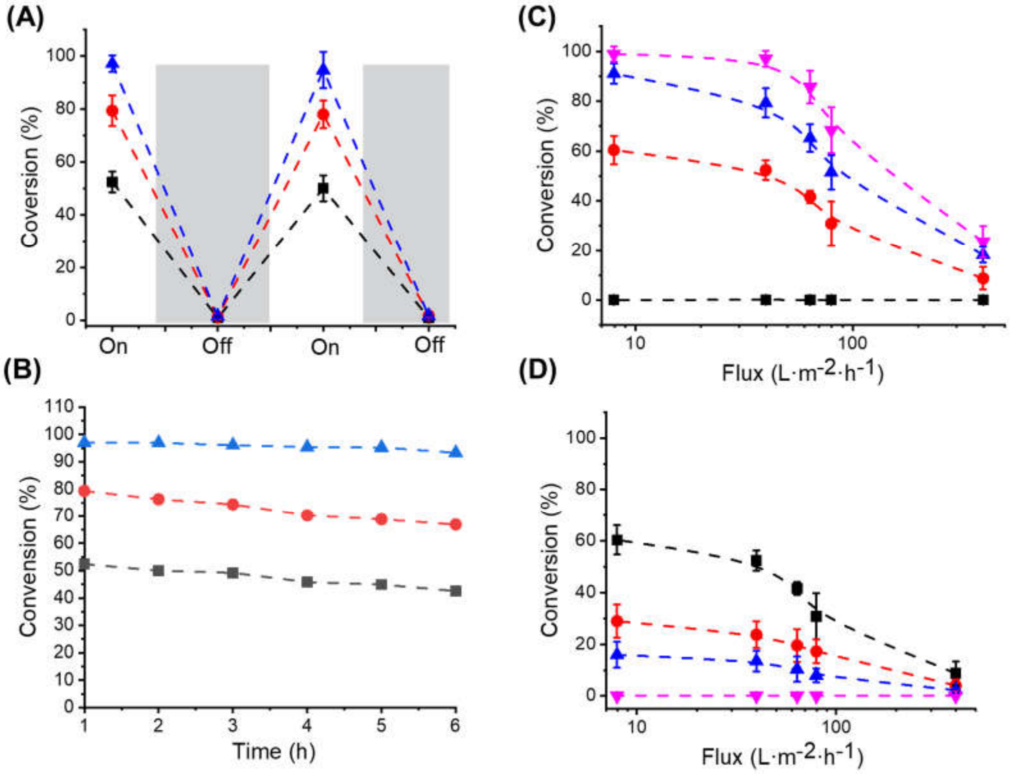

Figure 4.1.13. (A) Variation of the efficiency of the catalytic membranes for the degradation of rhodamine B using membranes prepared with AuNP@CeO_2 with different structures (AuNRs (black), AuNR@F-CeO_2 (red) and AuNR@T-CeO_2 (blue)) under different irradiation conditions. (B) Variation of the efficiency during continuous operation for membranes prepared with AuNRs (black), AuNR@F-CeO_2 (red) and AuNR@T-CeO_2 (blue). (C) Degradation of rhodamine B using membranes prepared with AuNP@CeO_2 with different structures (no Au (black), AuNRs (red), AuNR@F-CeO_2 (blue) and AuNR@T-CeO_2 (pink)), all the membranes were prepared with 0.02 wt% of Au atoms; (D) Degradation of rhodamine B using membranes with variable loading of AuNRs (0 mg of Au/mg of PVA (black), 0.05 mg of Au/mg of PVA (orange), 0.1 mg of Au/mg of PVA (green), and 0.2 mg of Au/mg of PVA (red).

4.1.3. Conclusion

In summary, we prepared efficient photocatalytic membranes containing binary heteronanostructures made of gold and cerium oxide. Using the selective over-growth of crystalline cerium oxide on gold nanotemplates, we formulated a library of photocatalytic nanoparticles. Gold nanosphere, gold nanorod, and gold nanotriangle were used as templates for the growth of the cerium oxide domains, and the resulting heteronanoparticles catalyzed both reduction and oxidation photoreactions. The gold nanoparticles covered with patches of cerium oxide outperformed the fully covered and the naked nanoparticles in terms of catalytic efficiency for every reaction tested. Conversely, the catalytic activity observed with the different gold templates was influenced by the reaction studied due to the different mechanisms involving the adsorption of specific chemical species on specific crystallographic facets. Finally, the most efficient heteronanostructures were successfully embedded in membranes by colloidal electrospinning. The resulting functional membranes were a convenient and scalable manner to use the nanoparticles in model water remediation experiments.

4.2 Controlled and reversible directional self-assembly of gold nanorods[1]

In the previous section, the selective over-growth of crystalline cerium oxide was performed on gold nanoparticles template with distinct shapes. Just like cerium oxide can be specifically grown on specific facets of the gold nanoparticles, the gold nanorods can also be specifically functionalized with polymer patches through the preferential interaction of thiols for high index facets of gold nanostructures.

In this section, the linear assembly of polymer-functionalized nanorods was used to prepared 1D supracolloidal plasmonic structures from the self-assembly of patchy nanoparticles in suspensions. The polymer ligands were designed to interact with reversible host-guest interactions. The effect of the host-guest interaction between the polymer patches has been studied. Moreover, the average number of nanorods in the supracolloidal assemblies can be controlled by changing the condition such as light and the presence of specific molecules in the environment.

4.2.1 Introduction

The organization of individual nanoparticles (NPs) into well-designed structures has attracted much attention during the past decades. This is because of the unique properties obtained by the collective properties of the assemblies, which can be further used for many applications like sensors or electro-optical devices.[196-198] This is especially the case for metal nanoparticles such as Au, and Ag, which have a localized

---

surface plasmon resonances (LSPR). When plasmonic NPs assemble with close interparticle distances, the LSPR of individual nanoparticles can become coupled, resulting in the generation of hybridized plasmons that can generate hotspots with an enhanced optical electric field at the nanoparticle junctions.[199] Such hotspots have been effectively used to enhance spectroscopic signals in many techniques like surface-enhanced Raman scattering (SERS).[200, 201] Consequently, finding a way to control the final structure of nanoparticle assemblies with a controlled distance between nanoparticles and a controlled number of hotspots will potentially generate an array of new functional materials.

Linear chains of metal nanoparticles, also called plasmonic polymers,[202] can be formed, with controlled interparticle distances, on planar substrates by electron-beam lithography or focused ion-beam milling.[202, 203] However, those methods are cost and time prohibitive. The self-assembly of metal nanoparticles would offer a simple, cost-efficient, solution-based method for producing similar plasmonic structures. [204, 205] Imparting directionality to the building blocks used during the self-assembly process is the key to create such mesostructured materials. In doing so, the directional physical bonding between NPs functionalized with complementary or self-complementary ligands is an appealing strategy.[114, 206] The formation of plasmonic polymers has been controlled, for example, through hydrogen bonding, hydrophobic forces, and change the condition such as temperature.[207-210]

Dynamic reversible host-guest chemistry can be viewed as a versatile and powerful means for designing materials with complex structures.[210, 211] The formation of such supramolecular complexes can be controlled by external stimuli, including pH, temperature, or light irradiation.[212-214] This offers an interesting opportunity to design next-generation stimuli-responsive assemblies of NPs. While the assembly of gold NPs has been successfully performed using complementary interacting polymer patches and supramolecular chemistry has also been used,[215] complementary polymer patches undergoing supramolecular interactions have not. The use of complementary polymers forming a host-guest pair in the directional self-assembly of such nanostructures would provide a way to precisely control the distance between nanoparticles in a reversible manner.

Here, we demonstrate that host-guest chemistry can be used to control the self-assembly of gold nanorod to form plasmonic polymers. The plasmonic polymers can be broken and recombined by changing the condition. The building blocks were gold nanorods (NRs) end-terminated with polymer bearing cyclodextrin (β-CD) or azobenzene (Azo) moieties. The NR assembly was triggered by mixing the two different functionalized gold NRs suspensions resulting in the formation of a host-guest couple between the β-CD and the Azo. The resulting plasmonic polymer can be broken and recombined by irradiation. Furthermore, given that the comonomer used in the polymer synthesis was thermo- and pH-responsive, the interparticle distance could potentially be further tuned by changes in temperature or pH (**Figure 4.2.1**).

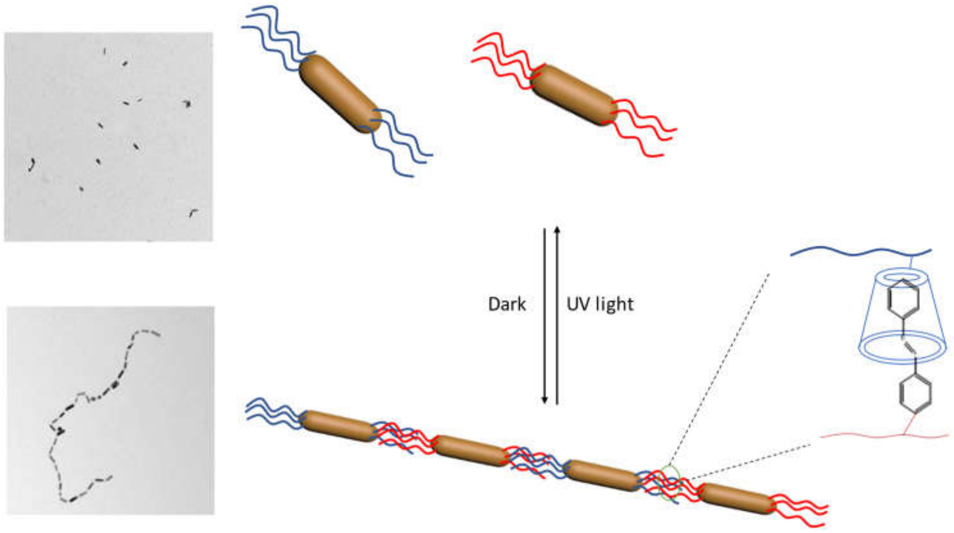

Figure 4.2.1: Schematic of the reversible self-assembly of complementary polymer-functionalized gold nanorod by host-guest chemistry.

4.2.2 Results and discussion

The gold nanorods synthesized (Experimental Section 3.2) were 35 ± 5 nm × 8 ± 2 nm in size as measured by transmission electron microscopy (TEM). The nanorods were also characterized by UV-vis spectroscopy and the LSPR of these nanoparticles was at ca. 780 nm in water.

For the polymer synthesis, the monomer 2-(dimethylamino)ethyl methacrylate (DMAEMA) was chosen because PDMAEMA is pH and temperature-sensitive. The β-CD/Azo couple was selected because it can undergo host-guest interaction. The polymer ligands poly(DMAEMA-*co*-β-CD) and poly(DMAEMA-*co*-Azo) were synthesized by reversible addition-fragmentation chain transfer polymerization (RAFT). Following the polymerization, the thiol-terminated polymer ligand was obtained by the aminolysis of the chain transfer agent used for the RAFT polymerization to produce a thiol group able to bind to the gold surface.

Before performing the ligands exchange of thiol-terminated polymers on the gold nanorods, it is crucial to study the availability of the –SH groups. The freshly prepared –SH group from the cleaved polymer can react with 5,5'-dithiobis-(2-nitrobenzoic acid) (DTNB) and produce 2-nitro-5-thiobenzoic acid (TNB), which has an absorption at 412 nm, and one mole of –SH group produces one mole of TNB. **Figure 4.2.2A** shows the UV-Vis spectra and the standard curve of TNB. The absorption of the cleaved polymers mixed with DTNB showed the quantitative formation of thiol groups, and every polymer chain was bearing one reactive –SH group.

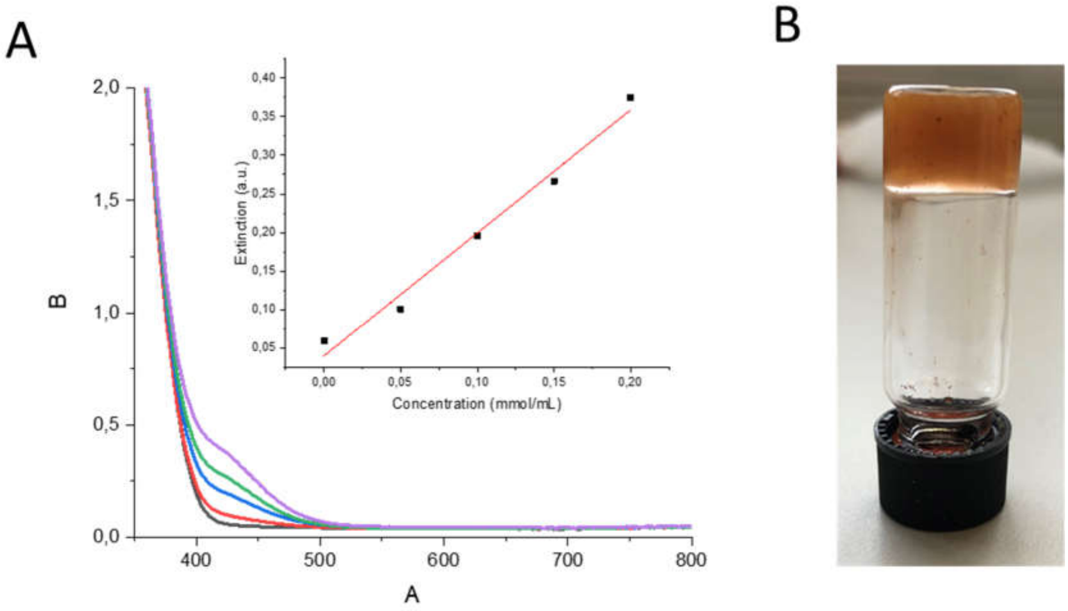

Figure 4.2.2 (A) the UV-Vis spectra and the standard curve of TNB, (B) the image of the polymer gel by mixing the polymers bearing β-CD and Azo moieties.

The two complementary polymers contained respectively 30 mol% of either β-CD or Azo monomers. Upon mixing those two polymers, the formation of host-guest interaction resulted in the formation of a gel (**Figure 4.2.2B**). This interaction can be harnessed to control the directional self-assembly of AuNRs in suspension.

The UV-Vis spectra of AuNRs functionalized with SH-poly(DMAEMA-*co*-cyclodextrin) and SH-poly(DMAEMA-*co*-azobenzene) (**Figure 4.2.3**) show that after polymer functionalization, the gold rods were still well-dispersed in suspension. Aggregation would have resulted in a shift in the position of both the transverse and longitudinal plasmon peaks. For both polymers functionalized AuNRs, the peak at ca. 530 nm did not shift, and the peak at ca. 780 nm was shifted by ca 10 nm for both polymers. This shift was caused by the presence of the polymer on the AuNRs. The presence of the polymer marginally changed the refractive index of the media at the surface of the AuNRs, which resulted in a moderate shift of the plasmon peak position.

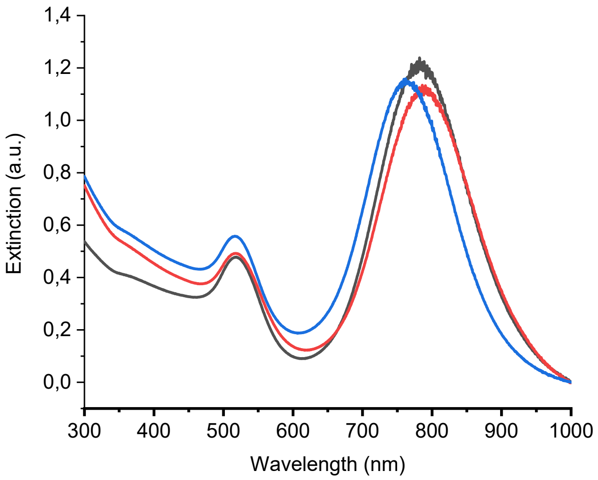

Figure 4.2.3 UV-Vis spectra of gold rods (black), and gold rods functionalized with SH-poly(DMAEMA-*co*-cyclodextrin) (red) and SH-poly(DMAEMA-*co*-azobenzene) (blue).

The extinction spectra of the self-assembled AuNR chains were measured by UV-vis during the course of the self-assembly (**Figure 4.2.4**). The results show that the peak at around 530 nm, which belongs to the transverse surface plasmon band, did not shift, while the spectral position of the LSPR at around 780 nm exhibited a time-dependent red-shift. This shift in the position of the LSPR peak suggests that the AuNRs self-assembled into an end-to-end structure. After 6 h of self-assembly, the position of the maximum of the LSPR stop shifting, but the self-assembly observed by TEM was still ongoing as observed by the variation in the number of particles per chains observed by TEM (**Figure 4.2.4C**). The discrepancy in the kinetic monitored by UV-vis and TEM was related to the limited plasmon hybridization in long chains of nanoparticles when the interparticle distance is large. The average tip-to-tip distance of adjacent AuNRs was ca. 10 nm. **Figure 4.2.4D** shows the TEM images of mixed suspension at 0 h (left) and 24 h (right). After 24 h, gold nanorods had self-assembled into a well-defined chain through the host-guest chemistry existing between complementary polymer patches at the end of AuNRs.

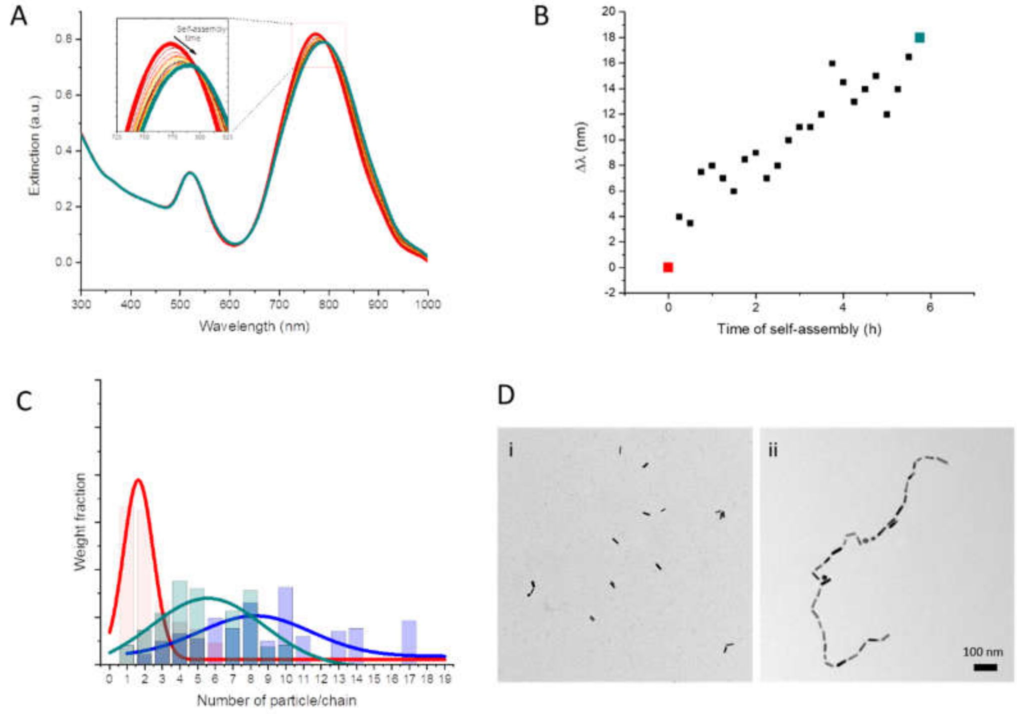

Figure 4.2.4 (A) Extinction spectra of the gold nanorod self-assembled. (B) Variation in the position of the maximum of the LSPR peak. (C) Chain length distribution of the nanorod self-assembly measured by TEM after a 0 h (red), 6 h (green) and 24 h (blue) of self-assembly. (D) TEM images of colloidal assemblies after a self-assembly time of 0 h (i) and 24 h (ii).

The self-assembly of the AuNRs occurred because of the formation of a supramolecular complex between the β-CD and the Azo decorating the AuNRs. The azobenzene can only form this host-guest complex when in its trans conformation due to the favorable hydrophobic interactions and intermolecular van der Waals forces with the β-CD. However, azobenzene in the cis conformation will not form a supramolecular complex with β-CD. Consequently, the formation of the non-covalent interaction between azobenzene and β-CD can be controlled by controlling the conformation of the azobenzene moieties. The transition between the trans and cis conformation of the azobenzene can be triggered with UV-light. Thus, the host-guest chemistry can be controlled by light, and this made the self-assembly of synthesized functionalized AuNRs also controllable and reversible.

The results show that the irradiation of the suspension of complementary AuNRs after 6 h of self-assembly resulted in the dissociation of the self-assembled chains of AuNRs (**Figure 4.2.5**). The change in the LSPR position was plotted as a function of the self-assembly time, *t*. The peak red-shift 23 nm after 6 h. after UV light irradiation for 30 min, the LSPR position blue-shift near the original location because the UV light converted the trans-azobenzene into cis-azobenzene. The host-guest interaction broke between the azobenzene and the β-CD resulting in the disassociation of the chains. Following the irradiation of the AuNRs suspension, the self-assembly resumed, and the LSPR position red-shifted again up to 21 nm after 6 h. This meant that the individual particles reassembled into chains after the irradiation with the UV light. The average number of particles per chain measured initially and after the second round of self-assembly were similar (**Figure 4.2.5B**). These results show that the self-assembly and disassembly can be controlled by light and that the self-assembly process was reversible.

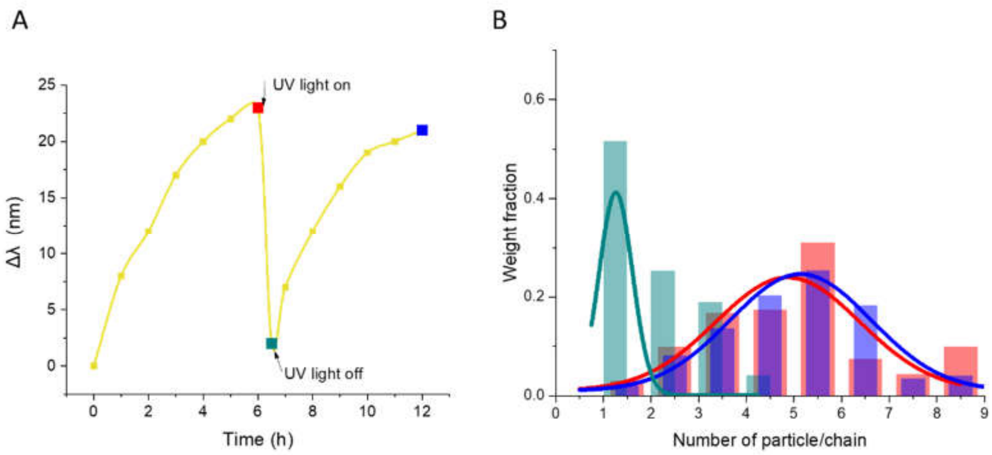

Figure 4.2.5 (A) Variation of LSPR peak positions (λ) with the self-assembly and UV-light irradiation. (B) Chain length distribution of the nanorod self-assembled structures measured by TEM after 6 h (red), after 30 min UV light irradiation (green), and after a second 6 h self-assembly (blue).

The disassembly of the chains not only happened under the UV light irradiation but also can be obtained after the addition of free azobenzene molecules. The host-guest complexes formed by azobenzene and β-CD are dynamic and always shuffling on and off once the equilibrium is reached. As shown in **Figure 4.2.6**, the addition of free azobenzene to the self-assembled suspension resulted in the disassembly of the AuNRs chains. The presence of free azobenzene weakens the interaction between the complementary polymer domains and eventually results in the disassembly of the chains. After the first addition of free azobenzene, the system contained the same number of azobenzene in the polymer ligands and free in suspension. This led to a moderate blue-shift of the LSPR in keeping with a decrease in the average number of AuNRs in the self-assembled chains. The addition of an excess of free azobenzene (10:1) led to a larger blue-shift signifying a more substantial decrease of the average number of AuNRs in the self-assembled chain. After the addition of a large excess of free azobenzene (100:1), the position of the LSPR blue-shifted to reach almost the

LSPR observed before the self-assembly. The average number of nanoparticles measured by TEM confirmed those results. Consequently, the chain length can be efficiently controlled by the addition of free azobenzene in the environment.

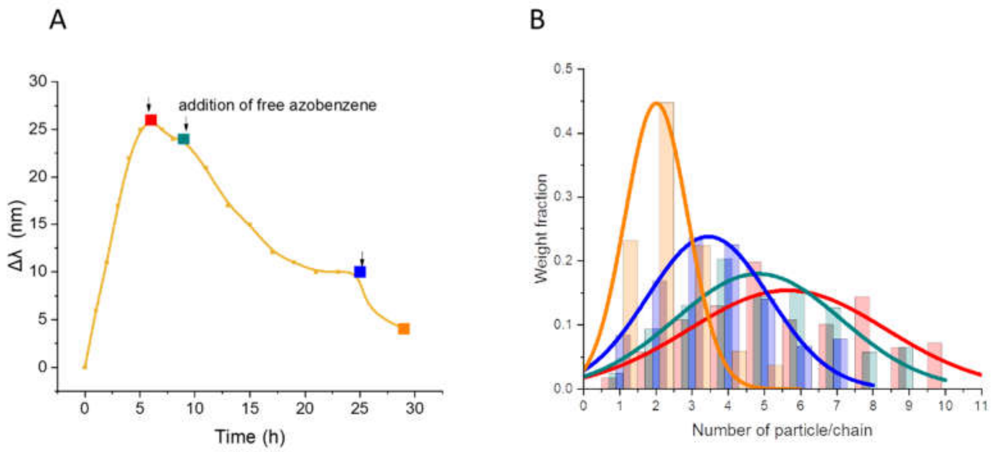

Figure 4.2.6 (A) Variation of LSPR peak with the self-assembly time and the addition of free azobenzene. (B) Chain length distribution of the nanorod self-assembled structures measured by TEM after the addition of free azobenzene molecule at a molar ratio to the β-cyclodextrin of 0 (red), 1 (green), 10 (blue) and 100 to 1 (orange).

4.2.3 Conclusion

End functionalized gold nanorods with SH-poly(DMAEMA-*co*-cyclodextrin) and SH-poly(DMAEMA-*co*-azobenzene) polymer have been successfully prepared. Using the host-guest chemistry between azobenzene and β-cyclodextrin, the self-assembly of gold nanorods to form plasmonic polymers can be easily controlled. The AuNRs assembly was triggered by mixing the two complementary functionalized AuNRs suspensions resulting in the formation of a host-guest complex. The resulting plasmonic polymer can be broken and recombined by irradiation. The average number of AuNRs in the self-assembled structure can also be controlled by the addition of free azobenzene to the system. Such supracolloidal assembly can be used to monitor the condition of the environment due to the coupling of the localized plasmon leading to a significant shift in the position of the longitudinal surface plasmon resonance.

4.3 Using solvent quality to control the directionality during the self-assembly of polymer functionalized colloidal nanoparticles[1]

In the previous sections, the directionality during the self-assembly of gold nanoparticles was introduced by using end-functionalized nanorods, i.e. building blocks having an intrinsic directionality. However, such directionality can also be observed using isotropic building blocks. In this section, the directionality during the self-assembly of polymer and inorganic spherical nanoparticles functionalized with end-tethered polymer chains was controlled by tuning the solvent quality, and the directionality was the result of the delicate balance of forces present at the nanoscale.

4.3.1 Introduction

The rapid reduction in the size of technological components and their increased complexity requires practical strategies to build complex structures from small elementary units, like functional nanoparticles (NPs), while generating materials with macroscale dimensions.[216-218] Thus, to develop new applications and gain fundamental insight, the ability to control the morphology of colloidal material is becoming increasingly important.[219, 220] Top-down approaches, like photolithography[59] or 3D printing,[221] where tools are controlled tools to create, cut, mill and shape materials with desired shape and order have been extensively used to create the complex structured material needed to address our technological needs. However, bottom-up approaches based on the assembly of colloidal particles,[222] offer alternatives to the expensive and

---

time-consuming top-down approaches to produce colloidal materials that have complex structures.[108] Furthermore, such strategies can produce materials with higher structural complexity. However, the final properties of the self-assembled materials are tightly related to the manner into which the colloidal building blocks are joined together.

Typically, during self-assembly, NPs will form close-packed structures. However, the ability to make more complex structures, either non-close-packed or directional would provide the freedom needed to produce supracolloidal assembly with new properties finding applications in different areas, such as chiral catalysis,[223] sensing,[224] optical metamaterials,[225] or medical diagnosis.[226] The preferential formation of close-packed structures is driven by the thermodynamic equilibrium leading to the formation of the assembled structures with the minimum conformational free energy.[227] To access non-close-packed and directional structures much effort have been devoted to study the assembly of anisotropic NPs.[228, 229] In such cases, either nanoparticles with specific shape (rods,[230] triangles,[231] bypyramids[232]) or patchy particles, i.e. particles with inhomogeneities on their surface composition,[109, 233] were used to produce a far richer and complex range of structures.

However, isotropic NPs with a homogenous surface composition can also be used to produce directional assemblies. For a limited number of NP compositions, directional assemblies can be prepared through field-assisted methods,[234, 235] but this strategy is limited to NPs that are intrinsically magnetic or possess a permanent dipole. Typically, in most cases, bare NPs will undergo unavoidable and uncontrolled agglomeration due to core-core van der Waals forces.[236] To suppress this phenomenon, NPs can be functionalized with molecular ligands, often polymers.[237] This results in an increase the NPs stability either through electrostatic, steric, or interfacial tension repulsion. In addition to preventing aggregation, the resulting canopy can be engineered to allow for directional self-assembly. The chemical and physical nature of the ligands on the surface of the NPs can be harnessed to controllably induce self-assembly, which can lead to the formation of 1D chains in some instances.[238] The directionality in the self-assembly process is the delicate result of the balance of forces present between the NPs due to the forces at play, such as van der Waals forces,[239] dipole-dipole interactions,[240] electrostatic forces,[241] hydrogen bonding,[242] π–π stacking interactions,[243] or halogen bonding.[244]

Furthermore, when polymer ligands are used to stabilize the NPs, the balance of nanoscale forces leading to directionality can be tuned with the solvent quality of the self-assembly media for the ligands.[141] The solvent quality affects the dynamics and conformation of the polymer ligands,[236, 245] and in some cases influences the type of self-assembled structure formed.[246,247] Reducing the solvent quality can be used to trigger the self-assembly itself,[248] but also to control the structure of the resulting structures. Increasing the solvent quality of the environment can change the morphology of the brush and the stability to the nanoparticles in suspension.[245, 249] Because the swollen polymer brushes shield the nanoparticles from the core-core van der Waals interaction. The presence of such mobile ligands, or the presence of surfactants, increases the repulsion between the nanoparticles to a point where they dominate the attractive van der Waals forces acting between the nanoparticles. Consequently, the suspension is stable and the nanoparticles aggregation is prevented.[63, 250] Although the morphology of the polymer ligands and the stability of the particles can be adjusted with the solvent quality, the control of the interactions present between the nanoparticles during self-assembly is complex and using this phenomenon to control the type of assemblies formed remains challenging.

Here, NPs with different core compositions either swollen crosslinked polymer NPs, silica NPs or gold NPs were functionalized with the same canopy of polymer ligands, either poly(methyl methacrylate-*co*-2-(dimethylamino)ethyl methacrylate) (PMMA-*co*-PDMAEMA) or poly(methyl methacrylate-*co*-methacrylic acid) (PMMA-*co*-PMAA). Upon mixing, the nanoparticles functionalized with those complementary polymer ligands undergo self-assembly. The quality of the solvent for the PMMA ligands was tuned while keeping the dielectric constant of the solvent similar using mixtures of solvents and non-solvents. By changing the solvent quality, the morphology and the mobility of the PMMA brush was changed and influenced the self-assembly process (**Figure 4.3.1**).

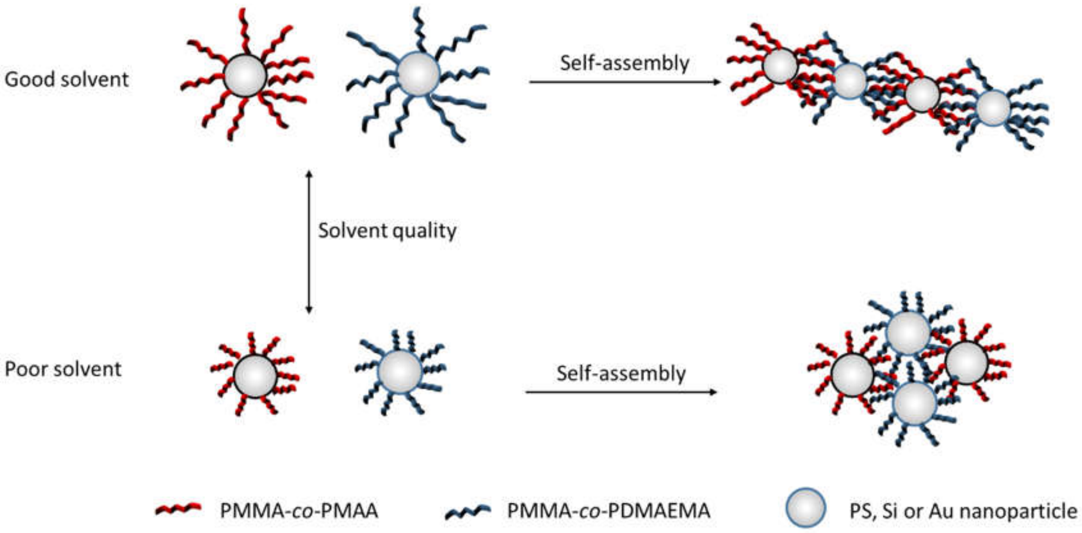

Figure 4.3.1. Influence of the brush conformation on the self-assembly of polymer-functionalized nanoparticles to form different supracolloidal assemblies in selective solvents.

4.3.2 Results and discussion

A library of core-canopy nanoparticles with a core of polystyrene, silica or Au grafted with a canopy of poly(methyl methacrylate-*co*-2-(dimethylamino)ethyl methacrylate) (PMMA-*co*-PDMAEMA) or poly(methyl methacrylate-*co*-methacrylic acid) (PMMA-*co*-PMAA) with different length (*N*) were prepared. As shown in **Table 4.3.1**, two different lengths of polymers have been grafted from the surface of the different core. The ratio between the reactive monomer (DMAEMA or MAA) and MMA in each chain was 3 to 7. The particles were dispersed in different solvents and solvent mixtures. The composition of the solvent mixtures was chosen for their selectivity toward the different components of the polymer system. Mixtures prepared were based on the combination of: THF a good solvent for both PS and PMMA; cyclohexane a theta solvent for PS and a non-solvent for PMMA; methyl acetate a good solvent for PMMA and a non-solvent for PS.

The size of the synthesized nanoparticles was measured by DLS in different solvent conditions. When the solvent quality for the polymer brushes decreased due to the addition of a selective non-solvent, the particle size decreased. This is because, upon the addition of cyclohexane, the PMMA brushes adopt a collapse conformation.[141] This deswelling observed is in agreement with the Flory-Huggins interaction parameter ($\chi_{\text{polymer-solvent}}$) of PMMA in the solvent mixtures (**Table 4.3.2**).

Table 4.3.1 Library of polymer-functionalized nanoparticles prepared.

Nanoparticle	Brush	*N*	Particle size (nm)	
			THF	$THF_{0.5}$+$CH_{0.5}$
PS	PMMA-*co*-PDMAEMA	20	212	190
		100	241	203
	PMMA-*co*-PMAA	20	220	195
		100	245	201
Si	PMMA-*co*-PDMAEMA	20	164	140
		100	197	152
	PMMA-*co*-PMAA	20	166	135
		100	195	149
Au	PMMA-*co*-PDMAEMA	20	85	70
		100	111	82
	PMMA-*co*-PMAA	20	83	69
		100	107	80

When the complementary nanoparticles were mixed, the formation of supracolloidal structures was observed in every solvent mixture used. For a given solvent mixture, the length of the polymer brushes tethered to the NPs did not significantly alter neither the kinetic of association nor the type of supracolloidal assembly observed (**Figure 4.3.2A**). As the time of self-assembly increased, the average number of NPs in each self-assembled supracolloidal structures increased linearly. The rate of self-assembly was moderately faster for the NPs functionalized with the longer polymer chains, likely because the self-assembly involved the interdigitation of the chains bearing acid groups and the chains bearing amino groups, which can be promoted given the increased mobility of longer grafted chains.[141, 245] Thus, the interdigitation can occur more rapidly when the PS NPs were functionalized with longer copolymers of PMMA, resulting in a moderate increase in the rate of self-assembly.

However, when the solvent quality for the polymer system was varied, significant differences in both the type of supracolloidal structure formed and the rate of self-assembly were observed (**Figure 4.3.2.B**). Three different solvent mixtures were used to carry out the self-assembly; pure THF a co-solvent for both the PS core and the PMMA canopy, a 1:1 mixture of THF and cyclohexane where the PS core was in a good solvent and the PMMA brushes in a poor solvent, and a 5:95 mixture of THF and methyl acetate where the PS core is in a non-solvent and the PMMA chains are in a good solvent. The variation of the solvent quality for the PS core did not influence the self-assembly process, which suggests that the self-assembly was almost purely driven by the brushes. In contrast, when the self-assembly was carried out in a poor solvent for the PMMA brushes, the self-assembly rate sharply increased, suggesting that the steric repulsion created by the tethered polymer ligands was very limited in a poor solvent for the brushes. Furthermore, the structure of the supracolloidal assembly obtained in the poor solvent for PMMA were close-packed clusters, while the self-assembled structures obtained in a good solvent for PMMA produced mostly linear chains.

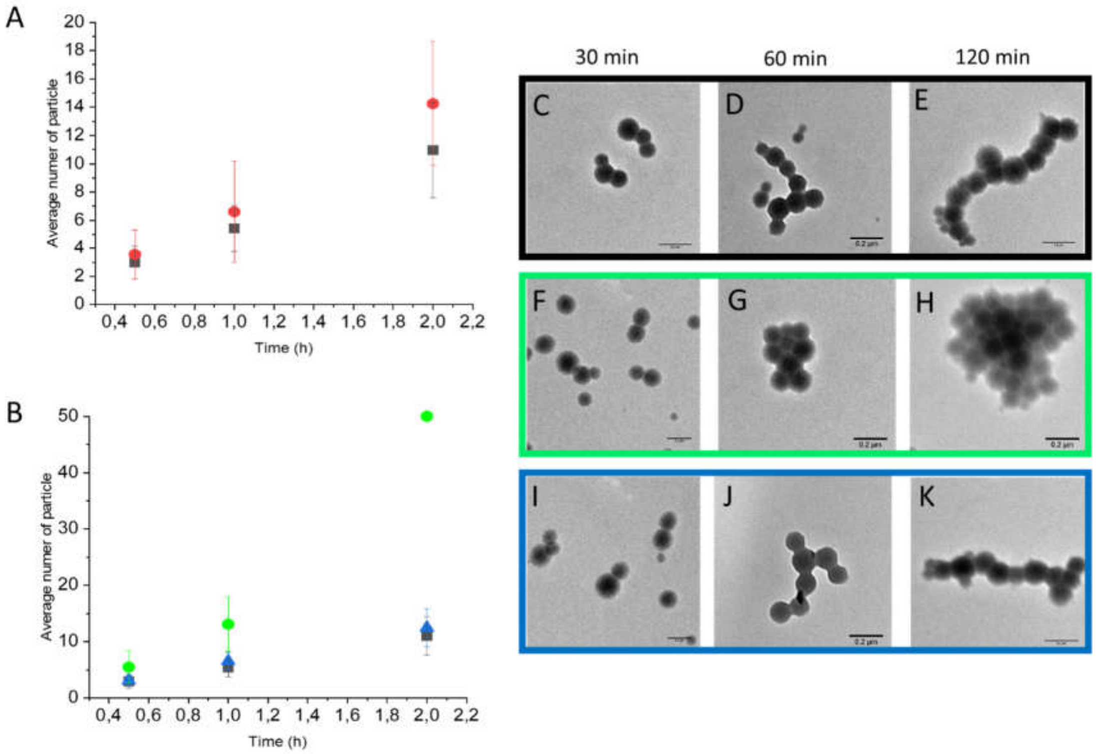

Figure 4.3.2 (A) Average number of particles in the supracolloidal assembly formed with PS-PMMA NPs functionalized with long (red) and short (black) PMMA chains. (B) Average number of particles in the supracolloidal assembly formed with PS-PMMA NPs in different solvent mixtures. THF (black), $THF_{0.5}$+$Cyhlohexane_{0.5}$ (green), $THF_{0.05}$+Methyl $acetate_{0.95}$ (blue). (C-K) TEM images of the supracolloidal assemblies. (C,D,E) in THF, (F,G,H) in $THF_{0.5}$+$cyhlohexane_{0.5}$, and (I,J,K) in $THF_{0.05}$+methyl $acetate_{0.95}$ obtained after 30 min., 1 h or 2 h of self-assembly.

The self-assembly process was strongly driven by the PMMA brushes. In addition to the influence of the solvent quality and the similar assembly observed with swollen and deswollen PS NPs core, the same self-assembly behavior was observed when the PS cores were substituted by Si NPs (**Figure 4.3.3**). In a good solvents for the PMMA, linear assemblies were observed, while in the THF:cyclohexane mixture, cluster formation was observed. The Flory-Huggins interaction parameter $\chi_{\text{polymer-solvent}}$ of PMMA in different solvents can be used to analyze the self-assembly process (**Table 4.3.2**).

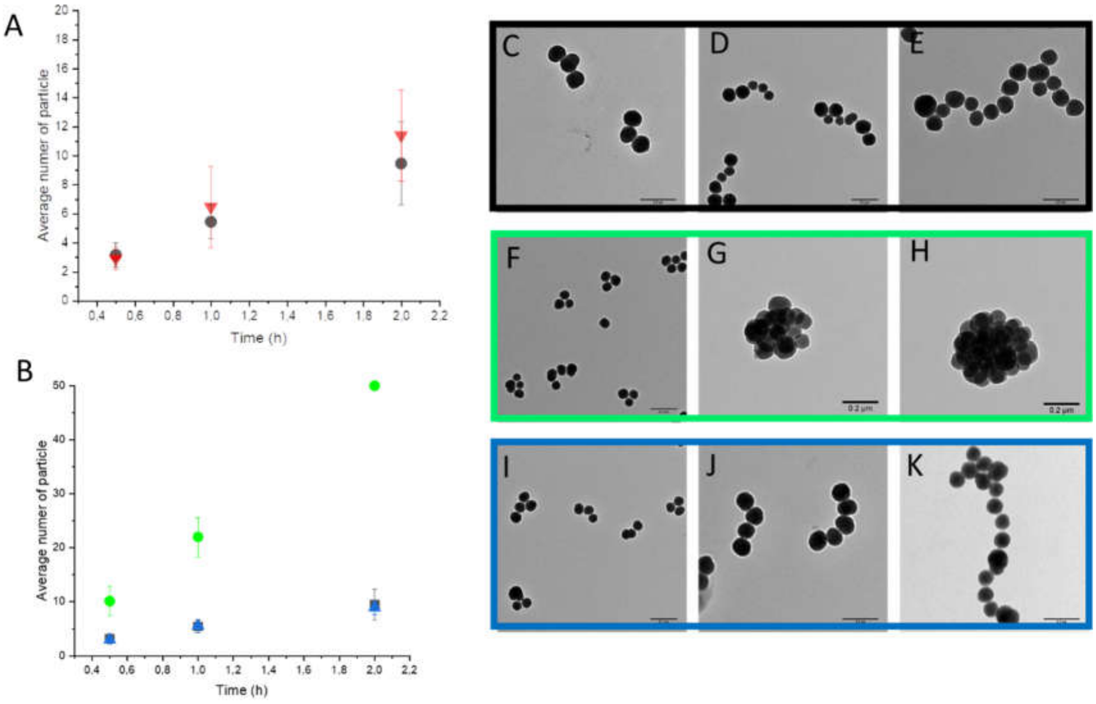

Figure 4.3.3 (A) Average number of particles in the supracolloidal assembly formed with Si-PMMA NPs functionalized with long (red) and short (black) PMMA chains. (B) Average number of particles in the supracolloidal assembly formed with Si-PMMA NPs in different solvent mixtures. THF (black), THF$_{0.5}$+cyhlohexane$_{0.5}$ (green), THF$_{0.05}$+Methyl acetate$_{0.95}$ (blue). (C-K) TEM images of the supracolloidal assemblies. (C,D,E) in THF, (F,G,H) in THF$_{0.5}$+cyhlohexane$_{0.5}$, and (I,J,K) in THF$_{0.05}$+methyl acetate$_{0.95}$ obtained after 30 min., 1 h or 2 h of self-assembly.

Table 4.3.2. Flory-Huggins interaction parameter $\chi_{\text{polymer-solvent}}$ of PMMA in different solvent mixtures and the self-assembly rate observed in those solvent mixtures.

Solvent	χ_{PMMA}	k ($\text{nM}^{-1}\ \text{h}^{-1}$)			
		short brush		long brush	
		PS	Si	PS	Si
THF	0.332	24 ± 1	21 ± 3	33 ± 2	22 ± 2
$\text{THF}_{0.5}$+$\text{Cyhlohexane}_{0.5}$	0.704	97 ± 20	110 ± 8	94 ± 20	120 ± 5
$\text{THF}_{0.66}$+$\text{Cyhlohexane}_{0.34}$	0.519	-	-	49 ± 3	54 ± 1
$\text{THF}_{0.8}$+$\text{Cyhlohexane}_{0.2}$	0.421	-	-	38 ± 2	46 ± 3
$\text{THF}_{0.05}$+Methyl $\text{acetate}_{0.95}$	0.416	28 ± 2	19 ± 1	29 ± 2	22± 1

To understand the effect of the solvent quality more in-depth, the solvent quality was varied by the addition of different molar fraction of cyclohexane in THF (**Figure 4.3.4**). The $\chi_{\text{PMMA-solvent}}$ was varied from 0.33 to 0.70. As the quality of the solvent for the PMMA brushes decreased, the rate of self-assembly increased linearly. However, the relationship between the collinearity of the NPs in the self-assembled structures and the solvent quality was more complex. The fraction of linear segments in the self-assembled structures was defined as the fraction of NPs in contact with two neighboring NPs amongst the nanoparticles having two or more neighboring NPs. While in pure THF, the fraction of linear segment in the assembly of both PS-PMMA and Si-PMAA were similar, the fraction of linear segments in the supracolloidal structures decreased more steeply for the Si-PMMA NPs than for the PS-PMAA NPs. This result suggests that the balance of forces acting on the NPs were different for the PS and the Si NPs.

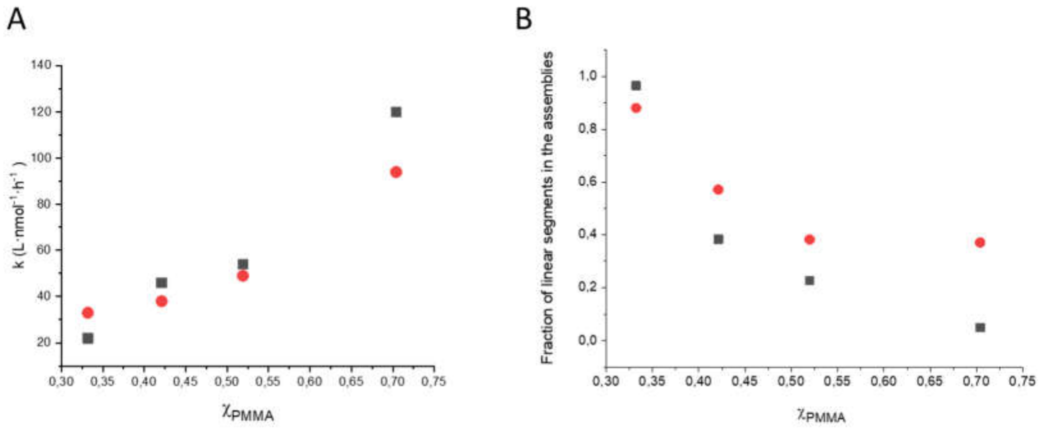

Figure 4.3.4 Influence of the solvent quality on the self-assembly process. (A) Self-assembly rate and (B) fraction of linear segments in the supracolloidal assemblies after 30 min of self-assemblies. For PS-PMMA (red) and Si-PMMA (black) NPs.

The forces acting at the nanoscale on the system undergoing self-assembly are multiple and complex. The main component in the system of PS-PMMA and Si-PMMA NPs are the core-core van der Waals attraction and the steric repulsion generated by the PMMA brushes. The vdW attraction between two NPs of radius *r* can be roughly approximated by[251]:

$$U_{vdW} = -\frac{\left(\sqrt{A_{NP}}-\sqrt{A_S}\right)^2 r}{12\,d} \qquad \text{Eq. 4.3.1}$$

where A_{NP} and A_s are the Hamaker constants of the NPs and for the solvent, respectively, and *d* is the distance between the two NPs. In the case of the PS NPs, given that the PS cores are swollen in the solvent, if the swollen NPs is approximated as a homogenous mixture of polymer and solvent, the Hamaker constant of the swollen NP can be expressed by[252]:

$$A_{NP} = \left(\varphi_P\sqrt{A_P} + (1-\varphi_P)\sqrt{A_S}\right)^2 \qquad \text{Eq. 4.3.2}$$

where A_p is the Hamaker constant of the polymer and φ_p the volume fraction of polymer in the NP. Consequently, the vdW attraction between swollen gel-like NPs becomes:

$$U_{vdW} = -\frac{\left(\sqrt{A_P}-\sqrt{A_S}\right)^2 \varphi_P{}^2 r}{12\, d} \qquad \text{Eq. 4.3.3}$$

Taking into account the swelling of the PS NPs, the attractive vdW interaction between the NPs was systematically smaller for the PS NPs than for the Si NPs (Figure 4.3.5B). Changing the solvent quality for the PMMA brushes led to a variation of the Hamaker constant of the solvent, and as the concentration of cyclohexane was increased, the vdW interaction between both PS and Si NPs decreased.

To compensate for the attractive vdW forces, the polymer brushes provide steric repulsion to stabilize the NPs in suspension. If the polymer layer is considered as an impenetrable cushion, the steric repulsion can be expressed as:[253, 254]

$$U_{Steric} = \frac{\pi r k T \sigma h_0^3}{6Nb^2}\left(-\ln a - \frac{9}{5}(1-a) + \frac{1}{3}(1-a^3) - \frac{1}{30}(1-a^6)\right) \qquad \text{Eq. 4.3.4}$$

$$a = \frac{d-2r}{2h_0} \qquad \text{Eq. 4.3.5}$$

where h_0 is the thickness of the undisturbed polymer brush layer, N the degree of polymerization of the polymer brushes, b the Kuhn length, k the Boltzmann constant, T the temperature, and σ the grafting density of the polymer brushes. As the solvent quality for the PMMA brushes decreased, the h_0 decreased (**Figure 4.3.6**) and the steric repulsion decreased (**Figure 4.3.5C**). Furthermore, due to the swelling of the PS NPs, the effective σ varied with the solvent quality, given that the swelling and deswelling of the PS core induced a change in the distance between the grafting points.

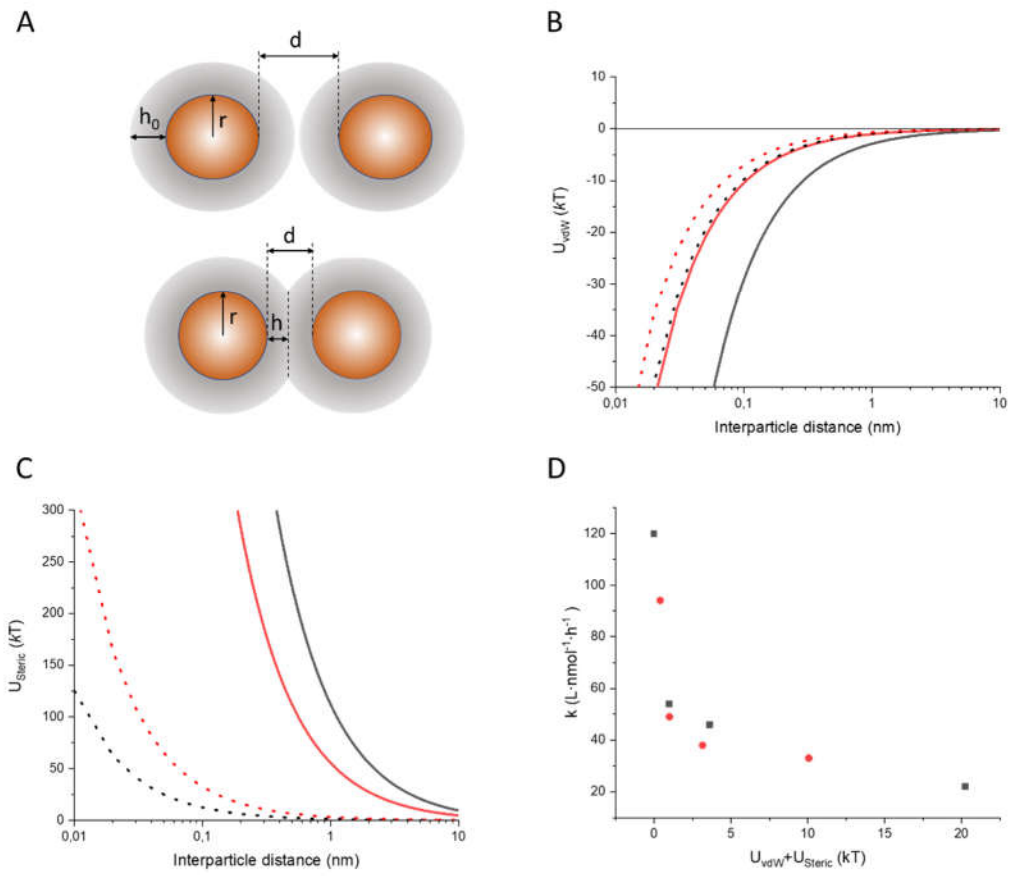

Figure 4.3.5 Nanoscale forces influencing the self-assembly of the PMMA-functionalized nanoparticles. (A) Schematic of non-interacting and interaction nanoparticles. (B) Van der Waals forces between NPs in different solvent mixtures. Si NPs (black) and PS NPs (red), in THF (solid line) or in $THF_{0.5}$+$cyhlohexane_{0.5}$ (dotted line). (C) Steric repulsion between NPs in different solvent mixtures. Si NPs (black) and PS NPs (red), in THF (solid line) or in $THF_{0.5}$+$cyhlohexane_{0.5}$ (dotted line). (D) variation of the self-assembly rate with U_{vdW}+U_{steric} calculated at a interparticle distance of 5 nm for Si NP (black), PS NP (red).

However, eq. 4.3.4 assumes that the brushes did not undergo interdigitation. Nevertheless, the main driving force of the self-assembly was the formation of acid-base pairs between the PMMA-*co*-PMAA and the PMMA-*co*-PDMAEMA chains, which can only occur through interdigitation. It can be assumed that this interdigitation remained mostly constant across the different systems, given that the main driving force for this will be the chemical composition of the brush. Furthermore, during the formation of the supracolloidal assembly, the total surface area between the NPs and the solvent would be reduced, which can also contribute to the favorable attractive interaction leading to the formation of the assemblies. Nonetheless, by considering only the contribution of the vdW attraction and the brushes steric repulsion, the self-assembly rate increased with the molar fraction of cyclohexane present in the solvent mixture can be explained qualitatively (**Figure 4.3.5D**). Given that the average nanoparticle distance observed by TEM was ca. 5-8 nm, if the energetic balance Is considered at that interparticle distance, in pure THF, the summation of Eq 4.3.1 and 4.3.4 yielded a large positive energy in keeping with the limited speed of self-assembly. At the same time, in the $THF_{0.5}$+ $cyclohexane_{0.5}$, the $U_{vdW}+U_{Steric}$ was moderately negative, and the self-assembly rate observed was much larger.

The directionality observed can be partially attributed to entropic consideration rather than to enthalpic consideration. When two polymer layers interdigitate, this is accompanied by a rearrangement of the polymer ligands.[255] A gradient in local polymer concentration is created by this redistribution of the polymer chains. After two NPs have formed a junction, the local polymer concentration within the polymer brush layer will be the lowest at the position diametrically opposite to the junction.[255] Consequently, the interpenetration of a third NPs is favored in that region.

The variation in the fraction of linear segments during the addition of the non-solvent and the difference between the PS and the Si NPs can both be ascribed to the ability of the polymer chains that are tethered to the NPs to be redistributed after the formation of a NP-NP junction. To quantify the apparent mobility of the PMMA chains in the different solvent systems, the relaxation time of the PMMA was measured by NMR spectroscopy. Using an inversion-recovery pulse sequence, the spin-lattice relaxation (T_1) of the polymer chains was measured.[256] For grafted polymer chains, an increase in T_1 is typically associated with a decrease in the local mobility of the chain.[245] In a good solvent, when the end-tethered chains are long and the brushes are highly swollen in a good solvent, the chains are more mobile than either short chains in a good solvent or long chains in a marginal solvent. These considerations are in keeping with the experimental results where the preferential linear assembly was observed for low χ_{PMMA}. However, when χ_{PMMA} increased above 0.5, the chains were less mobile, and the preferential linear assembly was consequently no longer favored by those entropic considerations. Finally, recent studies have shown that the stiffness of the NPs core also influences the dynamics of the tethered chains.[141] Here, the PMMA chains grafted on the stiffer silica core displayed a similar reduced local mobility in comparison to the PMMA chains grafted on the swollen PS NPs (**Figure 4.3.6**). Consequently, more linear assemblies were observed with the PS NPs than with the Si NPs in marginal and poor solvents.

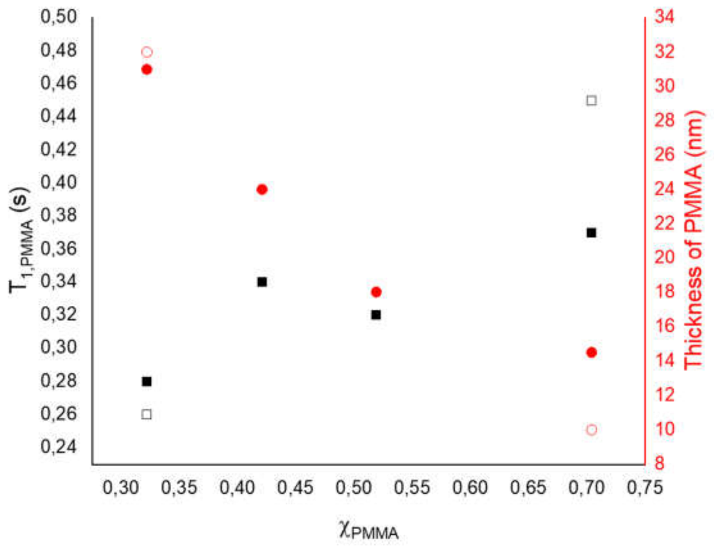

Figure 4.3.6 Effect of solvent quality on the swelling (red) and mobility (black) of the PMMA chains grafted to PS and Si NPs. $T_{1,PMMA}$ of PS NPs (■), $T_{1,PMMA}$ of Si NPs (□), thickness of PMMA chain on PS NP (●), thickness of PMMA chain on Si NP (○).

The results obtained showed that the nanoparticle self-assembly process can be controlled to form more complex structures by changing the solvent quality. For example, the formation of core-satellite complexed structures is one of such targeted structures because of their unique properties; these materials present outstanding optical performance impressive enhancement factors compared with classical SERS agent, which can enable the used of such hierarchical assembly as single object labels labels.[257-259] **Figure 4.3.7A** show the TEM images of supracolloidal assemblies formed with different ratio of large Si NPs (r = 30 nm) functionalized with PMMA-*co*-PMAA and small Au NPs (r = 10 nm) functionalized with PMMA-*co*-PDMAEMA. After 30 min of self-assembly, core-satellite structures with different structures can be formed by tuning the ratio of AuNP:SiNP from 1:1 to 1:50. The self-assembly also allows the formation of nanopillar arrays on curve substrates, and such structure can be formed by the self-assembly of AuNRs and AuNSs. Given the different crystalline facets of the AuNRs, the polymer functionalization with thiolated polymer can be performed only on the tips or on the full surface of the NRs. Tuning the polymer coverage and the solvent quality allowed to control the formation of the pillar array occurring upon the mixing of the AuNRs and AuNSs. Fully covered NRs yielded arrays where the long axes of the NRs were tangential to the AuNSs substrate, and the long axis of the NRs were all aligned. Conversely, when tip-functionalized NRs were used, the NRs were oriented perpendicularly to the AuNS substrate (**figure 4.3.7 D, E**).

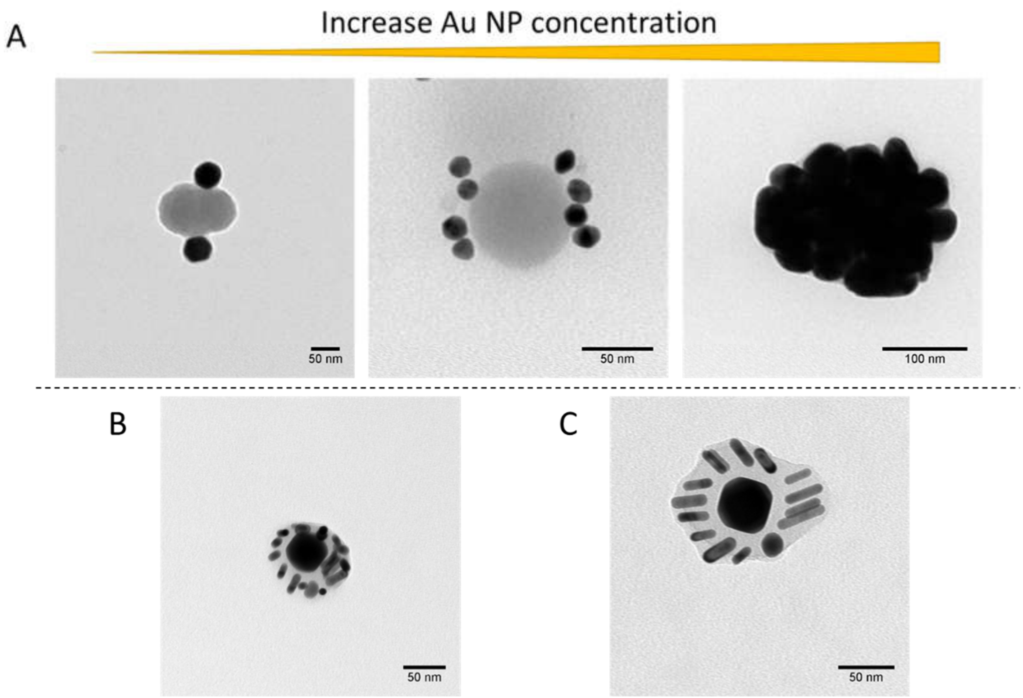

Figure 4.3.7 TEM images of formed core-satellite complexed structures under different ratio. (A) Structures obtained by the combination of AuNPs and SiNPs with a 1:1, 10:1 and 50:1 ratio. (D,E) Structures obtained by the combination of a 10:1 ratio of AuNSs and AuNRs when the NRs were fully covered with polymer ligands (D) or only tip-functionalized (E).

4.3.3 Conclusion

NPs with different core compositions, either swollen crosslinked polymer NPs, silica NPs or gold NPs were functionalized with the same canopy of polymer ligands, either poly(methyl methacrylate-*co*-2-(dimethylamino)ethyl methacrylate), or poly(methyl methacrylate-*co*- methacrylic acid). Upon mixing nanoparticles functionalized with those complementary polymer ligands undergo self-assembly. The self-assembly can be controlled using selective solvent and tuning the solvent quality for the different polymer components. The solvent quality influenced both the self-assembly rate and the final structure of supracolloidal assemblies. The resulting controlled assembly process can be harnessed to generate complex supracolloidal assemblies.

4.4 Self-assembly of anisotropic nanoparticles at the liquid-air interface to form 2D colloidal films

In the previous sections, the linear assembly of isotropic nanoparticles and patchy anisotropic nanoparticles was used to prepare 1D colloidal assemblies in suspensions. The shape of the core and the interaction between the polymer patches played an important role in the formation of the colloidal chains. Furthermore, the assembly could be controlled by changing the condition, such as irradiation and solvent quality. However, in these cases, the directionality of the assembly was only induced in one dimension. Alternatively, the nanoparticles can be assembled in more complex structures, such as 2D colloidal monolayer films. In this section, such films were prepared using patchy polymer-metal anisotropic nanoparticles via the Langmuir−Blodgett technique. Using different nanoparticles, different speeds, and substrate conditions can control the directional self-assembly during the Langmuir−Blodgett process. The present objective was to get well-controlled 2D colloidal monolayer films with distinct structures, especially with the aim to form controlled non-closed packed films.

4.4.1 Introduction

Using self-assembly to organized inorganic nanoparticles (NPs) into a two-dimensional (2D) highly ordered monolayer film has attracted a lot of interest in the past few decades.[260-262] Compared with individual nanoparticles and bulk materials, 2D monolayer films show unique physical and chemical properties because of the interparticle interactions between the constituent particles. This can become especially interesting when the constituting nanocolloids are plasmonic nanoparticles.[80, 263] Such 2D monolayer films have found uses in various fields like electrical,[264, 265] optical,[266] and magnetic devices.[267, 268] To produce such films, different approaches can be used. Self-assembly is a bottom-up method – in contrast to top-down methods like photolithography,[269] electron beam lithography,[270, 271] and nanostencil lithography[272] that all require long experiment time and complex instrumentations – which can be used to rapidly prepare 2D monolayer films at the interface of two immiscible phases and the resulting films can easily be made to cover a large surface area. The resulting films usually have a close-packed structure, cover a large area, and are easily transferable to different substrates.[273-275] However, a significant challenge remains in the formation of colloidal films: the formation of non-close-packed structures. Such films could give rise to a broader range of applications in comparison to closed-packed films due to the potential diversity in structures that could be created.[276]

One of the gold standards in the self-assembly of nanocolloids is the formation of supracolloidal structure made of gold nanoparticles (AuNPs). Such supracolloidal assemblies have been used in many fields such as analysis,[277-279] sensors,[280, 281] and surface-enhanced Raman scattering (SERS) spectroscopy.[282] This is because AuNPs have a localized surface plasmon resonance (LSPR), which depends on the constitutive material properties of the noble metals and the surrounding environment.[283] The LSPR of AuNPs can be controlled by changing the morphology of nanoparticles or tuning the size of the nanoparticles. The LSPR behavior and tailored optical property of the monolayer films formed by the assembly of AuNPs also can be controlled to a certain extent by controlling the orientation and distance between the AuNPs in the supracolloidal assemblies.[284, 285] Consequently, the properties and performance of the colloidal monolayer are strongly influenced by the structure of the monolayer film.[286]

The Langmuir−Blodgett (LB) technique is a powerful method to prepare high-quality monolayers film of nanoparticles at water−air interfaces.[287-289] As the formation of Langmuir films is a slow process, and the nanoparticles can effectively find the energetically most favorable position, the quality of the films can be better controlled than the films fabricated by spin-coating, and other techniques.[290-292] Most monolayer films prepared by Langmuir−Blodgett have been made using isotropic nanoparticles, and they displayed a close-packed structure.[293] In contrast, non-close-packed monolayer films can be made by template-guided deposition.[294] However, it remains a significant challenge to prepare non-close-packed colloidal monolayer film by assembly via the Langmuir−Blodgett technique.

Here, the main goal is to use colloidal nanoparticles to form supracolloidal monolayer films via the Langmuir−Blodgett method and control the film structure with experimental conditions, such as pH, temperature, and pressure. To do so, patchy polymer-metal anisotropic nanoparticles were used. The NPs were functionalized with stimuli-responsive polymer chains, and given the specific affinity of thiolated ligands for specific facets of the AuNPs, anisotropic AuNPs can be specifically site-functionalized. Those particles are used to perform directional self-assembly leading to the formation of different structures. Because of the use of responsive polymer chains to functionalize the AuNPs, changing the conditions before or after forming the monolayer nanocolloidal films such as pH or temperature should induce a change in the solvency of the polymer ligands and control the conformation of the polymer patches. So the structure of the films should change to produce films with different properties. The preparation of those monolayer nanocolloidal films would lead to a fundamental study of the relationship between structures and properties of film materials. The result will further help to understand the relationship between structures and properties of 2D colloidal materials (**Figure 4.4.1**).

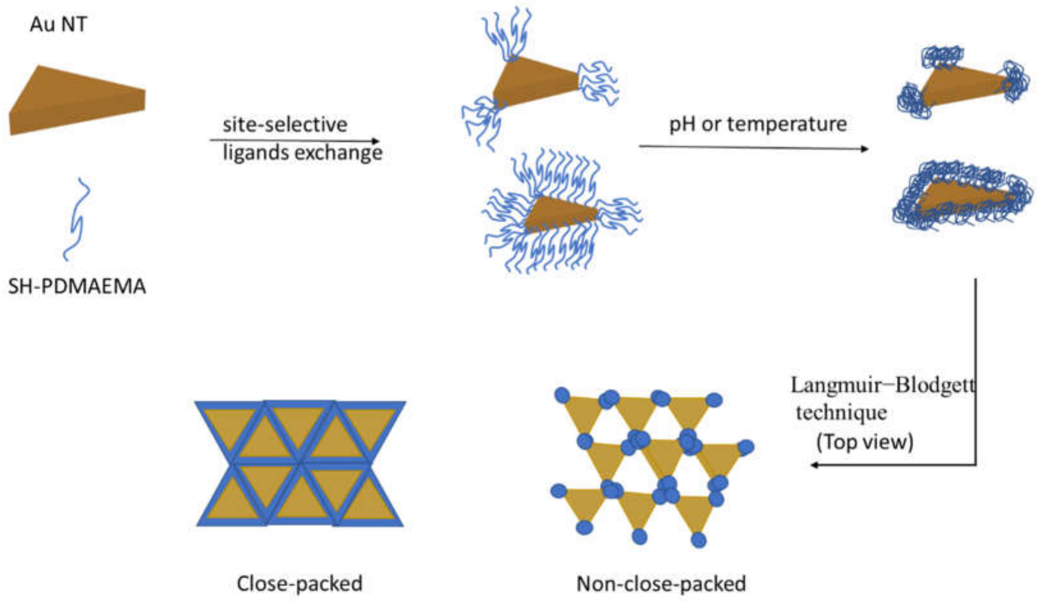

Figure 4.4.1 Schematic of the preparation of monolayer nanocolloidal films with polymer-functionalized anisotropic Au nanoparticles to form different types of self-assembled structures.

4.4.2 Results and discussion:

In order to get the ideal monolayer nanocolloidal films, the building blocks need to be prepared with high shape purity. Gold nanotriangles (AuNT) were synthesized by seedless growth method. The synthesis was carried out in water in the presence of cetylammonium chloride. The extinction of the gold nanotriangles was at ca. 680 nm (**Figure 4.4.2a**). The morphology of the AuNTs was measured by transmission electron microscopy (TEM) and atomic force microscope (AFM). As shown in **Figure 4.4.2**, the building blocks had a triangular morphology. The edge length of the synthesized nanotriangle was ca. 68 ± 7 nm and thickness ca. 4.2 ± 0.8 nm.

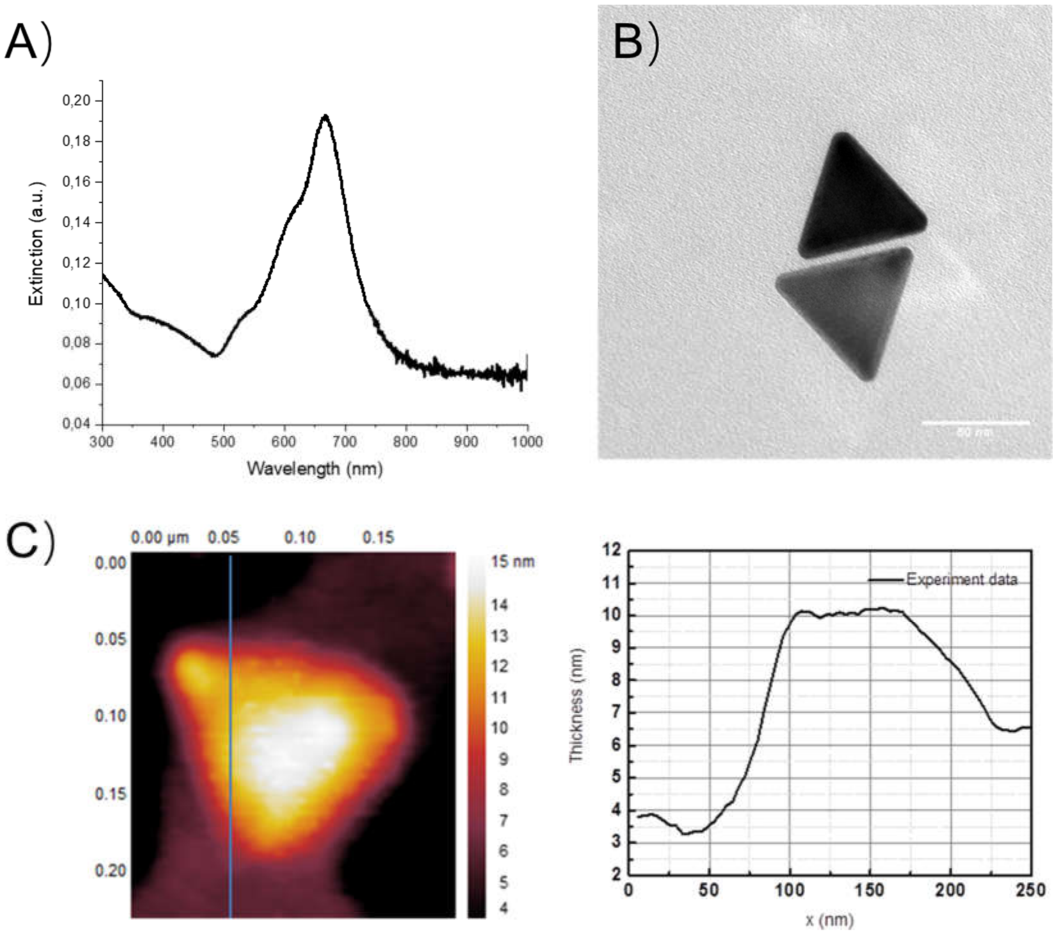

Figure 4.4.2 The UV-vis extinction spectra of gold nanotriangles (A), TEM image (B) and AFM image of the synthesized AuNTs (C).

The AuNTs were functionalized with thiol-terminated stimuli-responsive polymer chains. Poly(2-(dimethylamino)ethyl methacrylate) (PDMAEMA), which is both pH- and temperature- responsive, was used as a ligand to functionalized the AuNTs. The PDMAEMA was synthesized by reversible addition-fragmentation chain-transfer (RAFT) polymerization with an average molecular weight of 15 kDa. The aminolysis of the RAFT chain transfer agent led to the formation of a terminal thiol on the polymer chain, which was then used to do the functionalization of gold nanotriangles. **Figure 4.4.3** shows the functionalization of AuNTs with SH-PDMAEMA in different solvents (THF and Water). The peak at ca. 680 nm did not shift upon the transfer of the gold nanotriangles in the polymer solutions. The moderate red-shift was due to the different solvents influencing the surface plasmon resonance of gold nanotriangles, but no aggregation of the AuNTs occurred during the ligand exchange. Especially for ligand exchange realized in THF, this result means that the ligand exchange succeeded because only the polymer functionalized gold nanotriangles are stable in THF. Otherwise, the gold nanotriangles would aggregate, and the peak would become broader.

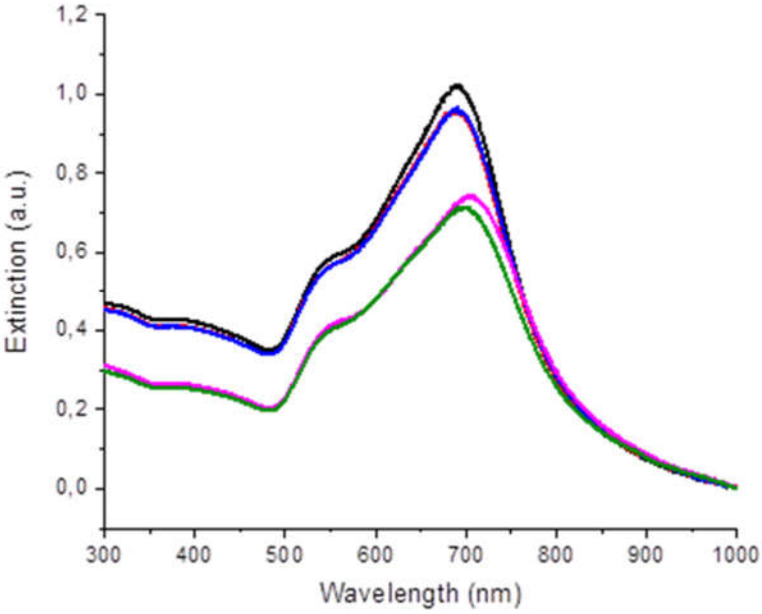

Figure 4.4.3 The UV-vis extinction spectra of the suspensions of AuNTs following their functionalization with SH-PDMAEMA in different solvents. Original AuNT suspension in water (black), polymer-functionalized AuNT in water directly after ligand exchange (red), polymer-functionalized AuNT in water 18h after ligand exchange (blue), polymer-functionalized AuNT in THF directly after ligand exchange (pink) and polymer-functionalized AuNT in THF 18h after ligand exchange (green).

PDMAEMA is soluble in both aqueous and organic solvents and can be used to stabilize the AuNTs in an array of solvent conditions. In order to make colloidal films at the air-liquid interface, or the liquid-liquid interface, it was essential first to assess the solubility of the nanoparticles and their ability to remain at the interface. Initially, the AuNTs are stabilized with cetylammonium surfactants. After the site-selective polymer functionalization, with a low concentration of thiolated polymer ligands, the polymer chains were tethered only at the edges of the AuNTs, while the flat faces of the AuNTs, remained coved with the small molecule surfactant.

First, the AuNT-PDMAEMA were redispersed in toluene and mixed with the same amount of water. After shaking the mixture by hand, the AuNT-PDMAEMA move to the toluene-water interface (**Figure 4.4.4**) due to the mixed surface coverage, as observed by the dark blue interfacial film. When all the toluene evaporated, the AuNT-PDMA remained at the water interface and did not disperse into the water phase. Choosing the right organic solvent to cast the AuNTs on the water subphase is also very important. The solvent needs to evaporate; be compatible with PDMAEMA and its density must be smaller than water. When suspensions of nanotriangle in toluene were used, aggregation of the nanoparticles on the surface of the bath was observed, leading to macroscopic segregated islands of NPs. There was no change in the surface tension of the bath observed. However, when a suspension of NPs in THF was used, no macroscopic separation was observed. The main difference was caused by the miscibility of the THF in the water subphase. The AuNT suspension in toluene dried, forming small droplets at the surface of the LB bath. However, when a diluted THF suspension was used, the THF diffused in the subphase, leaving a homogenous film of AuNTs at the interface.

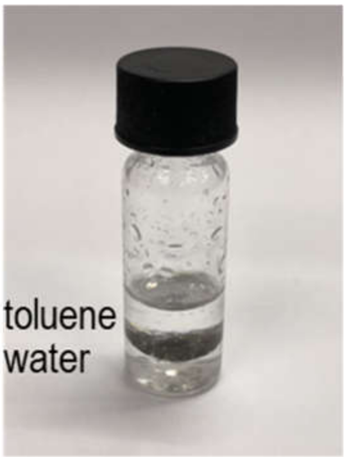

Figure 4.4.4 Image of the transfer AuNT-PDMAEMA to the water interface.

After carefully depositing 0.2 mL of a 1.5 mg/mL AuNT suspension in THF, the bath was left standing still for about 10 min to let THF evaporate completely. This was monitor by looking at the surface tension over time. When pure THF was used, following the addition of THF, the surface tension dropped from 72 mN/m to 42 mN/m, and after 10 min, the surface tension of the bath was back to 72 mN/m, indicating that all the THF was evaporated.

In the case of the addition of NP suspension (**Figure 4.4.5A**), the surface tension dropped after the addition of the suspension, and after ca 10 min, it reached equilibrium at a surface tension of ca. 53 mN/m, indicating the evaporation of the THF and the presence of NPs at the air/water interface. Once this equilibrium was reached, the barriers of the bath were moved to compress the NP monolayer.

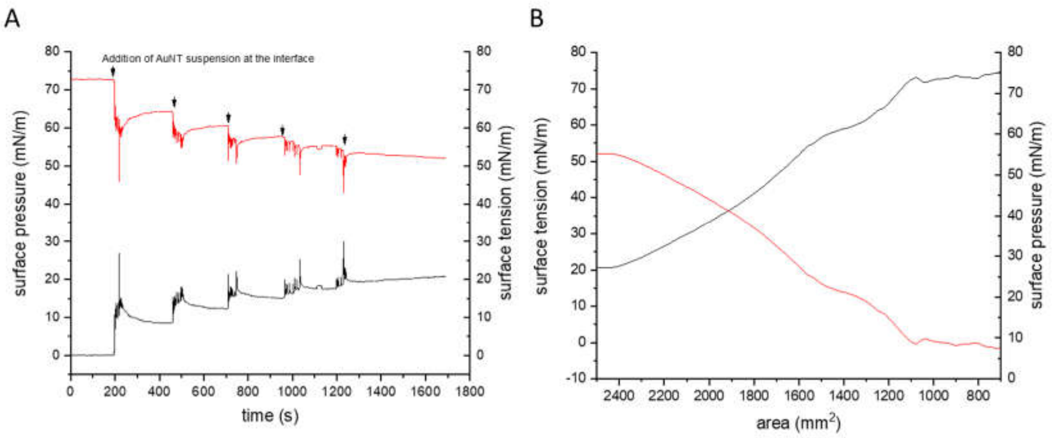

Figure 4.4.5 (A) The change of surface tension and surface pressure after the addition of the suspension, (B) The evolution of surface tension and surface pressure during the decrease of the total area with 0.2 mL suspension. Surface pressure (black), surface tension (red).

Figure 4.4.5B shows the change of the surface pressure and surface tension with total area. As the total area decreased, the surface pressure increased. When the total area was smaller than 1100 mm^2, the surface pressure and surface tension reached a plateau and both of them did not change with a further reduction of the total area. This is because, at 1100 mm^2, the gold nanotriangles formed a close-packed monolayer film, so 1100 mm^2 is the critical area for surface pressure and surface tension.

In order to control the area of the prepared monolayer films, the relationship of added suspension and area was calculated (**Table 4.4.1**). The final area of the monolayer film can be controlled by using different amounts of AuNT-PDMAEMA suspension. **Figure 4.4.6** shows the change of the surface pressure and surface tension with total area. When the total area decreased, the surface pressure increased. After reaching an area of 1250 mm^2 (0.2 mL of AuNT suspension), 2350 mm^2 (0.4 mL of AuNT suspension), or 3250 mm^2 (0.5 mL of AuNT suspension), a discontinuity in the surface pressure was observed, potentially corresponding to the formation of a homogenous monolayer. The critical area was different when using different amounts of suspension and in keeping with the number of AuNT added to the bath. Still, in every case, the critical area observed was smaller than the area predicted by calculation. This discrepancy could result from a misestimation of the number of nanoparticles in suspension (based on the size of the AuNT, the density of gold, and the concentration of gold in the suspension) or because not all the AuNT-PDMAEMA were located at the air-water interface.

Table 4.4.1. The calculation result of ideal monolayer colloidal film with different amounts of Au NT suspension.

Volume of AuNT suspension of 1.5 mg/mL	Area of resulting close-packed monolayer
0.1 mL	950 mm^2
0.2 mL	1900 mm^2
0.3 mL	2850 mm^2
0.4 mL	3800 mm^2
0.5 mL	4750 mm^2

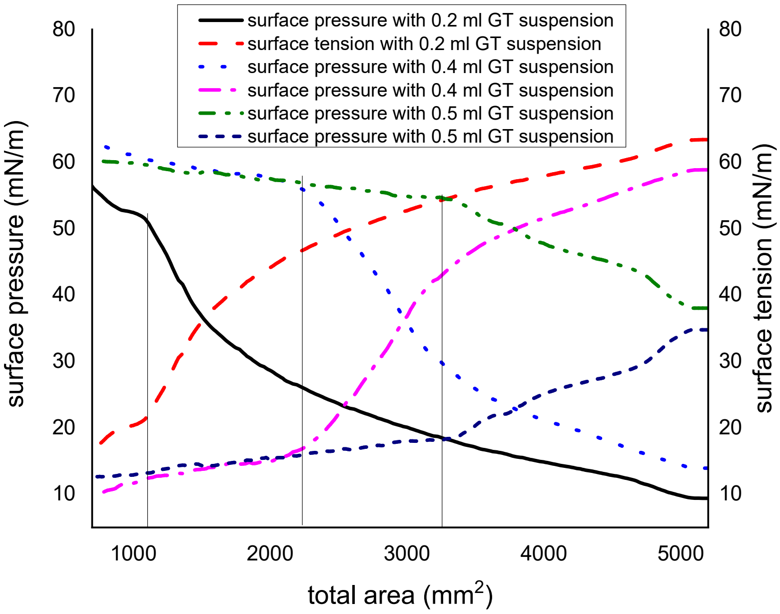

Figure 4.4.6. The change of surface tension and surface pressure for films formed with different amount of AuNT-PDMAEMA suspension

There are different methods to transfer the film onto solid substrates like glass, Si wafer, or TEM grids. The films can be transferred either by the Langmuir-Blodgett, Langmuir, or Langmuir-Schaefer method. Choosing the right way to transfer the film is very important because the film can be broken during the transfer process. **Figure 4.4.7** shows the TEM images of the transferred gold nanotriangle Langmuir-Blodgett film or Langmuir film. The films were prepared with the same batch AuNT, same compression speed, and same transfer point. Structural differences between the films were clearly visible (**Figure 4.4.7**). The Langmuir-Blodgett method should lead to the formation of a bilayer. However, the films obtained displayed aggregation of the AuNT, not the layered films expected. For the Langmuir film, the quality of AuNT is not ideal, but areas of monolayer film can be found by TEM. Compared with the Langmuir-Blodgett film, the Langmuir film appeared to be a better way to transfer the films.

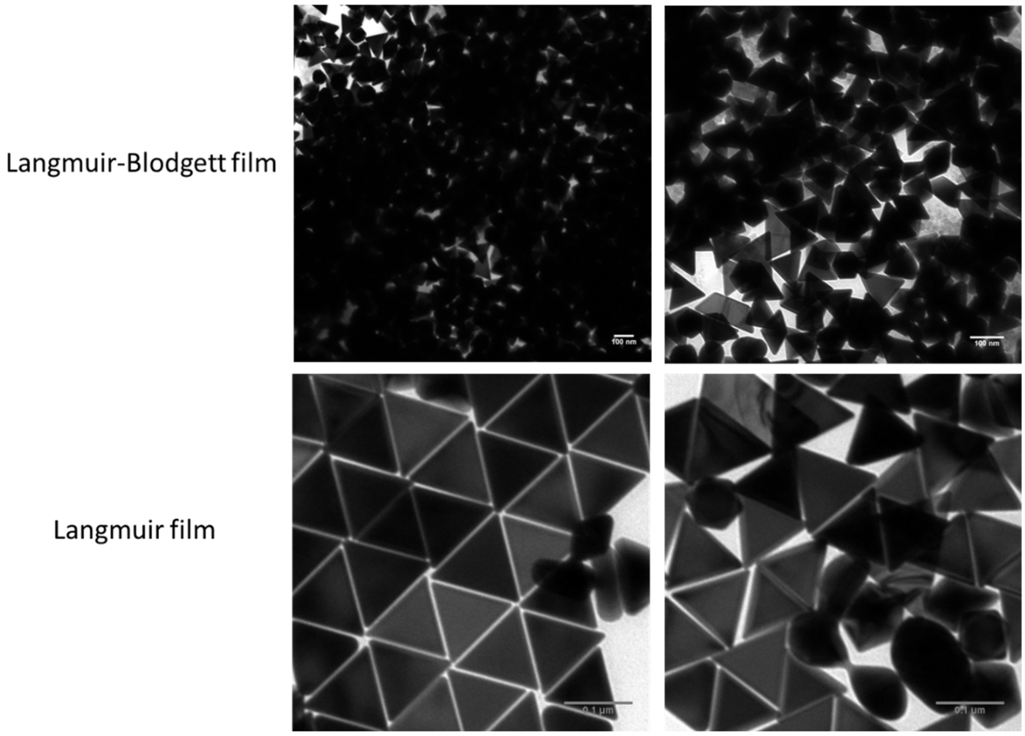

Figure 4.4.7. TEM images of the Langmuir-Blodgett film or Langmuir film.

Figure 4.4.8 shows the UV-vis spectra of gold nanosphere, gold nanosphere film and gold nanotriangle, gold nanotriangle monolayer film after the transfer of the films. The absorption peak of both films did not shift significantly but became broader than the original suspensions. The increased broadness of the plasmon peak could either be ascribed to the formation of the monolayer and the coupling of the plasmon or the uncontrolled aggregation of the nanoparticles.

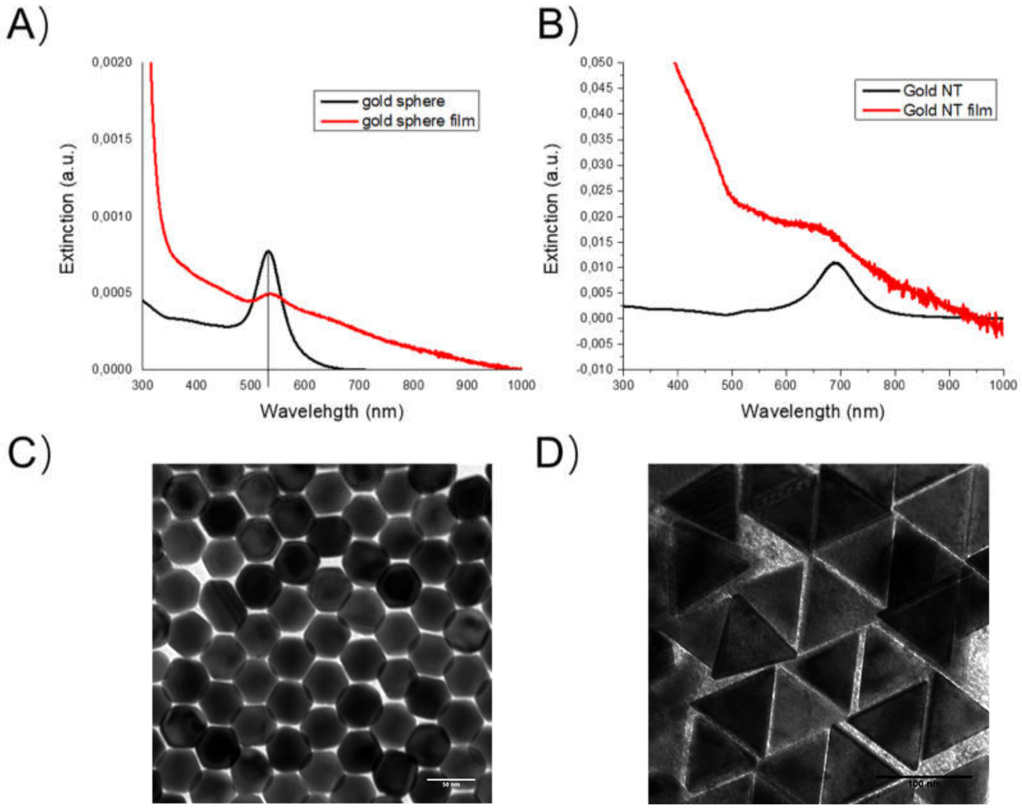

Figure 4.4.8 The UV-vis extinction spectra of gold nanosphere and gold nanosphere film (A), gold nanotriangle and gold nanotriangle film (B) TEM image (C) gold nanosphere film and (D) gold nanotriangle film.

The polymer used, PDMAEMA, is a pH- and temperature-responsive polymer. If the monolayer film were prepared on the interface of solutions with different pH values, the film structure should be different because of the desolvation of polymer patches influencing the type of assembly formed. To investigate this phenomenon, he films were prepared at pH 6.5 and 9.

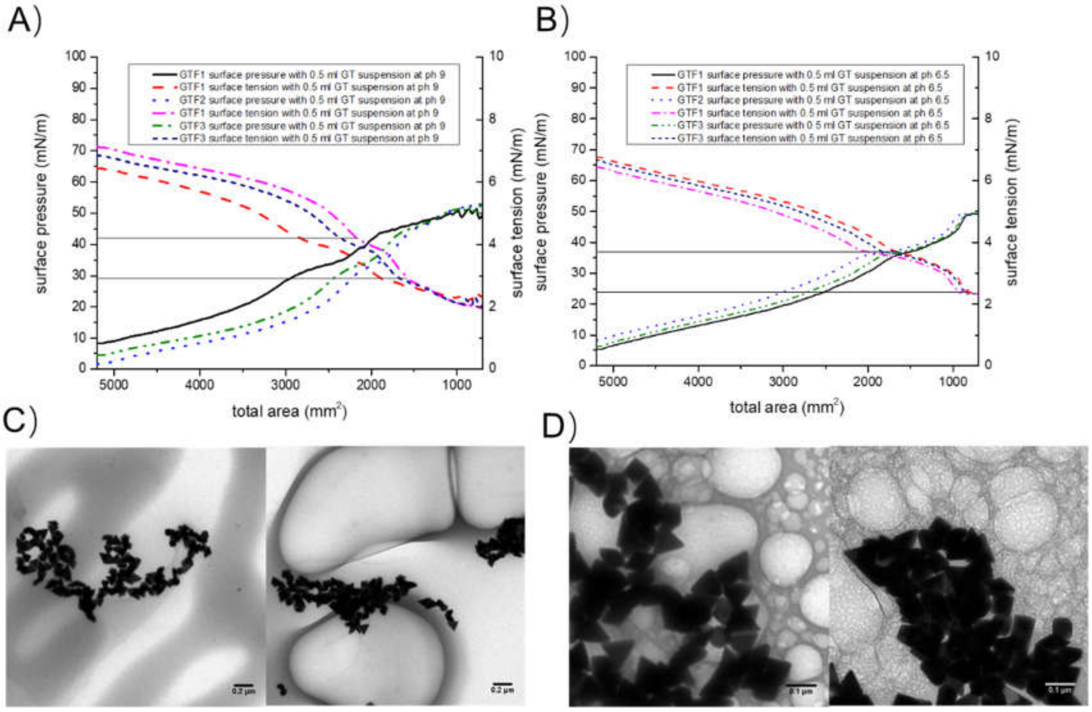

Figure 4.4.9. The results of surface tension and surface pressure for the films prepared at pH 9 (A) and 6.5 (B). TEM image of film at pH 9 (C) and 6.5 (D).

Figure 4.4.9 shows the change of the surface pressure and surface tension with total area at different pH. When the total area decreased, the surface pressure increased. The final surface pressure for the films at pH 6.5 and 9 was not obviously different. The resulting films did not display a monolayer structure, only aggregation was observed. This is likely because the concentration of the buffer used was too high and screened the electrostatic interaction, generated by the presence of remaining surfactant or protonated PDMAEMA, preventing the aggregation of the AuNTs, resulting only in the formation of uncontrolled aggregates.

4.4.3 Conclusion

The PDMAEMA functionalized gold nanoparticles have been successfully prepared. After the site-selective surface functionalization of gold nanoparticles, they stayed at the liquid-air interface. Using the Langmuir−Blodgett technique, monolayers of gold nanosphere and gold nanotriangle film can be successfully obtained. The transfer method and the condition both can influence the structure of the monolayer films. However, multiple parameters affect the structure and the conditions at the surface during the formation of the interfacial films. Unfortunately, the present system was not successful in forming a controlled non-close-packed structure, and the variation in pH led to the uncontrolled aggregation of the NPs rather than the formation of a well-controlled non-close-packed structure. To better control the formation of the interfacial films at different pH values, the AuNTs should be functionalized to provided more steric repulsion between the NPs to prevent the aggregation observed when the ionic strength of the subphase was increased. This functionalization should be produced with short and bulky ligands so not to interfere with the interaction of the PDMAEMA patches.

5. Summary and perspectives

5.1 Summary

In summary, this doctoral dissertation clearly demonstrates how the formation of supracolloidal assemblies can be controlled and used to prepare functional materials, such as photocatalytic membranes. Furthermore, design rules to generate complex supracolloidal structures have been established. Controlling the interaction between the building blocks is an excellent way to tune the final complex supracolloidal structures. Different polymer patches can control the directionality of the self-assembly under different conditions, such as light, temperature and solvent quality. By controlling the interaction between patches, the building blocks can form linear, cluster, core-satellites and monolayer film structures.

In **Section 4.1,** a library of anisotropic Au-CeO_2 nanoparticles with distinct shapes has been synthesized using gold nanosphere, gold nanorod, and gold nanotriangle were used as building blocks to be embedded in nanofibrous membranes by colloidal electrospinning. The resulting supracolloidal assemblies were used to catalyze reactions in flow-through reactors. The assembly of the hybrid polymer/nanoparticle materials was triggered by the flow and elongation of a solution containing the polymer matrix and the nanoparticles during the electrospinning process. The efficiency of the resulting hierarchical materials was controlled by tuning the shape and composition of the nanoparticles embedded in the electrospun membranes.

The formation of supracolloidal assemblies can also be realized by self-assembly. In **Section 4.2,** the host-guest chemistry between azobenzene and β-cyclodextrin was used to form directional linear assemblies of gold nanorods. The nanorods were functionalized with polymers bearing either azobenzene or β-cyclodextrin moieties.

Their combination resulted in the “polyaddition” of the nanorods to yield well-controlled and responsive supracolloidal assemblies. The host-guest chemistry provided a practical method to prepare reversible complex supracolloidal materials responsive to environmental cues.

In **Section 4.3,** isotropic nanoparticles with different core compositions functionalized with polymer ligands were able to undergo either directional or non-directional assembly depending on the solvent quality of the environment. The self-assembly rate or the final structure of supracolloidal assemblies was affected by the solvent quality. On the one hand, the self-assembly rate was related to the colloidal stability of the nanoparticles and the balances of nanoscale forces in the system. On the other hand, the structure of the resulting self-assembly seemed to be most affected by entropic contributions and influenced by the dynamics of the end-tethered polymer layer at the surface of the nanoparticles. The results provided design guidelines to build more complex supracolloidal assemblies.

Finally, in **Section 4.4**, the site-selective functionalization of AuNT with polymer ligands was used to create amphiphilic building blocks to form colloidal monolayer film by self-assembly at the liquid-air interface. Close-packed monolayers were successfully obtained. However, the generation of more complex non-close-packed structures should rely on nanoparticles functionalized only with ligand or surfactant providing steric stabilization since the presence of surfactants providing stability from electrostatic repulsion led to aggregation when the ionic strength of the subphase was increased.

5.2 Perspectives

This thesis showed the promising possibilities of directional self-assembly and directed assembly of nanoparticles in functional supracolloidal functional materials. Furthermore, the results provided design rules for the control of supracolloidal assembly. However, the production of self-assembled structures that display a non-close-packed architecture remains challenging.

In **Section 4.1**, anisotropic patchy nanoparticles have been successfully integrated into polymer nanofibers by colloidal electrospinning and catalyzed different reactions. In the present case, gold hybrid nanoparticles were used, but there is an array of functional nanoparticles able to act as photocatalysts like conjugated polymer nanoparticles or hybrid nanoparticles, displaying better selectivity during the course of photocatalysis and could be integrated in a similar manner into nanofibrous membranes. Furthermore, some responsive polymers, like poly(N-isopropyl acrylamide) could be used to form the nanofibers. This would yield nanofibers able to adapt to environmental cues, and changes in the operating conditions could control the catalytic properties of the electrospun membranes. More generally, the immobilization of nanoparticles in polymer nanofibers is a convenient method to produce versatile functional materials incorporating the function of precisely tailored nanoparticles and could be beneficial in other fields, like coating or flexible electronics.

In **Section 4.2**, plasmonic supracolloidal assemblies were formed through host-guest chemistry between polymer functionalized gold nanorods. This strategy could be used to produce more complex structures by using different types of nanorods or different types of nanoparticles. The self-assembly of a mix of different nanoparticles leads to the formation of symmetry breaks in the resulting supracolloidal structure, and this can be harnessed in the design of more efficient optoelectronic devices,[295] used for instance, in sensing applications.

In **Section 4.3**, the effect of the solvent quality on the self-assembly of polymer-functionalized building blocks influenced the structure of the resulting supracolloidal assemblies. Not only the solvent quality, but also the length of the polymer corona and grafting density can influence the structure of colloidal building blocks and their directional of self-assembly. The physicochemical properties of the grafted polymer ligand strongly influence the formation of the supracolloidal structures, and the self-assembly behavior should be related more thoroughly to the conformation and dynamics of the polymer shell.

In **Section 4.4**, monolayer colloidal films were prepared with gold nanotriangles. However, the control over the structure of the resulting supracolloidal assemblies can be improved. To produce responsive non-close-packed 2D assemblies, it would be essential to replace the small ionic surfactants providing a fraction of the colloidal stability of the nanoparticles in water, or at the water interface, by short and bulky ligand providing more steric repulsion rather than electrostatic repulsion to make the array less susceptible to the increase of ionic strength. More generally, 2D and 3D structures produced through self-assembly of rather simple building blocks could open the door to the design of an array of new functional supracolloidal materials either due to the very localized NP-NP junctions or to the deliberate introduction of "empty" space tuning the dielectric properties of the supracolloidal assemblies.

6. Acknowledgment

7. Publications

8. Literature

1. Aguirre, C. I.; Reguera, E.; Stein, A., Tunable Colors in Opals and Inverse Opal Photonic Crystals. *Advanced Functional Materials* **2010,** *20* (16), 2565-2578.
2. Yan, Q.; Wang, L.; Zhao, X. S., Artificial Defect Engineering in Three-Dimensional Colloidal Photonic Crystals. *Advanced Functional Materials* **2007,** *17* (18), 3695-3706.
3. Dolina, J.; Dvořák, L.; Lederer, T.; Vacková, T.; Mikmeková, Š.; Šlouf, M.; Černík, M., Characterisation of morphological, antimicrobial and leaching properties of in situ prepared polyurethane nanofibres doped with silver behenate. *RSC Advances* **2016,** *6* (28), 23816-23826.
4. Someya, T.; Bao, Z.; Malliaras, G. G., The rise of plastic bioelectronics. *Nature* **2016,** *540* (7633), 379-385.
5. Burrows, N. D.; Vartanian, A. M.; Abadeer, N. S.; Grzincic, E. M.; Jacob, L. M.; Lin, W.; Li, J.; Dennison, J. M.; Hinman, J. G.; Murphy, C. J., Anisotropic Nanoparticles and Anisotropic Surface Chemistry. *The Journal of Physical Chemistry Letters* **2016,** *7* (4), 632-41.
6. Chen, D.; Hou, X.; Li, T.; Yin, L.; Fan, B.; Wang, H.; Li, X.; Xu, H.; Lu, H.; Zhang, R.; Sun, J., Effects of morphologies on acetone-sensing properties of tungsten trioxide nanocrystals. *Sensors and Actuators B: Chemical* **2011,** *153* (2), 373-381.
7. Jiang, R.; Li, B.; Fang, C.; Wang, J., Metal/Semiconductor Hybrid Nanostructures for Plasmon-Enhanced Applications. *Advanced Materials* **2014,** *26* (31), 5274-5309.
8. Hsu, S.-W.; On, K.; Tao, A. R., Localized Surface Plasmon Resonances of Anisotropic Semiconductor Nanocrystals. *Journal of the American Chemical Society* **2011,** *133* (47), 19072-19075.
9. Priecel, P.; Adekunle Salami, H.; Padilla, R. H.; Zhong, Z.; Lopez-Sanchez, J. A., Anisotropic gold nanoparticles: Preparation and applications in catalysis. *Chinese Journal of Catalysis* **2016,** *37* (10), 1619-1650.
10. Challener, W. A.; Peng, C.; Itagi, A. V.; Karns, D.; Peng, W.; Peng, Y.; Yang, X.; Zhu, X.; Gokemeijer, N. J.; Hsia, Y. T.; Ju, G.; Rottmayer, R. E.; Seigler, M. A.; Gage, E. C., Heat-assisted magnetic recording by a near-field transducer with efficient optical energy transfer. *Nature Photonics* **2009,** *3* (4), 220-224.

11. Correa-Duarte, M. A.; Perez-Juste, J.; Sanchez-Iglesias, A.; Giersig, M.; Liz-Marzan, L. M., Aligning Au nanorods by using carbon nanotubes as templates. *Angewandte Chemie International Edition in English* **2005,** *44* (28), 4375-8.

12. Wang, J.; Mbah, C. F.; Przybilla, T.; Apeleo Zubiri, B.; Spiecker, E.; Engel, M.; Vogel, N., Magic number colloidal clusters as minimum free energy structures. *Nature Communications* **2018,** *9* (1), 5259.

13. Wang, J.; Sultan, U.; Goerlitzer, E. S. A.; Mbah, C. F.; Engel, M.; Vogel, N., Structural Color of Colloidal Clusters as a Tool to Investigate Structure and Dynamics. *Advanced Functional Materials* **2019,** *30* (26).

14. Montanarella, F.; Geuchies, J. J.; Dasgupta, T.; Prins, P. T.; van Overbeek, C.; Dattani, R.; Baesjou, P.; Dijkstra, M.; Petukhov, A. V.; van Blaaderen, A.; Vanmaekelbergh, D., Crystallization of Nanocrystals in Spherical Confinement Probed by in Situ X-ray Scattering. *Nano Letters* **2018,** *18* (6), 3675-3681.

15. Li, P.; Li, Y.; Zhou, Z.-K.; Tang, S.; Yu, X.-F.; Xiao, S.; Wu, Z.; Xiao, Q.; Zhao, Y.; Wang, H.; Chu, P. K., Evaporative Self-Assembly of Gold Nanorods into Macroscopic 3D Plasmonic Superlattice Arrays. *Advanced Materials* **2016,** *28* (13), 2511-2517.

16. Rong, Y.; Song, L.; Si, P.; Zhang, L.; Lu, X.; Zhang, J.; Nie, Z.; Huang, Y.; Chen, T., Macroscopic Assembly of Gold Nanorods into Superstructures with Controllable Orientations by Anisotropic Affinity Interaction. *Langmuir* **2017,** *33* (48), 13867-13873.

17. Klinger, D.; Wang, C. X.; Connal, L. A.; Audus, D. J.; Jang, S. G.; Kraemer, S.; Killops, K. L.; Fredrickson, G. H.; Kramer, E. J.; Hawker, C. J., A facile synthesis of dynamic, shape-changing polymer particles. *Angewandte Chemie International Edition in English* **2014,** *53* (27), 7018-22.

18. Bobbi, E.; Sabagh, B.; Cryan, S.-A.; Wilson, J. A.; Heise, A., Anisotropic polymer nanoparticles with solvent and temperature dependent shape and size from triblock copolymers. *Polymer Chemistry* **2019,** *10* (25), 3436-3443.

19. Yang, S.-M.; Kim, S.-H.; Lim, J.-M.; Yi, G.-R., Synthesis and assembly of structured colloidal particles. *Journal of Materials Chemistry* **2008,** *18* (19).

20. P.Taylor, Ostwald ripening in emulsions. *Advances in Colloid and Interface Science* **1998,** *75* (2), 107-163.

21. Landfester, K., Miniemulsion Polymerization and the Structure of Polymer and Hybrid Nanoparticles. *Angewandte Chemie International Edition* **2009,** *48* (25), 4488-4507.

22. Fryd, M. M.; Mason, T. G., Time-Dependent Nanoemulsion Droplet Size Reduction By Evaporative Ripening. *The Journal of Physical Chemistry Letters* **2010,** *1* (23), 3349-3353.

23. Li, L.; Matsunaga, K.; Zhu, J.; Higuchi, T.; Yabu, H.; Shimomura, M.; Jinnai, H.; Hayward, R. C.; Russell, T. P., Solvent-Driven Evolution of Block Copolymer Morphology under 3D Confinement. *Macromolecules* **2010,** *43* (18), 7807-7812.

24. Ku, K. H.; Shin, J. M.; Yun, H.; Yi, G.-R.; Jang, S. G.; Kim, B. J., Multidimensional Design of Anisotropic Polymer Particles from Solvent-Evaporative Emulsion. *Advanced Functional Materials* **2018,** *28* (42).

25. Bates, S. J. a. F. S., On the Origins of Morphological Complexity in Block Copolymer Surfactants. *Science* **2003,** *300.*

26. Wooley, A. M. N. a. K. L., The Importance of Chemistry in Creating Well-Defined Nanoscopic Embedded Therapeutics: Devices Capable of the Dual Functions of Imaging and Therapy. *Accounts of Chemical Research* **2011,** *44* (10), 969-978.

27. Mai, Y.; Eisenberg, A., Self-assembly of block copolymers. *Chemical Society Reviews* **2012,** *41* (18), 5969-85.

28. Li, L.; Raghupathi, K.; Song, C.; Prasad, P.; Thayumanavan, S., Self-assembly of random copolymers. *Chemical Communications* **2014,** *50* (88), 13417-32.

29. Voets, I. K.; de Keizer, A.; de Waard, P.; Frederik, P. M.; Bomans, P. H.; Schmalz, H.; Walther, A.; King, S. M.; Leermakers, F. A.; Cohen Stuart, M. A., Double-faced micelles from water-soluble polymers. *Angewandte Chemie International Edition* **2006,** *45* (40), 6673-6.

30. Honggang Cui, Z. C., Sheng Zhong, Karen L. Wooley, Darrin J. Pochan, Block Copolymer Assembly via Kinetic Control. *Science* **2007,** *317* (5838), 647-650.

31. Groschel, A. H.; Walther, A.; Lobling, T. I.; Schmelz, J.; Hanisch, A.; Schmalz, H.; Muller, A. H., Facile, solution-based synthesis of soft, nanoscale Janus particles with tunable Janus balance. *Journal of the American Chemical Society* **2012,** *134* (33), 13850-60.

32. Walther, A.; Barner-Kowollik, C.; Müller, A. H. E., Mixed, Multicompartment, or Janus Micelles? A Systematic Study of Thermoresponsive Bis-Hydrophilic Block Terpolymers. *Langmuir* **2010,** *26* (14), 12237-12246.

33. Skrabania, K.; Berlepsch, H. v.; Böttcher, C.; Laschewsky, A., Synthesis of Ternary, Hydrophilic−Lipophilic−Fluorophilic Block Copolymers by Consecutive RAFT Polymerizations and Their Self-Assembly into Multicompartment Micelles. *Macromolecules* **2010,** *43* (1), 271-281.

34. Begoña Almería, W. D., Tarek M.Fahmy, Alessandro Gomez, Controlling the morphology of electrospray-generated PLGA microparticles for drug delivery. *Journal of Colloid and Interface Science* **2010,** *343* (1), 125-133.

35. Julie A. Champion, Y. K. K., and Samir Mitragotri, Making polymeric micro- and nanoparticles of complex shapes. *PANS* **2007,** *104* (29), 11901-11904.

36. Park, J. E.; Lee, Y.; Nam, J. M., Precisely Shaped, Uniformly Formed Gold Nanocubes with Ultrahigh Reproducibility in Single-Particle Scattering and Surface-Enhanced Raman Scattering. *Nano Letters* **2018,** *18* (10), 6475-6482.

37. Liebig, F.; Sarhan, R. M.; Sander, M.; Koopman, W.; Schuetz, R.; Bargheer, M.; Koetz, J., Deposition of Gold Nanotriangles in Large Scale Close-Packed Monolayers for X-ray-Based Temperature Calibration and SERS Monitoring of Plasmon-Driven Catalytic Reactions. *ACS Applied Materials & Interfaces* **2017,** *9* (23), 20247-20253.

38. Cai, Z.; Zhang, Y.; He, Z.; Jiang, L.-P.; Zhu, J.-J., NIR-Triggered Chemo-Photothermal Therapy by Thermosensitive Gold Nanostar@Mesoporous Silica@Liposome-Composited Drug Delivery Systems. *ACS Applied Bio Materials* **2020,** *3* (8), 5322-5330.

39. Bernasconi, G. D.; Butet, J.; Martin, O. J. F., Dynamics of Second-Harmonic Generation in a Plasmonic Silver Nanorod. *ACS Photonics* **2018,** *5* (8), 3246-3254.

40. Xiao, D.; Wu, Z.; Song, M.; Chun, J.; Schenter, G. K.; Li, D., Silver Nanocube and Nanobar Growth via Anisotropic Monomer Addition and Particle Attachment Processes. *Langmuir* **2018,** *34* (4), 1466-1472.

41. Mankin, M. N.; Mazumder, V.; Sun, S., One-Pot Synthesis of Pt Nanocubes and Nanopods via Burst Nucleation and Controlled Secondary Growth. *Chemistry of Materials* **2011,** *23* (2), 132-136.

42. Li, R.; Bian, K.; Wang, Y.; Xu, H.; Hollingsworth, J. A.; Hanrath, T.; Fang, J.; Wang, Z., An Obtuse Rhombohedral Superlattice Assembled by Pt Nanocubes. *Nano Letters* **2015,** *15* (9), 6254-6260.

43. Fang, C.; Bi, T.; Ding, Q.; Cui, Z.; Yu, N.; Xu, X.; Geng, B., High-Density Pd Nanorod Arrays on Au Nanocrystals for High-Performance Ethanol Electrooxidation. *ACS Applied Materials & Interfaces* **2019,** *11* (22), 20117-20124.

44. Lai, K. C.; Chen, M.; Williams, B.; Han, Y.; Tsung, C. K.; Huang, W.; Evans, J. W., Reshaping of Truncated Pd Nanocubes: Energetic and Kinetic Analysis Integrating Transmission Electron Microscopy with Atomistic-Level and Coarse-Grained Modeling. *ACS Nano* **2020,** *14* (7), 8551-8561.

45. Chen, L.; Ji, F.; Xu, Y.; He, L.; Mi, Y.; Bao, F.; Sun, B.; Zhang, X.; Zhang, Q., High-yield seedless synthesis of triangular gold nanoplates through oxidative etching. *Nano Letters* **2014,** *14* (12), 7201-6.

46. Ye, E.; Regulacio, M. D.; Zhang, S. Y.; Loh, X. J.; Han, M. Y., Anisotropically branched metal nanostructures. *Chemical Society Reviews* **2015,** *44* (17), 6001-17.

47. Leonardo Scarabelli, M. C.-P., Juan J. Giner-Casares, Judith Langer, and Luis M. Liz-Marzán, Monodisperse Gold Nanotriangles Size Control, Large-Scale Self-Assembly, and Performance in Surface-Enhanced Raman Scattering. *ACS Nano* **2014,** *8* (6), 5833-5842.

48. Straney, P. J.; Andolina, C. M.; Millstone, J. E., Seedless initiation as an efficient, sustainable route to anisotropic gold nanoparticles. *Langmuir* **2013,** *29* (13), 4396-403.

49. Umar, A.; Lee, J.; Dey, J.; Choi, S.-M., Seedless Synthesis of Monodisperse Cuboctahedral Gold Nanoparticles with Tunable Sizes. *Chemistry of Materials* **2016,** *28* (14), 4962-4970.

50. Lohse, S. E.; Burrows, N. D.; Scarabelli, L.; Liz-Marzán, L. M.; Murphy, C. J., Anisotropic Noble Metal Nanocrystal Growth: The Role of Halides. *Chemistry of Materials* **2013,** *26* (1), 34-43.

51. Sanchez-Iglesias, A.; Winckelmans, N.; Altantzis, T.; Bals, S.; Grzelczak, M.; Liz-Marzan, L. M., High-Yield Seeded Growth of Monodisperse Pentatwinned Gold Nanoparticles through Thermally Induced Seed Twinning. *Journal of the American Chemical Society* **2017,** *139* (1), 107-110.

52. Dreaden, E. C.; Alkilany, A. M.; Huang, X.; Murphy, C. J.; El-Sayed, M. A., The golden age: gold nanoparticles for biomedicine. *Chemical Society Reviews* **2012,** *41* (7), 2740-2779.

53. Vigderman, L.; Zubarev, E. R., High-Yield Synthesis of Gold Nanorods with Longitudinal SPR Peak Greater than 1200 nm Using Hydroquinone as a Reducing Agent. *Chemistry of Materials* **2013,** *25* (8), 1450-1457.

54. Murphy, T. K. S. a. C. J., Room Temperature, High-Yield Synthesis of Multiple Shapes of Gold Nanoparticles in Aqueous Solution. *Journal of the American Chemical Society* **2004,** *126*, 8648-8649.

55. Lohse, S. E.; Murphy, C. J., The Quest for Shape Control: A History of Gold Nanorod Synthesis. *Chemistry of Materials* **2013,** *25* (8), 1250-1261.

56. Catherine J. Murphy, T. K. S., Anand M. Gole, Christopher J. Orendorff, Jinxin Gao, Linfeng Gou, Simona E. Hunyadi, and Tan Li, Anisotropic Metal Nanoparticles Synthesis, Assembly, and Optical Applications. *The Journal of Physical Chemistry B* **2005,** *109*, 13857-13870.

57. Wafa Abidi, P. R. S., Yanick Guillet, Isabelle Lampre, Patricia Beaunier,; Brigitte Pansu, B. P., and Hynd Remita, One-Pot Radiolytic Synthesis of Gold Nanorods and Their Optical Properties. *The Journal of Physical Chemistry C* **2010,** *114*, 14794-14803.

58. Kinkhabwala, A.; Yu, Z.; Fan, S.; Avlasevich, Y.; Müllen, K.; Moerner, W. E., Large single-molecule fluorescence enhancements produced by a bowtie nanoantenna. *Nature Photonics* **2009,** *3* (11), 654-657.

59. Lohmuller, T.; Iversen, L.; Schmidt, M.; Rhodes, C.; Tu, H. L.; Lin, W. C.; Groves, J. T., Single molecule tracking on supported membranes with arrays of optical nanoantennas. *Nano Letters* **2012,** *12* (3), 1717-21.

60. Wang, G. Z. a. D., Fabrication of Heterogeneous Binary Arrays of Nanoparticles via Colloidal Lithography. *Journal of the American Chemical Society* **2008,** *130*, 5616-5617.

61. Malainou, A.; Tsougeni, K.; Ellinas, K.; Petrou, P. S.; Constantoudis, V.; Sarantopoulou, E.; Awsiuk, K.; Bernasik, A.; Budkowski, A.; Markou, A.; Panagiotopoulos, I.; Kakabakos, S. E.; Gogolides, E.; Tserepi, A., Plasma-assisted nanoscale protein patterning on Si substrates via colloidal lithography. *The Journal of Physical Chemistry A* **2013,** *117* (50), 13743-51.

62. Gangishetty, M. K.; Fontes, A. M.; Malta, M.; Kelly, T. L.; Scott, R. W. J., Improving the rates of Pd-catalyzed reactions by exciting the surface plasmons of AuPd bimetallic nanotriangles. *RSC Advances* **2017,** *7* (64), 40218-40226.

63. Yadav, H. O. S., Understanding the binary interactions of noble metal and semiconductor nanoparticles. *Soft Matter* **2020,** *16* (40), 9262-9272.

64. Bradley, M. J.; Read, C. G.; Schaak, R. E., Pt-Au Nanoparticle Heterodimers as Seeds for Pt-Au-Metal Sulfide Heterotrimers: Thermal Stability and Chemoselective Growth Characteristics. *Journal of Physical Chemistry C* **2015,** *119* (16), 8952-8959.

65. Feng-Ru Fan, D.-Y. L., Yuan-Fei Wu, Sai Duan, Zhao-Xiong Xie, Zhi-Yuan Jiang, and; Tian, Z.-Q., Epitaxial Growth of Heterogeneous Metal Nanocrystals From Gold Nano-octahedra to Palladium and Silver Nanocubes. *Journal of the American Chemical Society* **2008,** *130*, 6949-6951.

66. Chun-Hong Kuo, T.-E. H., and Michael H. Huang, Au Nanocrystal-Directed Growth of Au−Cu2O Core−Shell Heterostructures with Precise Morphological Control. *Journal of the American Chemical Society* **2009,** *131* (49), 17871-17878.

67. Wang, H.-J.; Yang, K.-H.; Hsu, S.-C.; Huang, M. H., Photothermal effects from Au–Cu2O core–shell nanocubes, octahedra, and nanobars with broad near-infrared absorption tunability. *Nanoscale* **2016,** *8* (2), 965-972.

68. Lou, Z.; Kim, S.; Fujitsuka, M.; Yang, X.; Li, B.; Majima, T., Anisotropic Ag2 S-Au Triangular Nanoprisms with Desired Configuration for Plasmonic Photocatalytic Hydrogen Generation in Visible/Near-Infrared Region. *Advanced Functional Materials* **2018,** *28* (13).

69. Choueiri, R. M.; Galati, E.; Therien-Aubin, H.; Klinkova, A.; Larin, E. M.; Querejeta-Fernandez, A.; Han, L.; Xin, H. L.; Gang, O.; Zhulina, E. B.; Rubinstein, M.; Kumacheva, E., Surface patterning of nanoparticles with polymer patches. *Nature* **2016,** *538* (7623), 79-83.

70. Schweizerhof, S.; Demco, D. E.; Mourran, A.; Fechete, R.; Moller, M., Diffusion of Gold Nanorods Functionalized with Thermoresponsive Polymer Brushes. *Langmuir* **2018,** *34* (27), 8031-8041.

71. Galati, E.; Tebbe, M.; Querejeta-Fernandez, A.; Xin, H. L.; Gang, O.; Zhulina, E. B.; Kumacheva, E., Shape-Specific Patterning of Polymer-Functionalized Nanoparticles. *ACS Nano* **2017,** *11* (5), 4995-5002.

72. K. K. Caswell, J. N. W., Uwe H. F. Bunz, and Catherine J. Murphy, Preferential End-to-End Assembly of Gold Nanorods by Biotin−Streptavidin Connectors. *Journal of the American Chemical Society* **2003,** *125*, 13914-13915.

73. Zhang, X.; Lv, L.; Ji, L.; Guo, G.; Liu, L.; Han, D.; Wang, B.; Tu, Y.; Hu, J.; Yang, D.; Dong, A., Self-Assembly of One-Dimensional Nanocrystal Superlattice Chains Mediated by Molecular Clusters. *Journal of the American Chemical Society* **2016,** *138* (10), 3290-3.

74. Cheng, Q.; Song, L.; Lin, H.; Yang, Y.; Huang, Y.; Su, F.; Chen, T., Free-Standing 2D Janus Gold Nanoparticles Monolayer Film with Tunable Bifacial Morphologies via the Asymmetric Growth at Air-Liquid Interface. *Langmuir* **2020,** *36* (1), 250-256.

75. Ye, X.; Qi, L., Two-dimensionally patterned nanostructures based on monolayer colloidal crystals: Controllable fabrication, assembly, and applications. *Nano Today* **2011,** *6* (6), 608-631.

76. Younan Xia, B. G., Yadong Yin, and Yu Lu, Monodispersed Colloidal Spheres Old Materials with New Applications. *Advanced Materials* **2000,** *12* (10), 693-713.

77. ANDREA R. TAO, J. H., and PEIDONG YANG, Langmuir−Blodgettry of Nanocrystals and Nanowires. *Accounts of Chemical Research* **2008,** *41* (12), 1662-1673.

78. Zhou, Y.; Zhou, X.; Park, D. J.; Torabi, K.; Brown, K. A.; Jones, M. R.; Zhang, C.; Schatz, G. C.; Mirkin, C. A., Shape-selective deposition and assembly of anisotropic nanoparticles. *Nano Letters* **2014,** *14* (4), 2157-61.

79. Colson, P.; Cloots, R.; Henrist, C., Experimental Design Applied to Spin Coating of 2D Colloidal Crystal Masks: A Relevant Method? *Langmuir* **2011,** *27* (21), 12800-12806.

80. Lu, X.; Huang, Y.; Liu, B.; Zhang, L.; Song, L.; Zhang, J.; Zhang, A.; Chen, T., Light-Controlled Shrinkage of Large-Area Gold Nanoparticle Monolayer Film for Tunable SERS Activity. *Chemistry of Materials* **2018,** *30* (6), 1989-1997.

81. Kalyanikutty, C. N. R. R. a. K. P., The Liquid–Liquid Interface as a Medium To Generate Nanocrystalline Films of Inorganic Materials. *Accounts of Chemical Research* **2008,** *41* (4), 489-499.

82. Park, S.; Hwang, H.; Kim, M.; Moon, J. H.; Kim, S. H., Colloidal assembly in droplets: structures and optical properties. *Nanoscale* **2020,** *12* (36), 18576-18594.

83. Henzie, J.; Grunwald, M.; Widmer-Cooper, A.; Geissler, P. L.; Yang, P., Self-assembly of uniform polyhedral silver nanocrystals into densest packings and exotic superlattices. *Nature Materials* **2011,** *11* (2), 131-7.

84. Lagzi, I.; Kowalczyk, B.; Wang, D.; Grzybowski, B. A., Nanoparticle oscillations and fronts. *Angewandte Chemie International Edition in English* **2010,** *49* (46), 8616-9.

85. Srivastava, S. S., A.; Critchley, K.; Kim, K. S.; Podsiadlo, P.; Sun, K.; Lee, J.; Xu, C. L.; Lilly, G. D.; Glotzer, S. C.; Kotov, N, Light-Controlled Self-Assembly of

Semiconductor Nanoparticles into Twisted Ribbons. *Science* **2010,** *327* (5971), 1355-1359.

86. Goubet, N.; Portales, H.; Yan, C.; Arfaoui, I.; Albouy, P. A.; Mermet, A.; Pileni, M. P., Simultaneous growths of gold colloidal crystals. *Journal of the American Chemical Society* **2012,** *134* (8), 3714-9.

87. Nykypanchuk, D.; Maye, M. M.; van der Lelie, D.; Gang, O., DNA-guided crystallization of colloidal nanoparticles. *Nature* **2008,** *451* (7178), 549-52.

88. Zhang, Q.; Serpe, M. J.; Mugo, S. M., Stimuli Responsive Polymer-Based 3D Optical Crystals for Sensing. *Polymers* **2017,** *9* (11).

89. Chang, H. K.; Chang, G. T.; Thokchom, A. K.; Kim, T.; Park, J., Ultra-fast responsive colloidal-polymer composite-based volatile organic compounds (VOC) sensor using nanoscale easy tear process. *Scientific Reports* **2018,** *8*.

90. Marek Grzelczak, J. V., §, Eric M. Furst, and Luis M. Liz-Marzan, Directed Self-Assembly of Nanoparticles. *ACS Nano* **2010,** *4* (7), 3591–3605.

91. Lan, X.; Su, Z.; Zhou, Y.; Meyer, T.; Ke, Y.; Wang, Q.; Chiu, W.; Liu, N.; Zou, S.; Yan, H.; Liu, Y., Programmable Supra-Assembly of a DNA Surface Adapter for Tunable Chiral Directional Self-Assembly of Gold Nanorods. *Angewandte Chemie International Edition in English* **2017,** *56* (46), 14632-14636.

92. Lv, J.; Hou, K.; Ding, D.; Wang, D.; Han, B.; Gao, X.; Zhao, M.; Shi, L.; Guo, J.; Zheng, Y.; Zhang, X.; Lu, C.; Huang, L.; Huang, W.; Tang, Z., Gold Nanowire Chiral Ultrathin Films with Ultrastrong and Broadband Optical Activity. *Angewandte Chemie International Edition in English* **2017,** *56* (18), 5055-5060.

93. Barron, L. D., Chirality and magnetism shake hands. *Nature Materials* **2008,** *7*, 691-692.

94. Wu, X.; Xu, L.; Liu, L.; Ma, W.; Yin, H.; Kuang, H.; Wang, L.; Xu, C.; Kotov, N. A., Unexpected chirality of nanoparticle dimers and ultrasensitive chiroplasmonic bioanalysis. *Journal of the American Chemical Society* **2013,** *135* (49), 18629-36.

95. Hanske, C.; Tebbe, M.; Kuttner, C.; Bieber, V.; Tsukruk, V. V.; Chanana, M.; Konig, T. A.; Fery, A., Strongly coupled plasmonic modes on macroscopic areas via template-assisted colloidal self-assembly. *Nano Letters* **2014,** *14* (12), 6863-71.

96. Yuan Zhang, Q. L., Haridas Mundoor, Ye Yuan, and Ivan I. Smalyukh, Metal Nanoparticle Dispersion, Alignment, and Assembly in Nematic Liquid Crystals for Applications in Switchable Plasmonic Color Filters and E-Polarizers. *ACS Nano* **2015,** *9* (3), 3097-3108.

97. Julia J. Chiu, B. J. K., Edward J. Kramer, and David J. Pine, Control of Nanoparticle Location in Block Copolymers. *Journal of the American Chemical Society* **2005,** *127* (14), 5036-5037.

98. Zhang, C. L.; Lv, K. P.; Cong, H. P.; Yu, S. H., Controlled assemblies of gold nanorods in PVA nanofiber matrix as flexible free-standing SERS substrates by electrospinning. *Small* **2012,** *8* (5), 647-53.

99. Ko, F.; Gogotsi, Y.; Ali, A.; Naguib, N.; Ye, H.; Yang, G. L.; Li, C.; Willis, P., Electrospinning of Continuous Carbon Nanotube-Filled Nanofiber Yarns. *Advanced Materials* **2003,** *15* (14), 1161-1165.

100. Xue, J.; Xie, J.; Liu, W.; Xia, Y., Electrospun Nanofibers: New Concepts, Materials, and Applications. *Accounts of Chemical Research* **2017,** *50* (8), 1976-1987.

101. Jiang, S.; Lv, L. P.; Landfester, K.; Crespy, D., Nanocontainers in and onto Nanofibers. *Accounts of Chemical Research* **2016,** *49* (5), 816-23.

102. Zhang, C. L.; Yu, S. H., Nanoparticles meet electrospinning: recent advances and future prospects. *Chemical Society Reviews* **2014,** *43* (13), 4423-48.

103. Dian He, B. H., Qiao-Feng Yao, Kan Wang, and Shu-Hong Yu, Large-Scale Synthesis of Flexible FreeStanding SERS Substrates with High. *ACS Nano* **2009,** *3* (12), 3993-4002.

104. Collins, K. A.; Zhong, X.; Song, P.; Little, N. R.; Ward, M. D.; Lee, S. S., Electric-Field-Induced Reversible Phase Transitions in Two-Dimensional Colloidal Crystals. *Langmuir* **2015,** *31* (38), 10411-7.

105. Dziomkina, N. V.; Hempenius, M. A.; Vancso, G. J., Symmetry Control of Polymer Colloidal Monolayers and Crystals by Electrophoretic Deposition on Patterned Surfaces. *Advanced Materials* **2005,** *17* (2), 237-240.

106. Tang, Z.; Kotov, N. A., One-Dimensional Assemblies of Nanoparticles: Preparation, Properties, and Promise. *Advanced Materials* **2005,** *17* (8), 951-962.

107. Chen, L.; Su, B.; Jiang, L., Recent advances in one-dimensional assembly of nanoparticles. *Chemical Society Reviews* **2019,** *48* (1), 8-21.

108. Elacqua, E.; Zheng, X.; Shillingford, C.; Liu, M.; Weck, M., Molecular Recognition in the Colloidal World. *Accounts of Chemical Research* **2017,** *50* (11), 2756-2766.

109. Wang, Y.; Hollingsworth, A. D.; Yang, S. K.; Patel, S.; Pine, D. J.; Weck, M., Patchy particle self-assembly via metal coordination. *Journal of the American Chemical Society* **2013,** *135* (38), 14064-7.

110. Lan, Y.; Wu, Y.; Karas, A.; Scherman, O. A., Photoresponsive hybrid raspberry-like colloids based on cucurbit[8]uril host-guest interactions. *Angewandte Chemie International Edition in English* **2014,** *53* (8), 2166-9.

111. de Feijter, I.; Albertazzi, L.; Palmans, A. R.; Voets, I. K., Stimuli-responsive colloidal assembly driven by surface-grafted supramolecular moieties. *Langmuir* **2015,** *31* (1), 57-64.

112. Zheng, X.; Wang, Y.; Wang, Y.; Pine, D. J.; Weck, M., Thermal Regulation of Colloidal Materials Architecture through Orthogonal Functionalizable Patchy Particles. *Chemistry of Materials* **2016,** *28* (11), 3984-3989.

113. Choueiri, R. M.; Galati, E.; Klinkova, A.; Therien-Aubin, H.; Kumacheva, E., Linear assembly of patchy and non-patchy nanoparticles. *Faraday Discuss* **2016,** *191*, 189-204.

114. Liu, K.; Lukach, A.; Sugikawa, K.; Chung, S.; Vickery, J.; Therien-Aubin, H.; Yang, B.; Rubinstein, M.; Kumacheva, E., Copolymerization of metal nanoparticles: a route to colloidal plasmonic copolymers. *Angewandte Chemie International Edition in English* **2014,** *53* (10), 2648-53.

115. Ding, H.; Liu, C.; Gu, H.; Zhao, Y.; Wang, B.; Gu, Z., Responsive Colloidal Crystal for Spectrometer Grating. *ACS Photonics* **2014,** *1* (2), 121-126.

116. You, B.; Wen, N.; Shi, L.; Wu, L.; Zi, J., Facile fabrication of a three-dimensional colloidal crystal film with large-area and robust mechanical properties. *Journal of Materials Chemistry* **2009,** *19* (22).

117. Maldovan, M.; Ullal, C. K.; Carter, W. C.; Thomas, E. L., Exploring for 3D photonic bandgap structures in the 11 f.c.c. space groups. *Nature Materials* **2003,** *2* (10), 664-7.

118. Garcia-Adeva, A., Band gap atlas for photonic crystals having the symmetry of the kagomé and pyrochlore lattices. *New Journal of Physics* **2006,** *8* (6), 86-86.

119. He, M.; Gales, J. P.; Ducrot, E.; Gong, Z.; Yi, G. R.; Sacanna, S.; Pine, D. J., Colloidal diamond. *Nature* **2020,** *585* (7826), 524-529.

120. John, S., Strong localization of photons in certain disordered dielectric superlattices. *Physical Review Letters* **1987,** *58* (23), 2486-2489.

121. Gur, D.; Palmer, B. A.; Weiner, S.; Addadi, L., Light Manipulation by Guanine Crystals in Organisms: Biogenic Scatterers, Mirrors, Multilayer Reflectors and Photonic Crystals. *Advanced Functional Materials* **2017,** *27* (6).

122. Dumanli, A. G.; Savin, T., Recent advances in the biomimicry of structural colours. *Chem Soc Rev* **2016,** *45* (24), 6698-6724.

123. von Freymann, G.; Kitaev, V.; Lotsch, B. V.; Ozin, G. A., Bottom-up assembly of photonic crystals. *Chemical Society Reviews* **2013,** *42* (7), 2528-54.

124. Cho, Y.; Lee, S. Y.; Ellerthorpe, L.; Feng, G.; Lin, G.; Wu, G.; Yin, J.; Yang, S., Elastoplastic Inverse Opals as Power-Free Mechanochromic Sensors for Force Recording. *Advanced Functional Materials* **2015,** *25* (38), 6041-6049.

125. Zhao, Y.; Zhao, X.; Tang, B.; Xu, W.; Li, J.; Hu, J.; Gu, Z., Quantum-Dot-Tagged Bioresponsive Hydrogel Suspension Array for Multiplex Label-Free DNA Detection. *Advanced Functional Materials* **2010,** *20* (6), 976-982.

126. Yang, D.; Ye, S.; Ge, J., Solvent wrapped metastable colloidal crystals: highly mutable colloidal assemblies sensitive to weak external disturbance. *Journal of the American Chemical Society* **2013,** *135* (49), 18370-6.

127. Burgess, I. B.; Mishchenko, L.; Hatton, B. D.; Kolle, M.; Loncar, M.; Aizenberg, J., Encoding complex wettability patterns in chemically functionalized 3D photonic crystals. *Journal of the American Chemical Society* **2011,** *133* (32), 12430-2.

128. Hu, M.; Korschelt, K.; Daniel, P.; Landfester, K.; Tremel, W.; Bannwarth, M. B., Fibrous Nanozyme Dressings with Catalase-Like Activity for H2O2 Reduction To Promote Wound Healing. *ACS Applied Materials & Interfaces* **2017,** *9* (43), 38024-38031.

129. Tang, F.; Li, L.; Chen, D., Mesoporous silica nanoparticles: synthesis, biocompatibility and drug delivery. *Advanced Materials* **2012,** *24* (12), 1504-34.

130. Ulbrich, K.; Hola, K.; Subr, V.; Bakandritsos, A.; Tucek, J.; Zboril, R., Targeted Drug Delivery with Polymers and Magnetic Nanoparticles: Covalent and Noncovalent Approaches, Release Control, and Clinical Studies. *Chemical Reviews* **2016,** *116* (9), 5338-431.

131. Lu, Z. R.; Qiao, P., Drug Delivery in Cancer Therapy, Quo Vadis? *Molecular Pharmaceutics* **2018,** *15* (9), 3603-3616.

132. Yang, K.; Zhang, S.; He, J.; Nie, Z., Polymers and inorganic nanoparticles: A winning combination towards assembled nanostructures for cancer imaging and therapy. *Nano Today* **2021,** *36.*

133. Yang, K.; Liu, Y.; Liu, Y.; Zhang, Q.; Kong, C.; Yi, C.; Zhou, Z.; Wang, Z.; Zhang, G.; Zhang, Y.; Khashab, N. M.; Chen, X.; Nie, Z., Cooperative Assembly of Magneto-Nanovesicles with Tunable Wall Thickness and Permeability for MRI-

Guided Drug Delivery. *Journal of the American Chemical Society* **2018,** *140* (13), 4666-4677.

134. A. Mihi, M. E. C., J. A. Anta, and H. Mı´guez, Spectral Response of Opal-Based Dye-Sensitized Solar Cells. *The Journal of Physical Chemistry C* **2008,** *112*, 13-17.

135. Haugan, E.; Granlund, H.; Gjessing, J.; Marstein, E. S., Colloidal Crystals as Templates for Light Harvesting Structures in Solar Cells. *Energy Procedia* **2011,** *10*, 292-296.

136. Bosco, J. P.; Sasaki, K.; Sadakane, M.; Ueda, W.; Chen, J. G., Synthesis and Characterization of Three-Dimensionally Ordered Macroporous (3DOM) Tungsten Carbide: Application to Direct Methanol Fuel Cells†. *Chemistry of Materials* **2010,** *22* (3), 966-973.

137. Zhang, Y.; Wang, J.; Zhao, Y.; Zhai, J.; Jiang, L.; Song, Y.; Zhu, D., Photonic crystal concentrator for efficient output of dye-sensitized solar cells. *Journal of Materials Chemistry* **2008,** *18* (23).

138. Graff, R. W.; Wang, X.; Gao, H., Exploring Self-Condensing Vinyl Polymerization of Inimers in Microemulsion To Regulate the Structures of Hyperbranched Polymers. *Macromolecules* **2015,** *48* (7), 2118-2126.

139. El-Sayed, B. N. a. M. A., Preparation and Growth Mechanism of Gold Nanorods (NRs) Using Seed-Mediated Growth Method. *Chemistry of Materials* **2003,** *15* (10), 1957-1962.

140. Park, K.; Koerner, H.; Vaia, R. A., Depletion-induced shape and size selection of gold nanoparticles. *Nano Letters* **2010,** *10* (4), 1433-9.

141. Kim, Y. G.; Wagner, M.; Therien-Aubin, H., Dynamics of Soft and Hairy Polymer Nanoparticles in a Suspension by NMR Relaxation. *Macromolecules* **2020,** *53* (3), 844-851.

142. Stéphane Reculusa, C. M., Elodie Bourgeat-Lami, Etienne Duguet, Serge Ravaine, Synthesis of Daisy-Shaped and Multipod-like Silica/Polystyrene Nanocomposites. *Nano Letters* **2004,** *4* (9), 1677-1682.

143. Riedinger, A.; Pernia Leal, M.; Deka, S. R.; George, C.; Franchini, I. R.; Falqui, A.; Cingolani, R.; Pellegrino, T., "Nanohybrids" based on pH-responsive hydrogels and inorganic nanoparticles for drug delivery and sensor applications. *Nano Letters* **2011,** *11* (8), 3136-41.

144. Yang, X.; Wang, D., Photocatalysis: From Fundamental Principles to Materials and Applications. *ACS Applied Energy Materials* **2018,** *1* (12), 6657-6693.

145. Prier, C. K.; Rankic, D. A.; MacMillan, D. W., Visible light photoredox catalysis with transition metal complexes: applications in organic synthesis. *Chemical Reviews* **2013,** *113* (7), 5322-63.

146. Ravelli, D.; Dondi, D.; Fagnoni, M.; Albini, A., Photocatalysis. A multi-faceted concept for green chemistry. *Chemical Society Reviews* **2009,** *38* (7), 1999-2011.

147. Shaik, F.; Peer, I.; Jain, P. K.; Amirav, L., Plasmon-Enhanced Multicarrier Photocatalysis. *Nano Letters* **2018,** *18* (7), 4370-4376.

148. Mubeen, S.; Lee, J.; Liu, D.; Stucky, G. D.; Moskovits, M., Panchromatic photoproduction of H2 with surface plasmons. *Nano Letters* **2015,** *15* (3), 2132-6.

149. Kang, H.; Buchman, J. T.; Rodriguez, R. S.; Ring, H. L.; He, J.; Bantz, K. C.; Haynes, C. L., Stabilization of Silver and Gold Nanoparticles: Preservation and Improvement of Plasmonic Functionalities. *Chemical Reviews* **2019,** *119* (1), 664-699.

150. Gellé, A.; Jin, T.; de la Garza, L.; Price, G. D.; Besteiro, L. V.; Moores, A., Applications of Plasmon-Enhanced Nanocatalysis to Organic Transformations. *Chemical Reviews* **2020,** *120* (2), 986-1041.

151. Linic, S.; Aslam, U.; Boerigter, C.; Morabito, M., Photochemical transformations on plasmonic metal nanoparticles. *Nature Materials* **2015,** *14* (6), 567-576.

152. Zhang, C.; Kong, T.; Fu, Z.; Zhang, Z.; Zheng, H., Hot electron and thermal effects in plasmonic catalysis of nanocrystal transformation. *Nanoscale* **2020,** *12* (16), 8768-8774.

153. Zhang, Y.; He, S.; Guo, W.; Hu, Y.; Huang, J.; Mulcahy, J. R.; Wei, W. D., Surface-Plasmon-Driven Hot Electron Photochemistry. *Chemical Reviews* **2018,** *118* (6), 2927-2954.

154. Mao, Z.; Vang, H.; Garcia, A.; Tohti, A.; Stokes, B. J.; Nguyen, S. C., Carrier Diffusion—The Main Contribution to Size-Dependent Photocatalytic Activity of Colloidal Gold Nanoparticles. *ACS Catalysis* **2019,** *9* (5), 4211-4217.

155. Hou, W.; Cronin, S. B., A Review of Surface Plasmon Resonance-Enhanced Photocatalysis. *Advanced Functional Materials* **2013,** *23* (13), 1612-1619.

156. Fang, C.; Jia, H.; Chang, S.; Ruan, Q.; Wang, P.; Chen, T.; Wang, J., (Gold core)/(titania shell) nanostructures for plasmon-enhanced photon harvesting and

generation of reactive oxygen species. *Energy & Environmental Science* **2014,** *7* (10), 3431-3438.

157. Wu, B.; Liu, D.; Mubeen, S.; Chuong, T. T.; Moskovits, M.; Stucky, G. D., Anisotropic Growth of TiO2 onto Gold Nanorods for Plasmon-Enhanced Hydrogen Production from Water Reduction. *Journal of the American Chemical Society* **2016,** *138* (4), 1114-7.

158. Liu, X.; Iocozzia, J.; Wang, Y.; Cui, X.; Chen, Y.; Zhao, S.; Li, Z.; Lin, Z., Noble metal–metal oxide nanohybrids with tailored nanostructures for efficient solar energy conversion, photocatalysis and environmental remediation. *Energy & Environmental Science* **2017,** *10* (2), 402-434.

159. Waiskopf, N.; Ben-Shahar, Y.; Banin, U., Photocatalytic Hybrid Semiconductor–Metal Nanoparticles; from Synergistic Properties to Emerging Applications. *Advanced Materials* **2018,** *30* (41), 1706697.

160. Mandal, S.; Ananthakrishnan, R., Double Effects of Interfacial Ag Nanoparticles in a ZnO Multipod@Ag@Bi2S3 Z-Scheme Photocatalytic Redox System: Concurrent Tuning and Improving Charge-Transfer Efficiency. *Inorganic Chemistry* **2020,** *59* (11), 7681-7699.

161. Liu, M.; Wei, S.; Shahi, S.; Jaiswal, H. N.; Paletti, P.; Fathipour, S.; Remskar, M.; Jiao, J.; Hwang, W.; Yao, F.; Li, H., Enhanced carrier transport by transition metal doping in WS2 field effect transistors. *Nanoscale* **2020,** *12* (33), 17253-17264.

162. Wi, D. H.; Park, S. Y.; Lee, S.; Sung, J.; Hong, J. W.; Han, S. W., Metal–semiconductor ternary hybrids for efficient visible-light photocatalytic hydrogen evolution. *Journal of Materials Chemistry A* **2018,** *6* (27), 13225-13235.

163. Montini, T.; Melchionna, M.; Monai, M.; Fornasiero, P., Fundamentals and Catalytic Applications of CeO2-Based Materials. *Chemical Reviews* **2016,** *116* (10), 5987-6041.

164. Rodriguez, J. A.; Si, R.; Evans, J.; Xu, W.; Hanson, J. C.; Tao, J.; Zhu, Y., Active gold-ceria and gold-ceria/titania catalysts for CO oxidation: From single-crystal model catalysts to powder catalysts. *Catalysis Today* **2015,** *240*, 229-235.

165. Li, B.; Gu, T.; Ming, T.; Wang, J.; Wang, P.; Wang, J.; Yu, J. C., (Gold Core)@(Ceria Shell) Nanostructures for Plasmon-Enhanced Catalytic Reactions under Visible Light. *ACS Nano* **2014,** *8* (8), 8152-8162.

166. Pan, J.; Zhang, L.; Zhang, S.; Shi, Z.; Wang, X.; Song, S.; Zhang, H., Half-Encapsulated Au Nanorods@CeO2 Core@Shell Nanostructures for Near-Infrared Plasmon-Enhanced Catalysis. *ACS Applied Nano Materials* **2019,** *2* (3), 1516-1524.

167. Jia, H.; Du, A.; Zhang, H.; Yang, J.; Jiang, R.; Wang, J.; Zhang, C. Y., Site-Selective Growth of Crystalline Ceria with Oxygen Vacancies on Gold Nanocrystals for Near-Infrared Nitrogen Photofixation. *Journal of the American Chemical Society* **2019,** *141* (13), 5083-5086.

168. Li, K.; de Rancourt de Mimérand, Y.; Jin, X.; Yi, J.; Guo, J., Metal Oxide (ZnO and TiO_2) and Fe-Based Metal–Organic-Framework Nanoparticles on 3D-Printed Fractal Polymer Surfaces for Photocatalytic Degradation of Organic Pollutants. *ACS Applied Nano Materials* **2020,** *3* (3), 2830-2845.

169. Mehta, J. P.; Tian, T.; Zeng, Z.; Divitini, G.; Connolly, B. M.; Midgley, P. A.; Tan, J.-C.; Fairen-Jimenez, D.; Wheatley, A. E. H., Sol–Gel Synthesis of Robust Metal–Organic Frameworks for Nanoparticle Encapsulation. *Advanced Functional Materials* **2018,** *28* (8), 1705588.

170. Yar, A.; Haspulat, B.; Üstün, T.; Eskizeybek, V.; Avcı, A.; Kamış, H.; Achour, S., Electrospun TiO2/ZnO/PAN hybrid nanofiber membranes with efficient photocatalytic activity. *RSC Advances* **2017,** *7* (47), 29806-29814.

171. Horzum, N.; Muñoz-Espí, R.; Glasser, G.; Demir, M. M.; Landfester, K.; Crespy, D., Hierarchically Structured Metal Oxide/Silica Nanofibers by Colloid Electrospinning. *ACS Applied Materials & Interfaces* **2012,** *4* (11), 6338-6345.

172. Ranjith, K. S.; Manivel, P.; Rajendrakumar, R. T.; Uyar, T., Multifunctional ZnO nanorod-reduced graphene oxide hybrids nanocomposites for effective water remediation: Effective sunlight driven degradation of organic dyes and rapid heavy metal adsorption. *Chemical Engineering Journal* **2017,** *325*, 588-600.

173. Yang, G.; Li, X.; He, Y.; Ma, J.; Ni, G.; Zhou, S., From nano to micro to macro: Electrospun hierarchically structured polymeric fibers for biomedical applications. *Progress in Polymer Science* **2018,** *81*, 80-113.

174. Xu, J.; Liu, C.; Hsu, P. C.; Liu, K.; Zhang, R.; Liu, Y.; Cui, Y., Roll-to-Roll Transfer of Electrospun Nanofiber Film for High-Efficiency Transparent Air Filter. *Nano Letters* **2016,** *16* (2), 1270-5.

175. Xue, J.; Wu, T.; Dai, Y.; Xia, Y., Electrospinning and Electrospun Nanofibers: Methods, Materials, and Applications. *Chemical Reviews* **2019,** *119* (8), 5298-5415.

176. Lv, D.; Wang, R.; Tang, G.; Mou, Z.; Lei, J.; Han, J.; De Smedt, S.; Xiong, R.; Huang, C., Ecofriendly Electrospun Membranes Loaded with Visible-Light-Responding Nanoparticles for Multifunctional Usages: Highly Efficient Air Filtration, Dye Scavenging, and Bactericidal Activity. *ACS Applied Materials & Interfaces* **2019,** *11* (13), 12880-12889.

177. Prabu, G. T. V.; Dhurai, B., A Novel Profiled Multi-Pin Electrospinning System for Nanofiber Production and Encapsulation of Nanoparticles into Nanofibers. *Scientific Reports* **2020,** *10* (1), 4302.

178. Jia, S.; Tang, D.; Zhou, Y.; Du, Y.; Peng, J.; Sun, Z.; Yang, X., Polydopamine Microsphere-Incorporated Electrospun Fibers as Novel Adsorbents for Dual-Responsive Adsorption of Methylene Blue. *ACS Applied Materials & Interfaces* **2020,** *12* (44), 49723-49736.

179. Morselli, D.; Campagnolo, L.; Prato, M.; Papadopoulou, E. L.; Scarpellini, A.; Athanassiou, A.; Fragouli, D., Ceria/Gold Nanoparticles in Situ Synthesized on Polymeric Membranes with Enhanced Photocatalytic and Radical Scavenging Activity. *ACS Applied Nano Materials* **2018,** *1* (10), 5601-5611.

180. Hu, M.; Korschelt, K.; Viel, M.; Wiesmann, N.; Kappl, M.; Brieger, J.; Landfester, K.; Therien-Aubin, H.; Tremel, W., Nanozymes in Nanofibrous Mats with Haloperoxidase-like Activity To Combat Biofouling. *ACS Applied Materials & Interfaces* **2018,** *10* (51), 44722-44730.

181. Chen, H. J.; Kou, X. S.; Yang, Z.; Ni, W. H.; Wang, J. F., Shape- and size-dependent refractive index sensitivity of gold nanoparticles. *Langmuir* **2008,** *24* (10), 5233-5237.

182. Liu, L. C.; Corma, A., Metal Catalysts for Heterogeneous Catalysis: From Single Atoms to Nanoclusters and Nanoparticles. *Chemical Reviews* **2018,** *118* (10), 4981-5079.

183. Tesema, T. E.; Kafle, B.; Habteyes, T. G., Plasmon-Driven Reaction Mechanisms: Hot Electron Transfer versus Plasmon-Pumped Adsorbate Excitation. *The Journal of Physical Chemistry C* **2019,** *123* (14), 8469-8483.

184. Serra, A.; Artal, R.; Pozo, M.; Garcia-Amoros, J.; Gomez, E., Simple Environmentally-Friendly Reduction of 4-Nitrophenol. *Catalysts* **2020,** *10* (4).

185. He, X. Y.; Tian, F.; Chang, J. F.; Bai, X. Q.; Yuan, C. Q.; Wang, C.; Neville, A., Haloperoxidase Mimicry by CeO2-x Nanorods of Different Aspect Ratios for

Antibacterial Performance. *ACS Sustainable Chemistry & Engineering* **2020,** *8* (17), 6744-6752.

186. Larowska, D.; O'Brien, J. M.; Senge, M. O.; Burdzinski, G.; Marciniak, B.; Lewandowska-Andralojc, A., Graphene Oxide Functionalized with Cationic Porphyrins as Materials for the Photodegradation of Rhodamine B. *The Journal of Physical Chemistry C* **2020,** *124* (29), 15769-15780.

187. Santhosh, C.; Velmurugan, V.; Jacob, G.; Jeong, S. K.; Grace, A. N.; Bhatnagar, A., Role of nanomaterials in water treatment applications: A review. *Chemical Engineering Journal* **2016,** *306*, 1116-1137.

188. Rojas, S.; Horcajada, P., Metal–Organic Frameworks for the Removal of Emerging Organic Contaminants in Water. *Chemical Reviews* **2020,** *120* (16), 8378-8415.

189. Wang, Z. L.; Mohamed, M. B.; Link, S.; El-Sayed, M. A., Crystallographic facets and shapes of gold nanorods of different aspect ratios. *Surface Science* **1999,** *440* (1-2), L809-L814.

190. Wang, Z. L., Transmission Electron Microscopy of Shape-Controlled Nanocrystals and Their Assemblies. *The Journal of Physical Chemistry B* **2000,** *104* (6), 1153-1175.

191. Xu, R.; Wang, D.; Zhang, J.; Li, Y., Shape-dependent catalytic activity of silver nanoparticles for the oxidation of styrene. *Chemistry: An Asian Journal* **2006,** *1* (6), 888-93.

192. Herves, P.; Perez-Lorenzo, M.; Liz-Marzan, L. M.; Dzubiella, J.; Lu, Y.; Ballauff, M., Catalysis by metallic nanoparticles in aqueous solution: model reactions. *Chemical Society Reviews* **2012,** *41* (17), 5577-87.

193. Mendoza-Huizar, L. H.; García Rodríguez, D. E.; Rios-Reyes, C. H.; Alatorre-Ordaz, A., Theoretical quantum study about the adsorption of BH4- onto X(100) where (X = Cu, Ag and Au). *Journal of the Mexican Chemical Society* **2012,** *56* (3), 302-310.

194. Rostamikia, G.; Patel, R. J.; Merino-Jimenez, I.; Hickner, M.; Janik, M. J., Electrocatalyst Design for Direct Borohydride Oxidation Guided by First Principles. *The Journal of Physical Chemistry C* **2017,** *121* (5), 2872-2881.

195. Roskov, K. E.; Kozek, K. A.; Wu, W. C.; Chhetri, R. K.; Oldenburg, A. L.; Spontak, R. J.; Tracy, J. B., Long-range alignment of gold nanorods in electrospun polymer nano/microfibers. *Langmuir* **2011,** *27* (23), 13965-9.

196. Claridge, S. A.; Castleman, A. W.; Khanna, S. N.; Murray, C. B.; Sen, A.; Weiss, P. S., Cluster-Assembled Materials. *ACS Nano* **2009,** *3* (2), 244-255.

197. Nie, Z. H.; Petukhova, A.; Kumacheva, E., Properties and emerging applications of self-assembled structures made from inorganic nanoparticles. *Nature Nanotechnology* **2010,** *5* (1), 15-25.

198. Mann, S., Self-assembly and transformation of hybrid nano-objects and nanostructures under equilibrium and non-equilibrium conditions. *Nature Materials* **2009,** *8* (10), 781-792.

199. Huang, Y.; Ma, L. W.; Hou, M. J.; Li, J. H.; Xie, Z.; Zhang, Z. J., Hybridized plasmon modes and near-field enhancement of metallic nanoparticle-dimer on a mirror. *Scientific Reports* **2016,** *6*.

200. Moskovits, M., Surface-enhanced Raman spectroscopy: a brief retrospective. *Journal of Raman Spectroscopy* **2005,** *36* (6-7), 485-496.

201. Li, J. F.; Li, C. Y.; Aroca, R. F., Plasmon-enhanced fluorescence spectroscopy. *Chemical Society Reviews* **2017,** *46* (13), 3962-3979.

202. Slaughter, L. S.; Willingham, B. A.; Chang, W. S.; Chester, M. H.; Ogden, N.; Link, S., Toward Plasmonic Polymers. *Nano Letters* **2012,** *12* (8), 3967-3972.

203. Duan, X. X.; Park, M. H.; Zhao, Y. P.; Berenschot, E.; Wang, Z. Y.; Reinhoudt, D. N.; Rotello, V. M.; Huskens, J., Metal Nanoparticle Wires Formed by an Integrated Nanomolding-Chemical Assembly Process: Fabrication and Properties. *ACS Nano* **2010,** *4* (12), 7660-7666.

204. Guerrero-Martinez, A.; Grzelczak, M.; Liz-Marzan, L. M., Molecular Thinking for Nanoplasmonic Design. *ACS Nano* **2012,** *6* (5), 3655-3662.

205. Gao, Y.; Tang, Z. Y., Design and Application of Inorganic Nanoparticle Superstructures: Current Status and Future challenges. *Small* **2011,** *7* (15), 2133-2146.

206. De Greef, T. F. A.; Smulders, M. M. J.; Wolffs, M.; Schenning, A. P. H. J.; Sijbesma, R. P.; Meijer, E. W., Supramolecular Polymerization. *Chemical Reviews* **2009,** *109* (11), 5687-5754.

207. Ni, W. H.; Mosquera, R. A.; Perez-Juste, J.; Liz-Marzan, L. M., Evidence for Hydrogen-Bonding-Directed Assembly of Gold Nanorods in Aqueous Solution. *Journal of Physical Chemistry Letters* **2010,** *1* (8), 1181-1185.

208. Nie, Z. H.; Fava, D.; Rubinstein, M.; Kumacheva, E., "Supramolecular" assembly of gold nanorods end-terminated with polymer "Pom-Poms": Effect of pom-

pom structure on the association modes. *Journal of the American Chemical Society* **2008,** *130* (11), 3683-3689.

209. Li, Z. T.; Zhu, Z. N.; Liu, W. J.; Zhou, Y. L.; Han, B.; Gao, Y.; Tang, Z. Y., Reversible Plasmonic Circular Dichroism of Au Nanorod and DNA Assemblies. *Journal of the American Chemical Society* **2012,** *134* (7), 3322-3325.

210. Taladriz-Blanco, P.; Buurma, N. J.; Rodriguez-Lorenzo, L.; Perez-Juste, J.; Liz-Marzan, L. M.; Herves, P., Reversible assembly of metal nanoparticles induced by penicillamine. Dynamic formation of SERS hot spots. *Journal of Materials Chemistry* **2011,** *21* (42), 16880-16887.

211. Yao, H.; Ning, Y.; Jesson, C. P.; He, J.; Deng, R. H.; Tian, W.; Armes, S. P., Using Host-Guest Chemistry to Tune the Kinetics of Morphological Transitions Undertaken by Block Copolymer Vesicles. *ACS Macro Letters* **2017,** *6* (12), 1379-1385.

212. Hwang, I.; Jeon, W. S.; Kim, H. J.; Kim, D.; Kim, H.; Selvapalam, N.; Fujita, N.; Shinkai, S.; Kim, K., Cucurbit[7]uril: A simple macrocyclic, pH-triggered hydrogelator exhibiting guest-induced stimuli-responsive behavior. *Angewandte Chemie International Edition* **2007,** *46* (1-2), 210-213.

213. Choi, H. S.; Huh, K. M.; Ooya, T.; Yui, N., pH- and thermosensitive supramolecular assembling system: Rapidly responsive properties of beta-cyclodextrin-conjugated poly(epsilon-lysine). *Journal of the American Chemical Society* **2003,** *125* (21), 6350-6351.

214. Park, C.; Lee, K.; Kim, C., Photoresponsive Cyclodextrin-Covered Nanocontainers and Their Sol-Gel Transition Induced by Molecular Recognition. *Angewandte Chemie International Edition* **2009,** *48* (7), 1275-1278.

215. Benyettou, F.; Zheng, X.; Elacqua, E.; Wang, Y.; Dalvand, P.; Asfari, Z.; Olsen, J. C.; Han, D. S.; Saleh, N.; Ehabiri, M.; Weck, M.; Trabolsi, A., Redox-Responsive Viologen-Mediated Self-Assembly of CB[7]-Modified Patchy Particles. *Langmuir* **2016,** *32* (28), 7144-7150.

216. Boles, M. A.; Engel, M.; Talapin, D. V., Self-Assembly of Colloidal Nanocrystals: From Intricate Structures to Functional Materials. *Chemical Reviews* **2016,** *116* (18), 11220-11289.

217. Song, L. P.; Huang, Y. J.; Nie, Z. H.; Chen, T., Macroscopic two-dimensional monolayer films of gold nanoparticles: fabrication strategies, surface engineering and functional applications. *Nanoscale* **2020,** *12* (14), 7433-7460.

218. Genix, A. C.; Oberdisse, J., Nanoparticle self-assembly: from interactions in suspension to polymer nanocomposites. *Soft Matter* **2018,** *14* (25), 5161-5179.

219. Lin, C.-C.; Ohno, K.; Clarke, N.; Winey, K. I.; Composto, R. J., Macromolecular Diffusion through a Polymer Matrix with Polymer-Grafted Chained Nanoparticles. *Macromolecules* **2014,** *47* (15), 5357-5364.

220. Gwo, S.; Chen, H. Y.; Lin, M. H.; Sun, L.; Li, X., Nanomanipulation and controlled self-assembly of metal nanoparticles and nanocrystals for plasmonics. *Chemical Society Reviews* **2016,** *45* (20), 5672-5716.

221. Powell, A. W.; Stavrinadis, A.; de Miguel, I.; Konstantatos, G.; Quidant, R., White and Brightly Colored 3D Printing Based on Resonant Photothermal Sensitizers. *Nano Letters* **2018,** *18* (11), 6660-6664.

222. Renna, L. A.; Boyle, C. J.; Gehan, T. S.; Venkataraman, D., Polymer Nanoparticle Assemblies: A Versatile Route to Functional Mesostructures. *Macromolecules* **2015,** *48* (18), 6353-6368.

223. Watanabe, M. I., Ayako; Wang, Hui; Murata, Kunihiko; Ikariya, Takao, Catalytic Enantioselective Michael Addition of 1,3-Dicarbonyl Compounds to Nitroalkenes Catalyzed by Well-Defined Chiral Ru Amido Complexes. *Journal of the American Chemical Society* **2004,** *126* (36), 11148-11149.

224. Wu, X.; Hao, C.; Kumar, J.; Kuang, H.; Kotov, N. A.; Liz-Marzan, L. M.; Xu, C., Environmentally responsive plasmonic nanoassemblies for biosensing. *Chemical Society Reviews* **2018,** *47* (13), 4677-4696.

225. Gansel, J. K. T., Michael; Rill, Michael S.; Decker, Manuel; Bade, Klaus; Saile, Volker; von Freymann, Georg; Linden, Stefan; Wegener, Martin, Gold Helix Photonic Metamaterial as Broadband Circular Polarize. *Science* **2009,** *325*, 1513-1515.

226. Xu, L.; Gao, Y.; Kuang, H.; Liz-Marzan, L. M.; Xu, C., MicroRNA-Directed Intracellular Self-Assembly of Chiral Nanorod Dimers. *Angewandte Chemie International Edition in English* **2018,** *57* (33), 10544-10548.

227. Whitesides, G. M. G., Bartosz, Self-Assembly at All Scales. *Science* **2002,** *295*, 2418-2421.

228. Kim, J.; Song, X. H.; Ji, F.; Luo, B. B.; Ice, N. F.; Liu, Q. P.; Zhang, Q.; Chen, Q., Polymorphic Assembly from Beveled Gold Triangular Nanoprisms. *Nano Letters* **2017,** *17* (5), 3270-3275.

229. Luo, B.; Smith, J. W.; Ou, Z.; Chen, Q., Quantifying the Self-Assembly Behavior of Anisotropic Nanoparticles Using Liquid-Phase Transmission Electron Microscopy. *Accounts of Chemical Research* **2017,** *50* (5), 1125-1133.

230. Salant, A.; Amitay-Sadovsky, E.; Banin, U., Directed self-assembly of gold-tipped CdSe nanorods. *Journal of the American Chemical Society* **2006,** *128* (31), 10006-10007.

231. Fu, Q.; Ran, G. J.; Xu, W. L., Direct self-assembly of CTAB-capped Au nanotriangles. *Nano Resesrch* **2016,** *9* (11), 3247-3256.

232. van der Stam, W.; Gantapara, A. P.; Akkerman, Q. A.; Soligno, G.; Meeldijk, J. D.; van Roij, R.; Dijkstra, M.; Donega, C. D., Self-Assembly of Colloidal Hexagonal Bipyramid- and Bifrustum-Shaped ZnS Nanocrystals into Two-Dimensional Superstructures. *Nano Letters* **2014,** *14* (2), 1032-1037.

233. Morphew, D.; Shaw, J.; Avins, C.; Chakrabarti, D., Programming Hierarchical Self-Assembly of Patchy Particles into Colloidal Crystals via Colloidal Molecules. *ACS Nano* **2018,** *12* (3), 2355-2364.

234. Zhang, S. Y.; Regulacio, M. D.; Han, M. Y., Self-assembly of colloidal one-dimensional nanocrystals. *Chemical Society Reviews* **2014,** *43* (7), 2301-23.

235. Markus B. Bannwarth, S. U., Sandro Ebert, David A. Weitz, Daniel Crespy,and; Landfester, K., Colloidal Polymers with Controlled Sequence and Branching Constructed from Magnetic Field Assembled Nanoparticles. *ACS Nano* **2015,** *9* (3), 2720-2728.

236. Silvina M. Gatica, M. W. C., and Darrell Velegol, Designing van der Waals Forces between Nanocolloids. *Nano Letters* **2005,** *5* (1), 169-173.

237. Yi, C. L.; Yang, Y. Q.; Liu, B.; He, J.; Nie, Z. H., Polymer-guided assembly of inorganic nanoparticles. *Chemical Society Reviews* **2020,** *49* (2), 465-508.

238. Xu, N.; Han, J.; Zhu, Z. G.; Song, B.; Lu, X. H.; Cai, Y. L., Directional supracolloidal self-assembly via dynamic covalent bonds and metal coordination. *Soft Matter* **2015,** *11* (27), 5546-5553.

239. Gobre, V. V.; Tkatchenko, A., Scaling laws for van der Waals interactions in nanostructured materials. *Nature Communications* **2013,** *4*, 2341.

240. Thomas, J. R., Preparation and Magnetic Properties of Colloidal Cobalt Particles. *Journal of Applied Physics* **1966,** *37* (7), 2914-2915.

241. Alexander M. Kalsin, M. F., Maciej Paszewski, Stoyan K. Smoukov, Kyle J. M. Bishop, Bartosz A. Grzybowski, Electrostatic Self-Assembly of Binary

Nanoparticle Crystals with a Diamond-Like Lattice. *Science* **2006,** *312* (5772), 420-424.

242. Boal, A. K. I., Faysal; DeRouchey, Jason E.; Thurn-Albrecht, Thomas; Russell, Thomas P.; Rotello, Vincent M., Self-assembly of nanoparticles into structured spherical and network aggregates. *Nature* **2000,** *404*, 746-748.

243. Caputo, G.; Pinna, N., Nanoparticleself-assembly using π–π interactions. *Journal of Materials Chemistry A* **2013,** *1* (7), 2370-2378.

244. Sanjeeva, K. B.; Pigliacelli, C.; Gazzera, L.; Dichiarante, V.; Bombelli, F. B.; Metrangolo, P., Halogen bond-assisted self-assembly of gold nanoparticles in solution and on a planar surface. *Nanoscale* **2019,** *11* (39), 18407-18415.

245. Kim, Y. G.; Therien-Aubin, H., Impact of the Solvent Quality on the Local Dynamics of Soft and Swollen Polymer Nanoparticles Functionalized with Polymer Chains. *Macromolecules* **2020,** *53* (17), 7561-7569.

246. Kravchenko, V. S.; Potemkin, I. I., Self-assembly of rarely polymer-grafted nanoparticles in dilute solutions and on a surface: From non-spherical vesicles to graphene-like sheets. *Polymer* **2018,** *142*, 23-32.

247. Choueiri, R. M.; Klinkova, A.; Therien-Aubin, H.; Rubinstein, M.; Kumacheva, E., Structural transitions in nanoparticle assemblies governed by competing nanoscale forces. *Journal of the American Chemical Society* **2013,** *135* (28), 10262-5.

248. Fava, D.; Winnik, M. A.; Kumacheva, E., Photothermally-triggered self-assembly of gold nanorods. *Chemical Communications* **2009,** (18), 2571-2573.

249. Halperin, A.; Kroger, M.; Zhulina, E. B., Colloid-Brush Interactions: The Effect of Solvent Quality. *Macromolecules* **2011,** *44* (9), 3622-3638.

250. Li, X.; Liu, X.; Liu, X., Self-assembly of colloidal inorganic nanocrystals: nanoscale forces, emergent properties and applications. *Chemical Society Reviews* **2020**.

251. Hamaker, H. C., The London - Van Der Waals attraction between spherical particles. *Physica* **1937,** *4*, 1058-1072.

252. Vincent, B., The van der Waals attraction between colloid particles having adsorbed layers. II. Calculation of interaction curves. *Journal of Colloid and Interface Science* **1973,** *42* (2), 270-285.

253. Kim, J. U.; Matsen, M. W., Repulsion exerted on a spherical particle by a polymer brush. *Macromolecules* **2008,** *41* (1), 246-252.

254. Rubinstein, M.; Colby, R. H., *Polymer physics*. Oxford university press New York: 2003; Vol. 23.

255. Akcora, P.; Liu, H.; Kumar, S. K.; Moll, J.; Li, Y.; Benicewicz, B. C.; Schadler, L. S.; Acehan, D.; Panagiotopoulos, A. Z.; Pryamitsyn, V.; Ganesan, V.; Ilavsky, J.; Thiyagarajan, P.; Colby, R. H.; Douglas, J. F., Anisotropic self-assembly of spherical polymer-grafted nanoparticles. *Nature Materials* **2009,** *8* (4), 354-U121.

256. Fatkullin, N.; Kimmich, R.; Weber, H. W., Spin-Lattice Relaxation of Polymers - the Memory-Function Formalism. *Physical Review E* **1993,** *47* (6), 4600-4603.

257. Prasad, J.; Zins, I.; Branscheid, R.; Becker, J.; Koch, A. H. R.; Fytas, G.; Kolb, U.; Sonnichsen, C., Plasmonic Core-Satellite Assemblies as Highly Sensitive Refractive Index Sensors. *Journal of Physical Chemistry C* **2015,** *119* (10), 5577-5582.

258. Sebba, D. S.; Mock, J. J.; Smith, D. R.; LaBean, T. H.; Lazarides, A. A., Reconfigurable core-satellite nanoassemblies as molecularly-driven plasmonic switches. *Nano Letters* **2008,** *8* (7), 1803-1808.

259. Zhang, Z. Q.; Bando, K.; Taguchi, A.; Mochizuki, K.; Sato, K.; Yasuda, H.; Fujita, K.; Kawata, S., Au-Protected Ag Core/Satellite Nanoassemblies for Excellent Extra-/Intracellular Surface-Enhanced Raman Scattering Activity. *ACS Applied Materials & Interfaces* **2017,** *9* (50), 44027-44037.

260. Collier, C. P.; Saykally, R. J.; Shiang, J. J.; Henrichs, S. E.; Heath, J. R., Reversible tuning of silver quantum dot monolayers through the metal-insulator transition. *Science* **1997,** *277* (5334), 1978-1981.

261. Wong, S.; Kitaev, V.; Ozin, G. A., Colloidal crystal films: Advances in universality and perfection. *Journal of the American Chemical Society* **2003,** *125* (50), 15589-15598.

262. Shao, Q.; Niu, Z. Q.; Hirtz, M.; Jiang, L.; Liu, Y. J.; Wang, Z. H.; Chen, X. D., High-Performance and Tailorable Pressure Sensor Based on Ultrathin Conductive Polymer Film. *Small* **2014,** *10* (8), 1466-1472.

263. Shin, Y.; Song, J.; Kim, D.; Kang, T., Facile Preparation of Ultrasmall Void Metallic Nanogap from Self-Assembled Gold-Silica Core-Shell Nanoparticles Monolayer via Kinetic Control. *Advanced Materials* **2015,** *27* (29), 4344-4350.

264. Parthasarathy, R.; Lin, X. M.; Jaeger, H. M., Electronic transport in metal nanocrystal arrays: The effect of structural disorder on scaling behavior. *Physical Review Letters* **2001,** *87* (18).

265. Kim, S. H.; Medeiros-Ribeiro, G.; Ohlberg, D. A. A.; Williams, R. S.; Heath, J. R., Individual and collective electronic properties of Ag nanocrystals. *Journal of Physical Chemistry B* **1999,** *103* (47), 10341-10347.

266. Kagan, C. R.; Murray, C. B.; Nirmal, M.; Bawendi, M. G., Electronic energy transfer in CdSe quantum dot solids (vol 76, pg 1517, 1996). *Physical Review Letters* **1996,** *76* (16), 3043-3043.

267. de Jonge, N.; Lamy, Y.; Schoots, K.; Oosterkamp, T. H., High brightness electron beam from a multi-walled carbon nanotube (vol 420, pg 393, 2002). *Nature* **2003,** *423* (6938), 461-461.

268. Murray, C. B.; Sun, S. H.; Gaschler, W.; Doyle, H.; Betley, T. A.; Kagan, C. R., Colloidal synthesis of nanocrystals and nanocrystal superlattices. *Ibm Journal of Research and Development* **2001,** *45* (1), 47-56.

269. Bowen, A. M.; Nuzzo, R. G., Fabrication of Flexible Binary Amplitude Masks for Patterning on Highly Curved Surfaces. *Advanced Functional Materials* **2009,** *19* (20), 3243-3253.

270. Ueno, K.; Misawa, H., Spectral properties and electromagnetic field enhancement effects on nano-engineered metallic nanoparticles. *Physical Chemistry Chemical Physics* **2013,** *15* (12), 4093-4099.

271. Wang, L.; Xiong, W.; Nishijima, Y.; Yokota, Y.; Ueno, K.; Misawa, H.; Qiu, J. R.; Bi, G., Spectral properties of nanoengineered Ag/Au bilayer rods fabricated by electron beam lithography. *Applied Optics* **2011,** *50* (28), 5600-5605.

272. Aksu, S.; Huang, M.; Artar, A.; Yanik, A. A.; Selvarasah, S.; Dokmeci, M. R.; Altug, H., Flexible Plasmonics on Unconventional and Nonplanar Substrates. *Advanced Materials* **2011,** *23* (38), 4422-+.

273. Cheng, W. L.; Park, N. Y.; Walter, M. T.; Hartman, M. R.; Luo, D., Nanopatterning self-assembled nanoparticle superlattices by moulding microdroplets. *Nature Nanotechnology* **2008,** *3* (11), 682-690.

274. Cheng, W. L.; Campolongo, M. J.; Cha, J. J.; Tan, S. J.; Umbach, C. C.; Muller, D. A.; Luo, D., Free-standing nanoparticle superlattice sheets controlled by DNA. *Nature Materials* **2009,** *8* (6), 519-525.

275. Liu, Y. M.; Liu, Y.; Tao, P.; Shang, W.; Song, C. Y.; Deng, T., Vertical segregation in the self-assembly of nanoparticles at the liquid/air interface. *Nanoscale* **2014,** *6* (24), 14662-14666.

276. Vogel, N.; Retsch, M.; Fustin, C. A.; del Campo, A.; Jonas, U., Advances in Colloidal Assembly: The Design of Structure and Hierarchy in Two and Three Dimensions. *Chemical Reviews* **2015,** *115* (13), 6265-6311.

277. Li, S.; Xu, L. G.; Ma, W.; Wu, X. L.; Sun, M. Z.; Kuang, H.; Wang, L. B.; Kotov, N. A.; Xu, C. L., Dual-Mode Ultrasensitive Quantification of MicroRNA in Living Cells by Chiroplasmonic Nanopyramids Self-Assembled from Gold and Upconversion Nanoparticles. *Journal of the American Chemical Society* **2016,** *138* (1), 306-312.

278. Zhao, X. L.; Xu, L. G.; Sun, M. Z.; Ma, W.; Wu, X. L.; Xu, C. L.; Kuang, H., Tuning the interactions between chiral plasmonic films and living cells. *Nature Communications* **2017,** *8*.

279. Zhang, L.; Zha, X. H.; Zhang, G.; Gu, J. C.; Zhang, W.; Huang, Y. J.; Zhang, J. W.; Chen, T., Designing a reductive hybrid membrane to selectively capture noble metallic ions during oil/water emulsion separation with further function enhancement. *Journal of Materials Chemistry A* **2018,** *6* (22), 10217-10225.

280. Scanlon, M. D.; Smirnov, E.; Stockmann, T. J.; Peljo, P., Gold Nanofilms at Liquid-Liquid Interfaces: An Emerging Platform for Redox Electrocatalysis, Nanoplasmonic Sensors, and Electrovariable Optics. *Chemical Reviews* **2018,** *118* (7), 3722-3751.

281. Guo, Z. Y.; Jia, Y. R.; Song, X. X.; Lu, J.; Lu, X. F.; Liu, B. Q.; Han, J. J.; Huang, Y. J.; Zhang, J. W.; Chen, T., Giant Gold Nanowire Vesicle-Based Colorimetric and SERS Dual-Mode Immunosensor for Ultrasensitive Detection of Vibrio parahemolyticus. *Analytical Chemistry* **2018,** *90* (10), 6124-6130.

282. Si, S. R.; Liang, W. K.; Sun, Y. H.; Huang, J.; Ma, W. L.; Liang, Z. Q.; Bao, Q. L.; Jiang, L., Facile Fabrication of High-Density Sub-1-nm Gaps from Au Nanoparticle Monolayers as Reproducible SERS Substrates. *Advanced Functional Materials* **2016,** *26* (44), 8137-8145.

283. Baffou, G.; Quidant, R., Nanoplasmonics for chemistry. *Chemical Society Reviews* **2014,** *43* (11), 3898-3907.

284. Ding, S. Y.; Yi, J.; Li, J. F.; Ren, B.; Wu, D. Y.; Panneerselvam, R.; Tian, Z. Q., Nanostructure-based plasmon-enhanced Raman spectroscopy for surface analysis of materials. *Nature Reviews Materials* **2016,** *1* (6).

285. Gu, M.; Zhang, Q. M.; Lamon, S., Nanomaterials for optical data storage. *Nature Reviews Materials* **2016,** *1* (12).

286. Song, L. P.; Qiu, N. X.; Huang, Y. J.; Cheng, Q.; Yang, Y. P.; Lin, H.; Su, F. M.; Chen, T., Macroscopic Orientational Gold Nanorods Monolayer Film with Excellent Photothermal Anticounterfeiting Performance. *Advanced Optical Materials* **2020,** *8* (18).

287. Deak, A.; Bancsi, B.; Toth, A. L.; Kovacs, A. L.; Horvolgyi, Z., Complex Langmuir-Blodgett films from silica nanoparticles: An optical spectroscopy study. *Colloid Surface A* **2006,** *278* (1-3), 10-16.

288. Reculusa, S.; Ravaine, S., Colloidal photonic crystals obtained by the Langmuir-Blodgett technique. *Applied Surface Science* **2005,** *246* (4), 409-414.

289. Szekeres, M.; Kamalin, O.; Grobet, P. G.; Schoonheydt, R. A.; Wostyn, K.; Clays, K.; Persoons, A.; Dekany, I., Two-dimensional ordering of Stober silica particles at the air/water interface. *Colloid Surface A* **2003,** *227* (1-3), 77-83.

290. Kalosi, A.; Demydenko, M.; Bodik, M.; Hagara, J.; Kotlar, M.; Kostiuk, D.; Halahovets, Y.; Vegso, K.; Roldan, A. M.; Maurya, G. S.; Angus, M.; Veis, P.; Jergel, M.; Majkova, E.; Siffalovic, P., Tailored Langmuir-Schaefer Deposition of Few-Layer MoS2 Nanosheet Films for Electronic Applications. *Langmuir* **2019,** *35* (30), 9802-9808.

291. Bodik, M.; Demydenko, M.; Shabelnyk, T.; Halahovets, Y.; Kotlar, M.; Kostiuk, D.; Shaji, A.; Brunova, A.; Veis, P.; Jergel, M.; Majkova, E.; Siffalovic, P., Collapse Mechanism in Few-Layer MoS2 Langmuir Films. *Journal of Physical Chemistry C* **2020,** *124* (29), 15856-15861.

292. Bardosova, M.; Dillon, F. C.; Pemble, M. E.; Povey, I. M.; Tredgold, R. H., Langmuir-Blodgett assembly of colloidal photonic crystals using silica particles prepared without the use of surfactant molecules. *Journal of Colloid and Interface Science* **2009,** *333* (2), 816-819.

293. Stefaniu, C.; Chanana, M.; Wang, D. Y.; Novikov, D. V.; Brezesinski, G.; Mohwald, H., Langmuir and Gibbs Magnetite NP Layers at the Air/Water Interface. *Langmuir* **2011,** *27* (3), 1192-1199.

294. Hur, J.; Won, Y. Y., Fabrication of high-quality non-close-packed 2D colloid crystals by template-guided Langmuir-Blodgett particle deposition. *Soft Matter* **2008,** *4* (6), 1261-1269.

295. Halas, N. J.; Lal, S.; Chang, W. S.; Link, S.; Nordlander, P., Plasmons in Strongly Coupled Metallic Nanostructures. *Chemical Reviews* **2011,** *111* (6), 3913-3961.